

2016-05-11

# Zernike Wavefront Reconstruction of In Vitro Crystalline Lenses From Laser Ray Tracing Spot Patterns

Yue Yao

University of Miami, yyao1@umiami.edu

Follow this and additional works at: [https://scholarlyrepository.miami.edu/oa\\_theses](https://scholarlyrepository.miami.edu/oa_theses)

---

## Recommended Citation

Yao, Yue, "Zernike Wavefront Reconstruction of In Vitro Crystalline Lenses From Laser Ray Tracing Spot Patterns" (2016). *Open Access Theses*. 606.

[https://scholarlyrepository.miami.edu/oa\\_theses/606](https://scholarlyrepository.miami.edu/oa_theses/606)

This Open access is brought to you for free and open access by the Electronic Theses and Dissertations at Scholarly Repository. It has been accepted for inclusion in Open Access Theses by an authorized administrator of Scholarly Repository. For more information, please contact [repository.library@miami.edu](mailto:repository.library@miami.edu).



UNIVERSITY OF MIAMI

ZERNIKE WAVEFRONT RECONSTRUCTION OF IN VITRO CRYSTALLINE  
LENSES FROM LASER RAY TRACING SPOT PATTERNS

By

Yue Yao

A THESIS

Submitted to the Faculty  
of the University of Miami  
in partial fulfillment of the requirements for  
the degree of Master of Science

Coral Gables, Florida

May 2016

©2016  
Yue Yao  
All Rights Reserved

UNIVERSITY OF MIAMI

A thesis submitted in partial fulfillment of  
the requirements for the degree of  
Master of Science

ZERNIKE WAVEFRONT RECONSTRUCTION OF IN VITRO CRYSTALLINE  
LENSES FROM LASER RAY TRACING SPOT PATTERNS

Yue Yao

Approved:

---

Fabrice Manns, Ph.D.  
Professor of Biomedical  
Engineering and Ophthalmology

---

Noel Ziebarth, Ph.D.  
Assistant Professor of  
Biomedical Engineering

---

Jean-Marie Parel, Ph.D.  
Henri and Flore Lesieur Chair in  
Ophthalmology, Research Associate  
Professor of Ophthalmology and  
Biomedical Engineering

---

Guillermo J. Prado, Ph.D.  
Dean of the Graduate School

YAO, YUE

(M.S., Biomedical Engineering)

Zernike Wavefront Reconstruction of  
in Vitro Crystalline Lenses from Laser  
Ray Tracing Spot Patterns

(May 2016)

Abstract of a thesis at the University of Miami.

Thesis supervised by Professor Fabrice Manns.

No. of pages in text. (84)

The goal of this thesis project is to develop a method to perform direct wavefront reconstruction of *in vitro* crystalline lenses from spot diagrams measured using a Laser Ray Tracing (LRT) system. The LRT system is combined with a commercial Spectral-Domain OCT system to deliver laser rays sequentially onto the *in vitro* crystalline lens. The spot position for each ray is recorded at different axial positions using a camera. A MATLAB program was developed to calculate the slope of the rays from the spot positions. The ray slopes were used to calculate the Zernike wavefront coefficients using a least square curve fitting algorithm. The method was tested on glass lenses, on cynomolgus monkey lenses, and on human lenses.

## **DEDICATION**

This thesis is dedicated to all of my family members for their care and support of my education pursuits. My father's encouragement and optimism gave me the confidence to follow my dreams and accomplish difficult tasks. His energetic and humorous attitude towards life helped shape me into a very happy and positive person. My mothers' strength and perseverance carried me through all the hard times. I always feel grateful for her sacrifice of taking care of me and my younger sister and brother. To my younger sister and brother, I wish them to grow up with courage and happiness and follow their dreams.

## **ACKNOWLEDGEMENTS**

My most sincere thanks go to my mentor Dr. Fabrice Manns for his guidance, instruction, and unending patience throughout my undergraduate and graduate studies. I would like to thank Dr. Jean-Marie Parel who graciously served on my committee and mentored me for my undergraduate and graduate studies. I am very grateful to have the opportunity be part of the team at Ophthalmic Biophysics Center.

I would like to acknowledge Dr. Noel Ziebarth for her kindness to serve on my committee to participate and review my master thesis.

I would like to thank Dr. Bianca Maceo for providing me with great suggestions throughout my master thesis project and helping me with thesis writing and review. She is very patient and was willing to help whenever I needed.

I would like to thank Siobhan Williams for helping me with MATLAB program development.

I would like to thank Channing Chang for reading my thesis and giving me valuable suggestions.

Finally, I would like to acknowledge the rest of the team at the Ophthalmic Biophysics Center, past and present, for their suggestions and support: Mariela Aguilar, Karam Alawa, Alejandro Arboleda, Dr. Esdras Arrieta, Dr. Robert Augusteyn, Dr. Judith Birkenfeld, Dr. David Borja, Dr. Florence Cabot, Dr. Alberto de Castro, Carolina de Freitas, Stephanie Delgado, Heather Durkee, Dr. Klaus



Ehrmann, Alex Gonzalez, Dr. Victor Hernandez, Dr. Arthur Ho, Shawn Kelly, William Lee, Keke Liu, Daniel Lopez, Dr. Susana Marcos, Gabrielle Mesquita, Ashik Mohamed, Kelly Mote, Derek Nankivil, Izuru Nose, Jennifer Rodriguez, Cor Rowaan, Dr. Marco Ruggeri, Juan Silgado, Dr. Stephen Uhlhorn, Dr. Raksha Urs, Dr. Mukesh Taneja, Altricia Williams.

## TABLE OF CONTENTS

LIST OF FIGURES.....	vii
LIST OF TABLES .....	xiii
CHAPTER 1 AIMS OF STUDY .....	1
CHAPTER 2 BACKGROUND AND SIGNIFICANCE .....	3
2.1 The Optics of The Crystalline Lens .....	3
2.2 <i>In Vitro</i> Wavefront Aberration Measurement Overview.....	3
2.2.1 Point Diffraction Interferometry (PDI) .....	4
2.2.2 Hartmann-Shack Wavefront Sensor .....	5
2.2.3 Laser Ray Tracing.....	6
2.2.4 Comparison of Hartmann-Shack Wavefront Sensors and Laser Ray Tracing .....	8
2.3 Laser Ray Tracing System Developed at OBC.....	9
2.4 Project Need .....	10
CHAPTER 3 WAVEFRONT RECONSTRUCTION .....	11
3.1 Purpose.....	11
3.2 General Principles.....	11
3.3 Zernike Polynomials .....	12
3.4 Wavefront Reconstruction .....	17
3.5 Implementation in MATLAB .....	19
3.6 Testing .....	20
3.7 Summary.....	24
CHAPTER 4 APPLICATION TO THE LRT SYSTEM.....	25
4.1 Purpose.....	25
4.2 Experimental Setup.....	25
4.3 Data Analysis.....	26
4.3.1 Calculation of Spot Centroid Positions .....	26
4.3.2 Pupil Scaling .....	29
4.3.3 Slope Measurements .....	30
4.3.4 Calculation of Zernike Coefficients.....	34
4.4 Experiments.....	35
4.4.1 Glass Lens, f=18mm .....	35
4.4.2 Glass Lens, f=30mm .....	41
4.4.3 Cynomolgus Monkey Lens 1 (4C105-OS) .....	47
4.4.4 Cynomolgus Lens 2 (1632 OS).....	53
4.4.5 Human Eye Bank Lens #1 .....	59
4.4.6 Human Eye Bank Lens #2 .....	65
4.6 Discussion .....	71
CHAPTER 5 SUMMARY AND FUTURE WORK.....	76
5.1 Summary.....	76
5.2 Zernike Coefficients Distortion Correction.....	76
5.3 Effects of the Centroids Position Errors on the Slope Calculation.....	77
5.4 Evaluate Effects of Input Beam Geometry.....	78
WORKS CITED .....	82

## LIST OF FIGURES

Figure 2.1 Schematic of interferometer with HDI plate in focus (Acosta et al., 2009). .....	4
Figure 2.2 Schematic diagram of the Hartmann-Shack wavefront sensor experimental setup (Barriuso & Navarro, 2000). .....	5
Figure 2.3 Hartmann-Shack Wavefront Sensor: (a) single element illustrating how a lenslet is used to sense wavefront tilt; (b) the lenslet array to sense local tilt of a large wavefront (Liang et al., 1991). .....	6
Figure 2.4 Schematic diagrams of Laser Ray Tracing experimental Setup (Barriuso & Navarro, 2000). .....	6
Figure 2.5 Scanning laser optical performance evaluator (SLOPE). The system consists of a laser, two mirrors mounted on translation stages, a chamber filled with saline in which the lens is placed, and two CCD cameras, one above and the other to the side of the glass chamber. The cameras view the trajectory of the laser beams as they enter and are refracted by the crystalline lens (Rooda & Glasser, 2010). .....	7
Figure 2.6 Schematic of the LRT beam delivery onto a crystalline lens mounted in a mini-motorized lens stretcher. The position of the camera is measured as a distance $z$ (mm) below the tissue chamber (Maceo et al., 2015). .....	9
Figure 3.1 Cartesian and polar coordinates $(x,y)$ and $(r,\theta)$ , respectively, of a pupil point $Q$ in the plane of the exit pupil (Malacara, 2007). .....	13
Figure 3.2 Given Zernike coefficients $a_i$ . The values for the Zernike coefficients were taken from a published paper for cynomolgus monkey eyes (Roorda & Glasser, 2004). .....	21
Figure 3.3 Calculated Zernike coefficients $a_o$ . .....	22
Figure 3.4 Difference between Given Zernike coefficients $a_i$ and calculated Zernike coefficients $a_o$ . The difference is on the scale of $10^{-14}$ . .....	23
Figure 4.1 Experimental Setup. The LRT uses the source and beam delivery of a Spectral-Domain OCT system to deliver input rays onto the crystalline lens sequentially. The camera is used to record the spots positions of each ray sequentially at different vertical camera positions. The recorded spot positions for each ray at different vertical camera positions are used to calculate the ray slopes for Zernike wavefront reconstruction (Maceo, 2015). .....	25

Figure 4.2 Examples of spot images recorded from the LRT system. ....	26
Figure 4.3 Camera recorded spot centroids positions without the presence of the chamber. ....	28
Figure 4.4 Spots positions for all of the 621 rays without the presence of the chamber. The spot positions recorded by the camera were shifted to center at the (0,0) position. ....	28
Figure 4.5 Sampling geometry of the Zernike wevefront reconstruction within unit circle. All of the 621 rays form a 23 by 27 matrix. Some of the spot positions were recorded outside of the unit circle and therefore eliminated for the wavefront reconstruction. ....	29
Figure 4.6 Schematic of LRT beam propagating through the lens along the z-direction. $h$ is the entrance ray height, $\theta$ is the incident angle ( $\theta=0$ ), $d_p$ is the distance between the posterior surface of the lens and the window of the tissue chamber, $n_a$ is the refractive index of the medium, $d_w$ is the thickness of the window, $n_w$ is the refractive index of the glass window, $n_{air}$ is the refractive index of air ( $n_{air}=1$ ), $y$ is the ray height incident on the camera, $\theta' = dy/dz$ is the output ray slope, and $z_{focus}$ is the distance between the posterior window surface and the intersection of the lens focus along the optical axis (Maceo et al., 2015). ....	30
Figure 4.7 Centered camera recorded spots positions for rays within a circle of 6 diameter from $z=1\text{mm}$ to $z=8\text{mm}$ ....	31
Figure 4.8 Examples of x slopes calculation. The 6 rays were picked from the locations where the camera recorded y positions=0. ....	32
Figure 4.9 Examples of y slopes calculation. The 6 rays were picked from the locations where the camera recorded x positions=0. ....	32
Figure 4.10 Example of an output slope matrix for x-slope. The location of the labeled slope outputs corresponds to the location of the input laser beams in the sampling geometry used. Some of the camera recorded images do not have good spots. The image data in these locations are discarded. The calculated slope values are multiplied by 1000 on the map for easy reading purpose. ....	33
Figure 4.11 Example of an output slope matrix for y-slope. The location of the labeled slope outputs corresponds to the location of the input laser beams in the sampling geometry used. Some of the camera recorded images do not have good spots. The image data in these locations are discarded. The calculated slope values are multiplied by 1000 on the map for easy reading purpose. ....	33

Figure 4.12 Principle of the MATLAB program to calculate the Zernike coefficients. ....	34
Figure 4.13 Sample geometry. The sample matrix was 13 rows by 13 columns. The matrix was scaled from the 3mm radius to the unit radius .....	35
Figure 4.14 Camera recorded spots centroids from z=1mm to z=8 mm. The sample matrix was 13 rows by 13 columns. The recorded spots centroids are used to calculate the ray slopes.....	36
Figure 4.15 Camera recorded spots position differences along the z axis.....	37
Figure 4.16 Output slope map for x direction. The calculated slope values were multiplied by 1000 on the map for easy reading purpose. The location of the labeled slope outputs corresponds to the location of laser beams in 13 rows by 13 columns sample geometry. ....	38
Figure 4.17 Output slope map for y direction. The calculated slope values were multiplied by 1000 on the map for easy reading purpose. The location of the labeled slope outputs corresponds to the location of laser beams in 13 rows by 13 columns sample geometry. ....	38
Figure 4.18 Zernike coefficients for the f=18mm glass lens. The sample geometry was 13 rows by 13 columns over a 6mm diameter zone. ....	39
Figure 4.19 Zernike coefficients starting from Z [3, -3] for the f=18mm glass lens. ....	40
Figure 4.20 Sample geometry. The sample matrix was 13 rows by 13 columns. The matrix was scaled from the 3mm radius to the unit radius.....	41
Figure 4.21 Camera recorded spots positions from z=1mm to z=8 mm. The sample matrix was 13 rows by 13 columns.....	42
Figure 4.22 Camera recorded spots position differences along the z axis.....	43
Figure 4.23 Output slope map for x direction. The calculated slope values were multiplied by 1000 on the map for easy reading purpose. The location of the labeled slope outputs corresponds to the location of laser beams in 13 rows by 13 columns sample geometry. ....	44
Figure 4.24 Output slope map for y direction. The calculated slope values were multiplied by 1000 on the map for easy reading purpose. The location of the labeled slope outputs corresponds to the location of laser beams in 13 rows by 13 columns sample geometry. ....	44
Figure 4.25 Zernike coefficients for the f=30 mm glass lens. The sample geometry was 13 rows by 13 columns over a 6 mm diameter zone. ....	45

Figure 4.26 Zernike coefficients starting from Z [3, -3] for the f=30mm glass lens. .....	46
Figure 4.27 Sample geometry. The sample matrix was 19 rows by 19 columns. The matrix was scaled from the 2mm radius to the unit radius.....	47
Figure 4.28 Centered camera recorded spots positions for input rays within a circular aperture of of 4mm from z=1mm to z=8 mm. The sample matrix was 19 rows by 19 columns. ....	48
Figure 4.29 Centered camera recorded spots position differences along the z axis.....	49
Figure 4.30 Output slope map for x direction. The calculated slope values were multiplied by 1000 on the map for easy reading purpose. The location of the labeled slope outputs corresponds to the location of laser beams in 19 rows by 19 columns sample geometry. ....	50
Figure 4.31 Output slope map for y direction. The calculated slope values were multiplied by 1000 on the map for easy reading purpose. The location of the labeled slope outputs corresponds to the location of laser beams in 19 rows by 19 columns sample geometry. ....	50
Figure 4.32 Zernike coefficients for Cynomolgus lens 4C105 OS in the stretched state. The sample geometry was 19 rows by 19 columns over a 4mm diameter zone. ....	51
Figure 4.33 Zernike coefficients starting from Z [3, -3] for Cynomolgus lens 4C105 OS in the stretched state. ....	52
Figure 4.34 Sample geometry. The sample matrix was 19 rows by 19 columns. The matrix was scaled from the 2mm radius to the unit radius .....	53
Figure 4.35 Centered camera recorded spots positions for input rays within a circle of 4mm diameter from z=1mm to z=8 mm. The sample matrix was 19 rows by 19 columns. ....	54
Figure 4.36 Centered camera spots position differences along the z axis.....	55
Figure 4.37 Output slope map for x direction. The calculated slope values were multiplied by 1000 on the map for easy reading purpose. The location of the labeled slope outputs corresponds to the location of the input laser beams in 19 rows by 19 columns sample geometry. ....	56
Figure 4.38 Output slope map for y direction. The calculated slope values were multiplied by 1000 on the map for easy reading purpose. The location of the labeled slope outputs corresponds to the location of the input laser beams in 19 rows by 19 columns sample geometry. ....	56

Figure 4.39 Zernike coefficients for Cynomolgus lens 1632 OS. The sample geometry is 19 rows by 19 columns over a 4 mm diameter zone in the stretched state.....	57
Figure 4.40 Zernike coefficients starting from Z [3, -3] for Cynomolgus lens 1632 OS in the stretched state.....	58
Figure 4.41 Sample geometry. The sample matrix was 13 rows by 13 columns. The matrix was scaled from the 3mm radius to the unit radius.....	59
Figure 4.42 Camera recorded spots positions from z=1mm to z=8 mm. The sample matrix was 13 rows by 13 columns over a 6mm diameter zone.....	60
Figure 4.43 Camera recorded spots position differences along the z axis.....	61
Figure 4.44 Output slope map for x direction. The calculated slope values were multiplied by 1000 on the map for easy reading purpose. The location of the labeled slope outputs corresponds to the location of the input laser beams in 13 rows by 13 columns sample geometry.....	62
Figure 4.45 Output slope map for y direction. The calculated slope values were multiplied by 1000 on the map for easy reading purpose. The location of the labeled slope outputs corresponds to the location of the input laser beams in 13 rows by 13 columns sample geometry.....	62
Figure 4.46 Zernike coefficients for human lens # 16-04-014 OS. The sample geometry was 13 rows by 13 columns over a 6mm diameter zone. ....	63
Figure 4.47 Zernike coefficients starting from Z [3, -3] for human lens # 16-04-014 OS. ....	64
Figure 4.48 Sample geometry. The sample matrix was 13 rows by 13 columns. The matrix was scaled from the 3mm radius to the unit radius.....	65
Figure 4.49 Camera recorded spots positions from z=1mm to z=8 mm. The sample matrix was 13 rows by 13 columns over a 6mm diameter zone.....	66
Figure 4.50 Camera recorded spots position differences along the z axis.....	67
Figure 4.51 Output slope map for x direction. The calculated slope values were multiplied by 1000 on the map for easy reading purpose. The location of the labeled slope outputs corresponds to the location of the input laser beams in a 13 rows by 13 columns sample geometry.....	68
Figure 4.52 Output slope map for y direction. The calculated slope values were multiplied by 1000 on the map for easy reading purpose. The location of the labeled slope outputs corresponds to the location of the input laser beams in a 13 rows by 13 columns sample geometry.....	68

Figure 4.53 Zernike coefficients for human lens # 16-04-014 OD. The sample geometry was 13 rows by 13 columns over a 6mm diameter zone. ....	69
Figure 4.54 Zernike coefficients starting from $Z[-3,3]$ for human lens # 16-04-014 OD. ....	70
Figure 4.55 The relationship between wavefront aberration $W$ , input ray height $h$ and effective focal length $f$ under the assumption that aberrations other than $Z_2^0$ were negligible.....	71
Figure 5.1 Examples of spot images from a human lens with cataract .....	77
Figure 5.2 Spot centroids for empty cell experiment. The entrance rays form a 13 by 13 matrix over a 6 mm pupil size with 0.5mm increment. ....	78
Figure 5.3 Ray slopes of the entrance beam. The values were multiplied by 1000 for easy reading purpose. ....	79
Figure 5.4 Spot centroids differences along the $z$ direction for the empty cell experiment. ....	79
Figure 5.5. Calculated Zernike coefficients for empty cell experiments from $Z [0,0]$ to $Z[6,6]$ . ....	80
Figure 5.6 Calculated Zernike coefficients for empty cell experiments from $Z [3,-3]$ to $Z[6,6]$ . ....	81



## LIST OF TABLES

Table 3.1 Algebraic expansion of the Zernike Polynomial Sequence, orders from one to seven (Lakshminarayanan & Fleck, 2011).....	14
Table 3.2 Algebraic expansions of partial derivatives over x of the Zernike polynomial sequence .....	15
Table 3.3 Algebraic expansions of partial derivatives over y of the Zernike polynomial sequence .....	16
Table 4.1 Comparison between calculated focal length and expected focal length .....	73
Table 4.2 Comparison between calculated effective lens power values and published effective lens power values for cynomolgus lenses. For cynomolgus lenses, the Zernike coefficients are reconstructed over a 4mm pupil diameter.....	73
Table 4.3 Comparison between calculated effective lens power values and published effective lens power values for human lenses. For human lenses, the Zernike coefficients are reconstructed over a 6mm pupil diameter.....	74
Table 4.4 Comparison of Zernike coefficients $Z_4^0$ between calculated results and published values for cynomolgus lenses.....	75

## CHAPTER 1

### AIMS OF STUDY

Human eyes can be represented by an optical system containing several optical elements that focus light rays on the retina to form images. The quality of the retinal image depends on the aberration and diffraction properties of the optical system of the eye. For an ideal eye free of aberration, light passing through the pupil and converging on the retina will not cause a blur on the image. In reality, aberrations will give rise to blur of the retinal image and reduce the image quality. The crystalline lens of the eye is one of the key components that contribute to the retinal image quality. It produces approximately one-third of the eye's focusing power (Atchison & Smith, 2000). The power and aberrations of the crystalline lens change with age. These changes have implications in the development of refractive errors and presbyopia.

At the Ophthalmic Biophysics Center (OBC) of the University of Miami's Bascom Palmer Eye Institute, a Laser Tray Tracing (LRT) system combined with a commercial Spectral-Domain Optical Coherence Tomography (OCT) system has been developed to directly measure the power and spherical aberration of crystalline lenses, and to study the changes in lens aberration with age and accommodation. During the *in vitro* experiment, the combined LRT and OCT system delivers laser rays onto the crystalline lens, which is placed in a tissue chamber and submersed in hydration media. The laser rays pass through the crystalline lens and the spot position of each individual ray is recorded by a camera below the tissue chamber at different vertical positions (Maceo et al.,

2015). The centroids of the LRT images are determined using existing programs. The recorded spot images are used to calculate ray slope for each ray. The ray slopes can be used to calculate wavefront aberrations.

The aim of the project is to develop a MATLAB program to perform Zernike wavefront reconstruction for *in vitro* crystalline lenses from the LRT recorded spot patterns. The inputs of the MATLAB program are the recorded spot centroids obtained from the LRT experiments for crystalline lenses. The spot centroids recorded at different vertical positions will be used to calculate the slope of each ray. A modal reconstruction method will be implemented to calculate Zernike coefficients from the slopes. The MATLAB program will be tested on glass lenses, cynomolgus monkey lenses, and human lenses.

## CHAPTER 2

### BACKGROUND AND SIGNIFICANCE

#### 2.1 The Optics of The Crystalline Lens

The crystalline lens of human eyes continuously grows throughout life. The continued growth of the crystalline lens changes the shape and gradient refractive index of the lens, which causes changes in the optical power and aberrations. The effects of these changes on the optical quality of the human eyes in general and their implications for the development of refractive error, the development of presbyopia, and the long term outcomes for vision correction procedures are not well understood (Smith, 2003; Kasthurirangan et al., 2008).

In order to improve vision correction treatments, a better understanding of the effects of the change of shape and gradient refractive index on optical power and aberration are needed. *In vivo*, measurements remain challenging because it is difficult to directly measure the lens power, or spherical aberration (Garner & Smith, 1997). The application of *in vitro* wavefront aberration measurement technique can provide valuable information on the optical properties of the crystalline lenses.

#### 2.2 *In Vitro* Wavefront Aberration Measurement Overview

The three common approaches for the measurement of wavefront aberrations of *in vitro* crystalline lens are Point Diffraction Interferometry (PDI) (Smartt, 1975, Acosta et al., 2009), Hartmann-Shack wavefront sensors (H-S)(Liang et al.,

1994, Liang & Williams, 1997), and Laser Ray Tracing (LRT)(Navarro & Losada, 1997).

### 2.2.1 Point Diffraction Interferometry (PDI)

PDI uses a common-path interferometer to measure the fringes from the phase difference between the wave to be examined and a diffraction generated reference wave (Smartt, 1975). A modified PDI with a larger pinhole diameter (to be referred as HDI) was proposed to measure the aberrations of *in vitro* crystalline lenses (Acosta et al., 2009). Figure 2.1 shows the schematic of the interferometer with the HDI plate placed in focus.

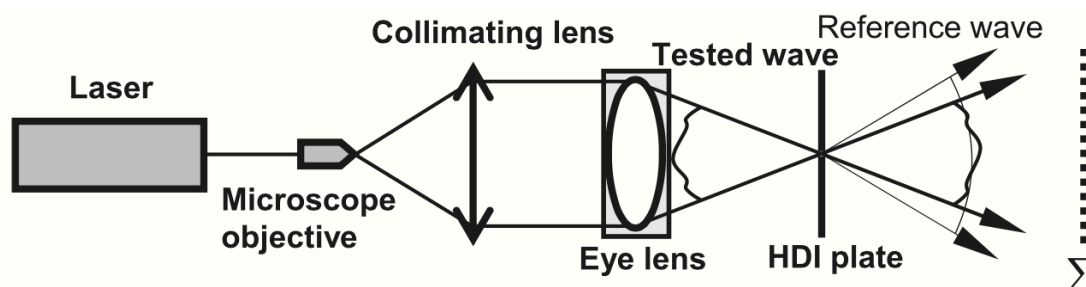


Figure 2.1 Schematic of interferometer with HDI plate in focus (Acosta et al., 2009).

In this approach, the eye lens is immersed in a 0.9% sodium chloride solution. The interference between the wave leaving the crystalline lens and the reference wave produces an interference pattern that will be used to represent the crystalline lens aberrations. Traditional PDIs are designed to measure very small aberrations, which are not suited for the crystalline lens of the eye. The modified HDI allows the measuring of larger aberrations. The draw back of the HDI is the

lower contrast of the fringes at the periphery caused by the use of a larger pinhole, which reduces the sensitivity of the system.

### 2.2.2 Hartmann-Shack Wavefront Sensor

The general principle of H-S to measure the aberrations of *in vitro* crystalline lens is shown in Figure 2.2.

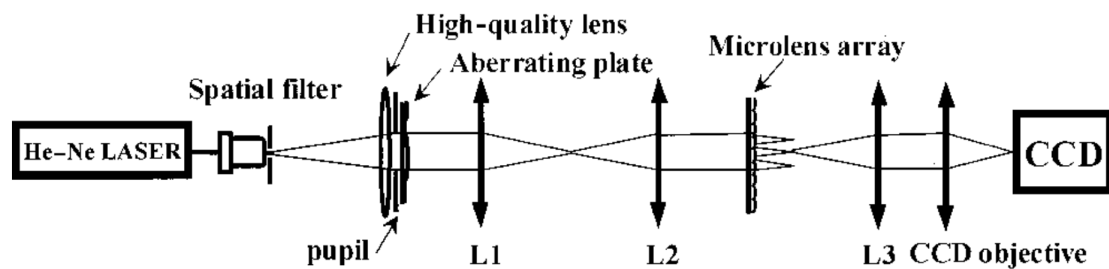


Figure 2.2 Schematic diagram of the Hartmann-Shack wavefront sensor experimental setup (Barriuso & Navarro, 2000).

A He-Ne-Laser is used as the light source. The high-quality lens together with the aberrating plate performs the function of an artificial eye. The pinhole of a spatial filter represent the point object placed at the focal plane of the artificial eye. The pupil is projected onto the microlens array by lenses  $L_1$  and  $L_2$ . The microlens array is located in the conjugate plane of the exit pupil to sample the wavefront. Each lenslet in the array can focus a light beam with a diameter equal to the lens diameter at the focal plane and forms a spot of light. A camera is used to record the positions of the focused spots. Figure 2.3 illustrates the functions of the lenslet array.

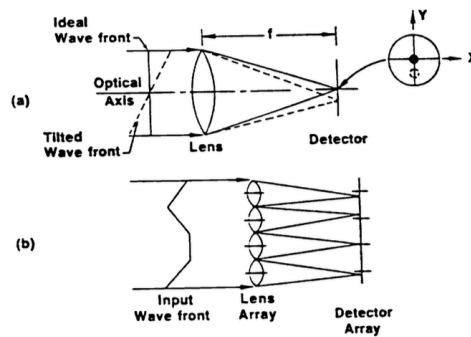


Figure 2.3 Hartmann-Shack Wavefront Sensor: (a) single element illustrating how a lenslet is used to sense wavefront tilt; (b) the lenslet array to sense local tilt of a large wavefront (Liang et al., 1991).

For a system with the presence of aberrations, the laser rays leaving the lens and passing through the microlenses are tilted as shown in Figure 2.3. The recorded spot images are shifted from the referenced positions. These spot positions are proportional to the wavefront slopes and can be used to calculate the wavefront aberration of the lens (Barriuso & Navarro, 2000).

### 2.2.3 Laser Ray Tracing

The schematic of the LRT experimental set up is shown in Figure 2.4.

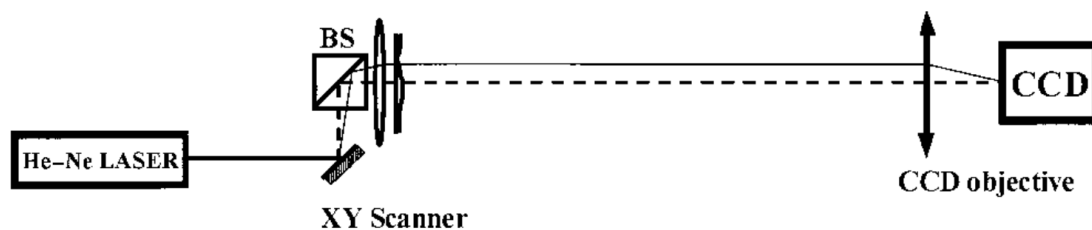


Figure 2.4 Schematic diagrams of Laser Ray Tracing experimental Setup (Barriuso & Navarro, 2000).

In the LRT experimental setup, the system delivers laser rays onto the *in vitro* crystalline lens sequentially over the desired pupil coordinates. In Figure 2.4, a

He-Ne laser is used as the source of the rays and a two dimensional  $XY$  optical scanner is used to produce different sampling geometries. A camera is used to record the spot positions for the rays passing through the lens. The recorded spot centroids will be used to calculate the slopes of the rays.

In a recent study performed by Roorda and Glasser (2004), the laser ray tracing technique was used to measure aberrations in the crystalline lens mounted in a lens stretcher to study the changes in aberrations under simulated accommodation. Figure 2.5 demonstrates the schematic of the system setup used in the study.

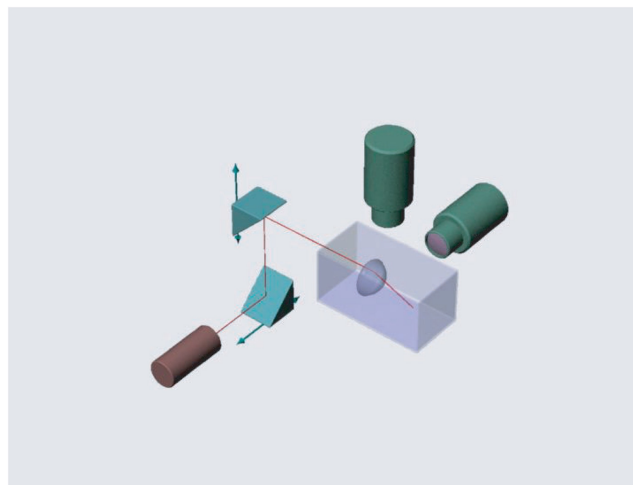


Figure 2.5 Scanning laser optical performance evaluator (SLOPE). The system consists of a laser, two mirrors mounted on translation stages, a chamber filled with saline in which the lens is placed, and two CCD cameras, one above and the other to the side of the glass chamber. The cameras view the trajectory of the laser beams as they enter and are refracted by the crystalline lens (Roorda & Glasser, 2010).

In this study, the two CCD cameras were used to image the laser beam trajectories from the top and side view. The 3-D laser scanning technique acquires the slopes of the wavefront that were used for the determination of the wavefront aberrations. The data analysis and wavefront reconstruction procedures were performed with custom software. However, there were several



limitations of the study. Only one set of experimental results for a macaque lens was reported. Therefore, there was not enough experimental data to validate the approach.

#### **2.2.4 Comparison of Hartmann-Shack Wavefront Sensors and Laser Ray Tracing**

The main difference between Hartmann-Shack method and laser ray tracing method is that Hartmann-Shack wavefront sensor uses a microlens array to sample the wavefront and measure the wavefront slopes, where as laser ray tracing specifies the trajectory of each ray through imaging the spots formed by the ray after passing through the artificial lens (Navarro & Barriuso, 1999, Barriuso & Navarro, 2000).

In the Hartmann-Shack method, the geometry of the wavefront sampling points and the resolution of the microlenses may limit the measurement range of the wavefront aberrations. For eyes with large aberrations, the recorded spots become highly distorted and it is very difficult to calculate the spot centroids positions. The laser ray tracing method is significantly more reliable against the presence of large aberrations because each ray is recorded and processed sequentially. The spot centroids calculation process of the laser ray tracing method is easier than the Hartmann-Shack method.

### 2.3 Laser Ray Tracing System Developed at OBC

At the Ophthalmic Biophysics Center (OBC) in Bascom Palmer Eye Institute, a laser ray tracing (LRT) system combined with an optical coherence tomography (OCT) system has been developed to measure lens power and spherical aberration directly on *in vitro* crystalline lens.

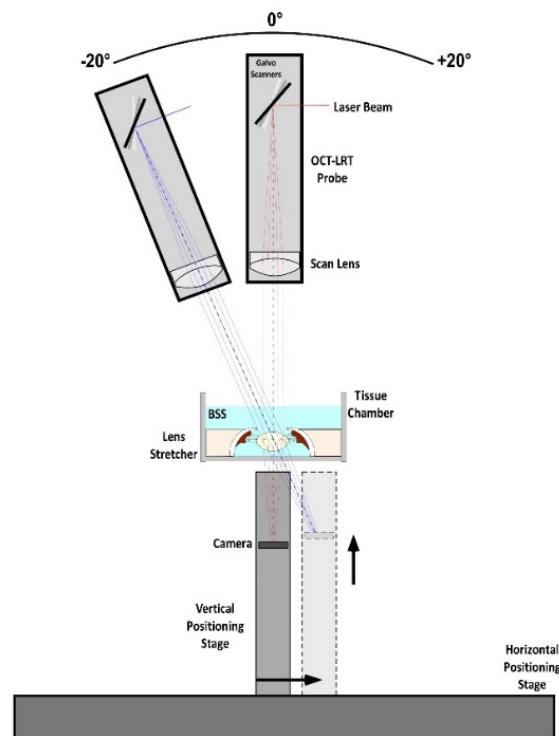


Figure 2.6 Schematic of the LRT beam delivery onto a crystalline lens mounted in a mini-motorized lens stretcher. The position of the camera is measured as a distance  $z$  (mm) below the tissue chamber (Maceo et al., 2015).

The laser ray tracing system is combined with a Spectral-Domain optical coherence tomography (OCT) system and a custom beam delivery probe (Bioptigen, Morrisville, NC) to perform ray tracing through the lens. Figure 2.6 is a schematic of the LRT beam delivery system. The lens is placed in a tissue chamber filled with Balanced Salt Solution (BSS). The lens is either isolated from

the eye or mounted in a miniature lens stretcher designed to simulate accommodation. A camera module (DCC1545M-GL, Thorlabs, USA) is mounted on a vertical positioning stage below the tissue chamber. During an LRT experiment, the LRT system delivers equally spaced parallel beams sequentially along the vertical direction on to the crystalline lens. The camera is used to record the spots position at different vertical positions corresponding to each individual ray. An existing MATLAB program is used to find the centroid position of each spot to estimate the measured ray height.

#### **2.4 Project Need**

The purpose of this thesis project is to develop a MATLAB program that uses a Zernike wavefront reconstruction algorithm to directly estimate the wavefront aberration of crystalline lenses measured in the LRT system. The developed program will be validated through performing LRT experiments on crystalline lenses and comparing the results with theoretical predictions and previous works.

The slopes of the emerging rays will be calculated based on the spot centroids acquired from the LRT experiments. The wavefront aberration will be reconstructed from the slopes by using a least squares procedure to fit a Zernike polynomial function. The resulting Zernike coefficients represent the wavefront of the crystalline lenses. The use of laser ray tracing technique to measure wavefront aberration over the lens surface will provide valuable information about the optical and accommodative performance of the *in vitro* crystalline lens.

## **CHAPTER 3**

### **WAVEFRONT RECONSTRUCTION**

#### **3.1 Purpose**

Laser ray tracing techniques have been applied to study the wavefront aberrations of the crystalline lens and provide valuable information related to the optical properties of the lens (Navarro & Losada, 1997, Maceo et al., 2015). An LRT system provides the local slope measurements of the wavefront that are essential for the Zernike wavefront reconstruction. Least-square fitting is generally used to calculate the wavefront aberration from wavefront slope measurements (Southwell, 1980). This chapter describes the development of a Zernike wavefront reconstruction MATLAB program that will be used to convert the slopes measured with the LRT system into wavefront aberration maps.

#### **3.2 General Principles**

Various approaches have been proposed to achieve wavefront reconstruction. These approaches may be classified into two categories, i.e., zonal wavefront reconstruction and modal wavefront reconstruction. The key difference between zonal estimation and modal estimation is the method used to fit the measured local slopes (Southwell, 1980).

In zonal estimation, the local wavefront slope is calculated in different regions of the pupil plane and modeled with a different function in each region, typically using polynomial functions.

In modal wavefront reconstruction, the wavefront over the entire pupil aperture is represented by an infinite sum expansion of orthogonal functions (Cubalchini, 1978). Unlike the zonal method, which separates the aperture into many subapertures, the modal method performs the wavefront estimation over the whole aperture by using a combination of linearly independent analytical functions (Hernández-Gómez, 2014). Normally, the most common analytical functions used to represent the wavefronts in modal estimation are Zernike polynomials. Southwell (1980) used Zernike polynomials to fit the measured slopes to do wavefront estimation. Compared with zonal estimation, modal methods are more suited when only a fixed number of slope sampling points are of interest. In addition, the computational process for modal methods is easier and faster.

In this thesis project modal wavefront reconstruction method was selected because the goal is to calculate the Zernike coefficients for wavefront aberrations. Detailed procedures related to the modal wavefront estimation will be described in following sections.

### **3.3 Zernike Polynomials**

Zernike polynomials are a set of continuous orthogonal functions defined on a unit circle and they have been broadly applied to characterize the aberration of optical instruments and of the eye (Born&Wolf, 1980, Malacara, 1992).

In polar coordinates  $(\rho, \theta)$ , a wavefront is expanded as:

$$W(\rho, \theta) = \sum_{n=0}^{\infty} \sum_{m=0}^n C_{nm} Z_n^m(\rho, \theta) \quad (\text{Eq.3.1})$$

where  $Z_n^m$  are the Zernike polynomials,  $C_{nm}$  are the Zernike expansion coefficients,  $n$  and  $m$  are positive integers such that  $n - m \geq 0$ . Figure 3.1 shows the coordinate system of a point Q within a unit circle that represents the exit pupil of an imaging system.

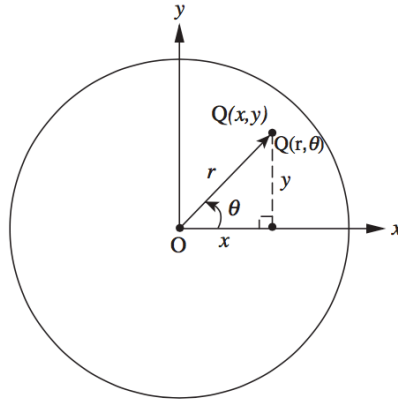


Figure 3.1 Cartesian and polar coordinates  $(x, y)$  and  $(r, \theta)$ , respectively, of a pupil point Q in the plane of the exit pupil (Malacara, 2007).

The Zernike polynomials can be expressed as:

$$Z_n^m(\rho, \theta) = \left[ \frac{2(n+1)}{1 + \delta_{m0}} \right]^{\frac{1}{2}} R_n^m(\rho) \cos(m\theta) \quad (\text{Eq.3.2})$$

where  $\delta_{ij}$  is the Kronecker delta, and  $R_n^m(\rho)$  are the radial circle polynomials given by

$$R_n^m(\rho) = \sum_{s=0}^{\frac{n-m}{2}} \left( \frac{(-1)^s (n-s)!}{s! \left(\frac{n+m}{2} - s\right)! \left(\frac{n+m}{2} - s\right)!} \right) \rho^{n-2s} \quad (\text{Eq.3.3})$$

The Zernike coefficients are given by:

$$C_{nm} = \frac{1}{\pi} \int_0^1 \int_0^{2\pi} W(\rho, \theta) Z_n^m(\rho, \theta) \rho \partial \rho \partial \theta \quad (\text{Eq.3.4})$$

The algebraic expansions of the Zernike polynomials and their derivatives, which are used for the development of the wavefront reconstruction MATLAB program are shown in Table 3.1, Table 3.2, and Table 3.3 in the Cartesian coordinate system.

<i>n</i>	<i>m</i>	$Z_n^m$	RMS	Polar form ( $dx^2 \rightarrow r d\theta dr$ )	Cartesian form ( $dx^2 \rightarrow dx dy$ )
0	0	$Z_0^0$	$\sqrt{2}$	1	1
1	-1	$Z_1^{-1}$	2	$r \sin \theta$	<i>x</i>
1	1	$Z_1^1$	2	$r \cos \theta$	<i>y</i>
2	-2	$Z_2^{-2}$	$\sqrt{6}$	$r^2 \sin 2\theta$	2 <i>xy</i>
2	0	$Z_2^0$	$\sqrt{3}$	$2r^2 - 1$	$-1 + 2x^2 + 2y^2$
2	2	$Z_2^2$	$\sqrt{6}$	$r^2 \cos 2\theta$	$-x^2 + y^2$
3	-3	$Z_3^{-3}$	$2\sqrt{2}$	$r^3 \sin 3\theta$	$-x^3 + 3xy^2$
3	-1	$Z_3^{-1}$	$2\sqrt{2}$	$(3r^3 - 2r) \sin \theta$	$-2x + 3x^3 + 3xy^2$
3	1	$Z_3^1$	$2\sqrt{2}$	$(3r^3 - 2r) \cos \theta$	$-2y + 3y^3 + 3x^2y$
3	3	$Z_3^3$	$2\sqrt{2}$	$r^3 \cos 3\theta$	$y^3 - 3x^2y$
4	-4	$Z_4^{-4}$	$\sqrt{10}$	$r^4 \sin 4\theta$	$-4x^3y + 4xy^3$
4	-2	$Z_4^{-2}$	$\sqrt{10}$	$(4r^4 - 3r^2) \sin 2\theta$	$-6xy + 8x^3y + 8xy^3$
4	0	$Z_4^0$	$\sqrt{5}$	$6r^4 - 6r^2 + 1$	$1 - 6x^2 - 6y^2 + 6x^4 + 12x^2y^2 + 6y^4$
4	2	$Z_4^2$	$\sqrt{10}$	$(4r^4 - 3r^2) \cos 2\theta$	$3x^2 - 3y^2 - 4x^4 + 4y^4$
4	4	$Z_4^4$	$\sqrt{10}$	$r^4 \cos 4\theta$	$x^4 - 6x^2y^2 + y^4$
5	-5	$Z_5^{-5}$	$2\sqrt{3}$	$r^5 \sin 5\theta$	$x^5 - 10x^3y^2 + 5xy^4$
5	-3	$Z_5^{-3}$	$2\sqrt{3}$	$(5r^5 - 4r^3) \sin 3\theta$	$4x^3 - 12xy^2 - 5x^5 + 10x^3y^2 + 15xy^4$
5	-1	$Z_5^{-1}$	$2\sqrt{3}$	$(10r^5 - 12r^3 + 3r) \sin \theta$	$3x - 12x^3 - 12xy^2 + 10x^5 + 20x^3y^2 + 10xy^4$
5	1	$Z_5^1$	$2\sqrt{3}$	$(10r^5 - 12r^3 + 3r) \cos \theta$	$3y - 12y^3 - 12x^2y + 10y^5 + 20x^2y^3 + 10x^4y$
5	3	$Z_5^3$	$2\sqrt{3}$	$(5r^5 - 4r^3) \cos 3\theta$	$-4y^3 + 12x^2y + 5y^5 - 10x^2y^3 - 15x^4y$
5	5	$Z_5^5$	$2\sqrt{3}$	$r^5 \cos 5\theta$	$y^5 - 10x^2y^3 + 5x^4y$
6	-6	$Z_6^{-6}$	$\sqrt{14}$	$r^6 \sin 6\theta$	$6x^5y - 20x^3y^3 + 6xy^5$
6	-4	$Z_6^{-4}$	$\sqrt{14}$	$(6r^6 - 5r^4) \sin 4\theta$	$20x^3y - 20xy^3 - 24x^5y + 24xy^5$
6	-2	$Z_6^{-2}$	$\sqrt{14}$	$(15r^6 - 20r^4 + 6r^2) \sin 2\theta$	$12xy - 40x^3y - 40xy^3 + 30x^5y + 60x^3y^3 - 30xy^5$
6	0	$Z_6^0$	$\sqrt{7}$	$20r^6 - 30r^4 + 12r^2 - 1$	$-1 + 12x^2 + 12y^2 - 30x^4 - 60x^2y^2 - 30y^4 + 20x^6 + 60x^4y^2 + 60x^2y^4 + 20y^6$
6	2	$Z_6^2$	$\sqrt{14}$	$(15r^6 - 20r^4 + 6r^2) \cos 2\theta$	$-6x^2 + 6y^2 + 20x^4 - 20y^4 - 15x^6 - 15x^4y^2 + 15x^2y^4 + 15y^6$
6	4	$Z_6^4$	$\sqrt{14}$	$(6r^6 - 5r^4) \cos 4\theta$	$-5x^4 + 30x^2y^2 - 5y^4 + 6x^6 - 30x^4y^2 - 30x^2y^4 + 6y^6$
6	6	$Z_6^6$	$\sqrt{14}$	$r^6 \cos 6\theta$	$-x^6 + 15x^4y^2 - 15x^2y^4 + y^6$
7	-7	$Z_7^{-7}$	4	$r^7 \sin 7\theta$	$-x^7 + 21x^5y^2 - 35x^3y^4 + 7xy^6$
7	-5	$Z_7^{-5}$	4	$(7r^7 - 6r^5) \sin 5\theta$	$-6x^5 + 60x^3y^2 - 30xy^4 + 7x^7 - 63x^5y^2 - 35x^3y^4 + 35xy^6$
7	-3	$Z_7^{-3}$	4	$(2r^7 - 30r^5 + 10r^3) \sin 3\theta$	$-10x^3 + 30xy^2 + 30x^5 - 60x^3y^2 - 90xy^4 - 21x^7 + 21x^5y^2 + 105x^3y^4 + 63xy^6$
7	-1	$Z_7^{-1}$	4	$(35r^7 - 60r^5 + 30r^3 - 4r) \sin \theta$	$-4x + 30x^3 + 30xy^2 - 60x^5 - 120x^3y^2 - 60xy^4 + 35x^7 + 105x^5y^2 + 105x^3y^4 + 35xy^6$
7	1	$Z_7^1$	4	$(35r^7 - 60r^5 + 30r^3 - 4r) \cos \theta$	$-4y + 30y^3 + 30x^2y - 60y^5 - 120x^2y^3 - 60x^4y + 35y^7 + 105x^2y^5 + 105x^4y^3 + 35x^6y$
7	3	$Z_7^3$	4	$(2r^7 - 30r^5 + 10r^3) \cos 3\theta$	$10y^3 - 30x^2y - 30y^5 + 60x^2y^3 + 90x^4y + 21y^7 - 21x^2y^5 - 105x^4y^3 + 63x^6y$
7	5	$Z_7^5$	4	$(7r^7 - 6r^5) \cos 5\theta$	$-6y^5 + 60x^2y^3 - 30x^4y + 7y^7 - 63x^2y^5 - 35x^4y^3 + 35x^6y$
7	7	$Z_7^7$	4	$r^7 \cos 7\theta$	$y^7 - 21x^2y^5 + 35x^4y^3 - 7x^6y$

Table 3.1 Algebraic expansion of the Zernike Polynomial Sequence, orders from one to seven (Lakshminarayanan & Fleck, 2011).

Equation # for MATLAB Program	n	m	$Z_n^m$	RMS	Cartesian form partial derivatives $V_x = \frac{\partial Z}{\partial x}$
1	0	0	$Z_0^0$	$\sqrt{2}$	0
2	1	-1	$Z_1^{-1}$	2	2
3	1	1	$Z_1^1$	2	0
4	2	-2	$Z_2^{-2}$	$\sqrt{6}$	2y
5	2	0	$Z_2^0$	$\sqrt{3}$	4x
6	2	2	$Z_2^2$	$\sqrt{6}$	-2x
7	3	-3	$Z_3^{-3}$	$2\sqrt{2}$	$-3x^2 + 3y^2$
8	3	-1	$Z_3^{-1}$	$2\sqrt{2}$	$-2 + 9x^2 + 3y^2$
9	3	1	$Z_3^1$	$2\sqrt{2}$	6xy
10	3	3	$Z_3^3$	$2\sqrt{2}$	-6xy
11	4	-4	$Z_4^{-4}$	$\sqrt{10}$	$-12x^2y + 4y^3$
12	4	-2	$Z_4^{-2}$	$\sqrt{10}$	$-6y + 24x^2y + 8y^3$
13	4	0	$Z_4^0$	$\sqrt{5}$	$-12x + 24x^3 + 24xy^2$
14	4	2	$Z_4^2$	$\sqrt{10}$	$6x - 16x^3$
15	4	4	$Z_4^4$	$\sqrt{10}$	$4x^3 - 12xy^2$
16	5	-5	$Z_5^{-5}$	$2\sqrt{3}$	$5x^4 - 30x^2y^2 + 5y^4$
17	5	-3	$Z_5^{-3}$	$2\sqrt{3}$	$12x^2 - 12y^2 - 25y^4 + 30x^2y^2 + 15y^4$
18	5	-1	$Z_5^{-1}$	$2\sqrt{3}$	$3 - 36x^2 - 12y^2 + 50x^4 + 60x^2y^2 + 10y^4$
19	5	1	$Z_5^1$	$2\sqrt{3}$	$-24xy + 40xy^3 + 40x^3y$
20	5	3	$Z_5^3$	$2\sqrt{3}$	$24xy - 20xy^3 - 60x^3y$
21	5	5	$Z_5^5$	$2\sqrt{3}$	$-20xy^3 + 20x^3y$
22	6	-6	$Z_6^{-6}$	$\sqrt{14}$	$30x^4y - 60x^2y^3 + 6y^5$
23	6	-4	$Z_6^{-4}$	$\sqrt{14}$	$60x^2y - 20y^3 - 120x^4y + 24y^5$
24	6	-2	$Z_6^{-2}$	$\sqrt{14}$	$12y - 120x^2y - 40y^3 + 150x^4y + 180x^2y^3 - 30y^5$
25	6	0	$Z_6^0$	$\sqrt{7}$	$24x - 120x^3 - 120xy^2 + 120x^5 + 240x^3y^2 + 120xy^4$
26	6	2	$Z_6^2$	$\sqrt{14}$	$-12x + 80x^3 - 90x^5 - 60x^3y^2 + 30xy^4$
27	6	4	$Z_6^4$	$\sqrt{14}$	$-20x^3 + 60xy^2 + 36x^5 - 120x^3y^2 - 60xy^4$
28	6	6	$Z_6^6$	$\sqrt{14}$	$-6x^5 + 60x^3y^2 - 30xy^4$

Table 3.2 Algebraic expansions of partial derivatives over x of the Zernike polynomial sequence



Equation # for MATLAB Program	n	m	$Z_n^m$	RMS	Cartesian form partial derivatives $Vy = \frac{\partial Z}{\partial y}$
1	0	0	$Z_0^0$	$\sqrt{2}$	0
2	1	-1	$Z_1^{-1}$	2	0
3	1	1	$Z_1^1$	2	2
4	2	-2	$Z_2^{-2}$	$\sqrt{6}$	$2x$
5	2	0	$Z_2^0$	$\sqrt{3}$	$4y$
6	2	2	$Z_2^2$	$\sqrt{6}$	$2y$
7	3	-3	$Z_3^{-3}$	$2\sqrt{2}$	$6xy$
8	3	-1	$Z_3^{-1}$	$2\sqrt{2}$	$6xy$
9	3	1	$Z_3^1$	$2\sqrt{2}$	$-2 + 9y^2 + 3x^2$
10	3	3	$Z_3^3$	$2\sqrt{2}$	$3y^2 - 3x^2$
11	4	-4	$Z_4^{-4}$	$\sqrt{10}$	$-4y^3 + 12xy^2$
12	4	-2	$Z_4^{-2}$	$\sqrt{10}$	$-6x + 8x^3 + 24xy^2$
13	4	0	$Z_4^0$	$\sqrt{5}$	$-12y + 24x^2y + 24y^3$
14	4	2	$Z_4^2$	$\sqrt{10}$	$-6y + 16y^3$
15	4	4	$Z_4^4$	$\sqrt{10}$	$-12x^2y + 4y^3$
16	5	-5	$Z_5^{-5}$	$2\sqrt{3}$	$-20x^3y + 20xy^3$
17	5	-3	$Z_5^{-3}$	$2\sqrt{3}$	$-24xy + 20x^3y + 60xy^3$
18	5	-1	$Z_5^{-1}$	$2\sqrt{3}$	$-24xy + 40x^3y + 40xy^3$
19	5	1	$Z_5^1$	$2\sqrt{3}$	$3 - 36y^2 - 12x^2 + 50y^4 + 60x^2y^2 + 10x^4$
20	5	3	$Z_5^3$	$2\sqrt{3}$	$-12y^2 + 12x^2 + 25y^4 - 30x^2y^2 - 15x^4$
21	5	5	$Z_5^5$	$2\sqrt{3}$	$5y^4 - 30x^2y^2 + 5x^4$
22	6	-6	$Z_6^{-6}$	$\sqrt{14}$	$6x^5 - 60x^3y^2 + 30xy^4$
23	6	-4	$Z_6^{-4}$	$\sqrt{14}$	$20x^3 - 60xy^2 - 24x^5 + 120xy^4$
24	6	-2	$Z_6^{-2}$	$\sqrt{14}$	$12x - 40x^3 - 120xy^2 + 30x^5 + 180x^3y^2 - 150xy^4$
25	6	0	$Z_6^0$	$\sqrt{7}$	$24y - 120x^2y - 120y^3 + 120x^4y + 240x^2y^3 + 120y^5$
26	6	2	$Z_6^2$	$\sqrt{14}$	$12y - 80y^3 - 30x^4y + 60x^2y^3 + 90y^5$
27	6	4	$Z_6^4$	$\sqrt{14}$	$60x^2y - 20y^3 - 60x^4y - 120x^2y^3 + 36y^5$
28	6	6	$Z_6^6$	$\sqrt{14}$	$30x^4y - 60x^2y^3 + 6y^5$

Table 3.3 Algebraic expansions of partial derivatives over y of the Zernike polynomial sequence

### 3.4 Wavefront Reconstruction

The wavefront is represented by a function  $W(x, y)$ :

$$W(x, y) = \sum_{k=1}^K a_k Z_k(x, y) \quad (\text{Eq.3.5})$$

where  $K$  represent the total number of Zernike polynomial terms,  $a_k$  represent the  $k^{\text{th}}$  Zernike coefficient, and  $Z_k$  represent the  $k^{\text{th}}$  Zernike polynomial.

At any positions  $(x_i, y_j)$  in the pupil coordinate system where ray slope is measured, the ray slope and wavefront are related by

$$S_x(x_i, y_j) = \frac{\partial W}{\partial x}(x_i, y_j) \quad (\text{Eq.3.6})$$

$$S_y(x_i, y_j) = \frac{\partial W}{\partial y}(x_i, y_j) \quad (\text{Eq.3.7})$$

The range of  $i$  and  $j$  is from 1 to  $N$  and  $M$ .  $N$  represents the total number of columns of the sampling matrix and  $M$  represents the total number of rows of the sampling matrix, and  $N$  generally equals to  $M$ .

The relationship between the measured slope  $S$  from LRT experiments and the Zernike coefficients can be written as:

$$S = aV \quad (\text{Eq.3.8})$$

where  $S$  is a vector with  $2M \times N$  elements that contains all of the slope measurements. Typically, the upper half of the vector represents the  $x$  slope information and the bottom half of the matrix represents the  $y$  slope information.

$$\mathbf{S} = \begin{bmatrix} \frac{\partial W(x_1, y_1)}{\partial x} \\ \frac{\partial W(x_2, y_1)}{\partial x} \\ \vdots \\ \frac{\partial W(x_N, y_M)}{\partial x} \\ \frac{\partial W(x_1, y_1)}{\partial y} \\ \frac{\partial W(x_2, y_1)}{\partial y} \\ \vdots \\ \frac{\partial W(x_N, y_M)}{\partial y} \end{bmatrix} \quad (\text{Eq.3.9})$$

And  $\mathbf{a}$  is the vector of the Zernike coefficients that describes the contribution of each fitting polynomial to the reconstructed wavefront.

$$\mathbf{a} = \begin{bmatrix} a_1 \\ a_2 \\ a_3 \\ a_4 \\ \vdots \\ a_K \end{bmatrix} \quad (\text{Eq.3.10})$$

The matrix  $\mathbf{V}$  is a  $2M \times N$  rows by  $K$  columns matrix that contain the derivatives of the Zernike polynomials  $\mathbf{Z}$ :

$$\mathbf{V} = \begin{bmatrix} \frac{\partial Z_1(x_1, y_1)}{\partial x} & \dots & \frac{\partial Z_2(x_1, y_1)}{\partial x} & \dots & \frac{\partial Z_K(x_1, y_1)}{\partial x} \\ \frac{\partial Z_1(x_2, y_1)}{\partial x} & \dots & \frac{\partial Z_2(x_2, y_1)}{\partial x} & \dots & \frac{\partial Z_K(x_2, y_1)}{\partial x} \\ \vdots & \dots & \vdots & \dots & \vdots \\ \frac{\partial Z_1(x_N, y_M)}{\partial x} & \dots & \frac{\partial Z_2(x_N, y_M)}{\partial x} & \dots & \frac{\partial Z_K(x_N, y_M)}{\partial x} \\ \frac{\partial Z_1(x_1, y_1)}{\partial y} & \dots & \frac{\partial Z_2(x_1, y_1)}{\partial y} & \dots & \frac{\partial Z_K(x_1, y_1)}{\partial y} \\ \frac{\partial Z_1(x_2, y_1)}{\partial y} & \dots & \frac{\partial Z_2(x_2, y_1)}{\partial y} & \dots & \frac{\partial Z_K(x_2, y_1)}{\partial y} \\ \vdots & \dots & \vdots & \dots & \vdots \\ \frac{\partial Z_1(x_N, y_M)}{\partial y} & \dots & \frac{\partial Z_2(x_N, y_M)}{\partial y} & \dots & \frac{\partial Z_K(x_N, y_M)}{\partial y} \end{bmatrix} \quad (\text{Eq.3.11})$$

The top half of the matrix  $V$  corresponds to the  $x$  derivatives of the Zernike polynomials and the bottom half of the matrix  $V$  corresponds to the  $y$  derivatives of the Zernike polynomials.

In practice, matrix equation  $S = aV$  is overdetermined. There are more sampling points,  $2M \times N$ , than the number of the Zernike coefficients  $a$ . Therefore, the equation cannot be solved directly and a least square solution is used to fit the slope measurements vector  $S$  to a set of derivatives of the Zernike polynomials  $Z$  (Cubalchini, 1978, Southwell, 1980).

The least square method produces the fitting equation for the Zernike coefficients:

$$a = [V^T V]^{-1} V^T S \quad (\text{Eq.3.12})$$

### 3.5 Implementation in MATLAB

The aim of this project is to develop a MATLAB program to determine the Zernike coefficients of *in vitro* crystalline lenses measured using the LRT system. The MATLAB program was designed to calculate the first 28 Zernike polynomial terms, up to the 6<sup>th</sup> order.

The developed MATLAB program was separated into several steps to obtain the Zernike coefficients.

- Input  $x$  and  $y$  sampling positions
- Determine matrix  $V$

- Input the local wavefront slopes from LRT system experiments to determine matrix  $\mathbf{S}$ .
- Calculation of Zernike coefficients through matrix manipulation (Eq.3.12).

### 3.6 Testing

A wavefront reconstruction program was written in MATLAB to test the developed calculation algorithm for Zernike Coefficients. The general steps of the test program are shown below.

- Input Zernike coefficients matrix  $\mathbf{a}_i$
- Calculate slopes  $\mathbf{S}$
- Use slopes  $\mathbf{S}$  as input to calculate Zernike coefficients  $\mathbf{a}_0$
- Compare  $\mathbf{a}_i$  and  $\mathbf{a}_0$

The sample geometry selected for the test was a 7x7 grid with total of 49 sampling positions within a unit circle. The values for the given Zernike coefficients were taken from a published paper for a cynomolgus monkey lens (Roorda & Glasser, 2004). A defocus term was added to simulate the experimental condition of the LRT system, where the beam leaving the lens is focused. The amplitude of the defocus term was 33  $\mu\text{m}$ , corresponding to a cynomolgus lens with a power of 40 diopters.

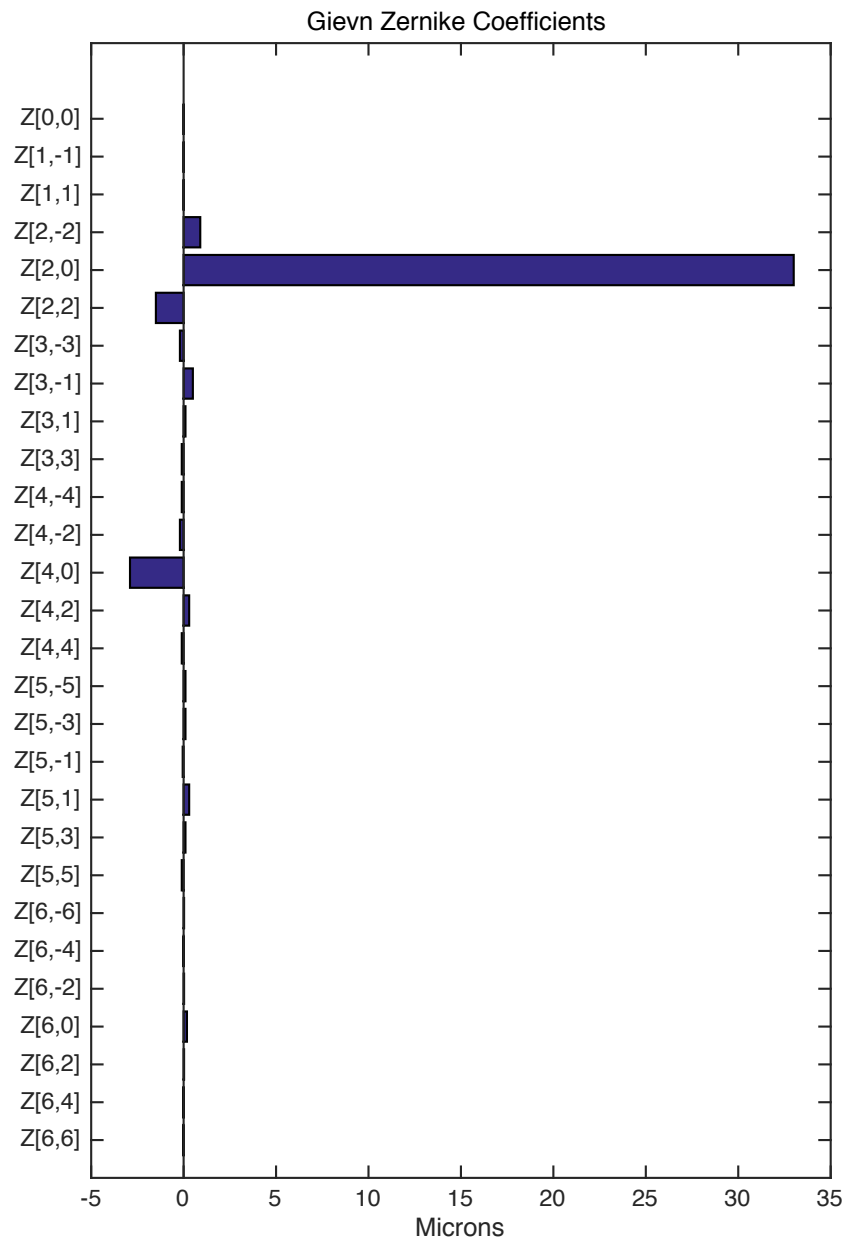


Figure 3.2 Given Zernike coefficients  $\alpha_i$ . The values for the Zernike coefficients were taken from a published paper for cynomolgus monkey eyes (Roorda & Glasser, 2004).

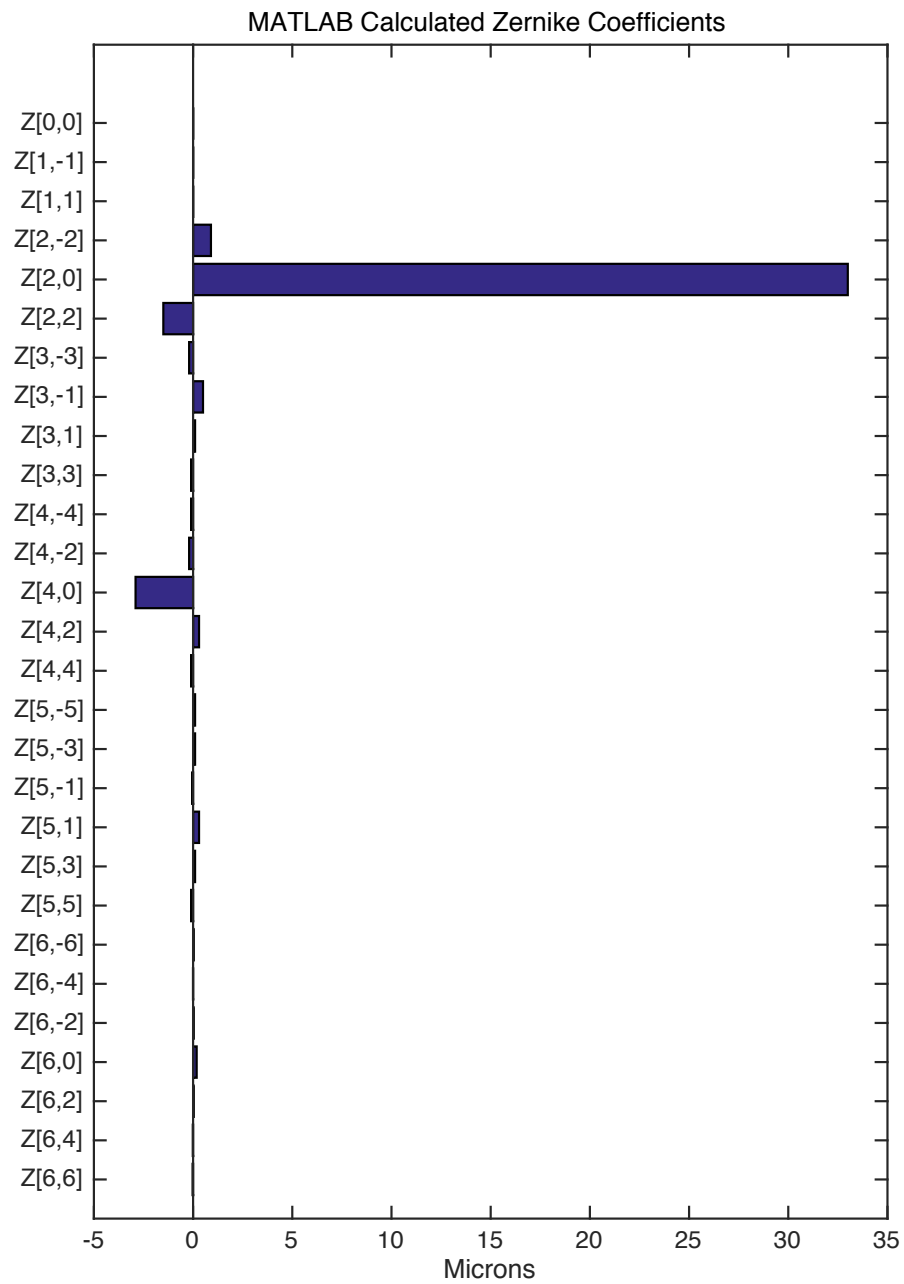


Figure 3.3 Calculated Zernike coefficients  $\alpha_0$ .

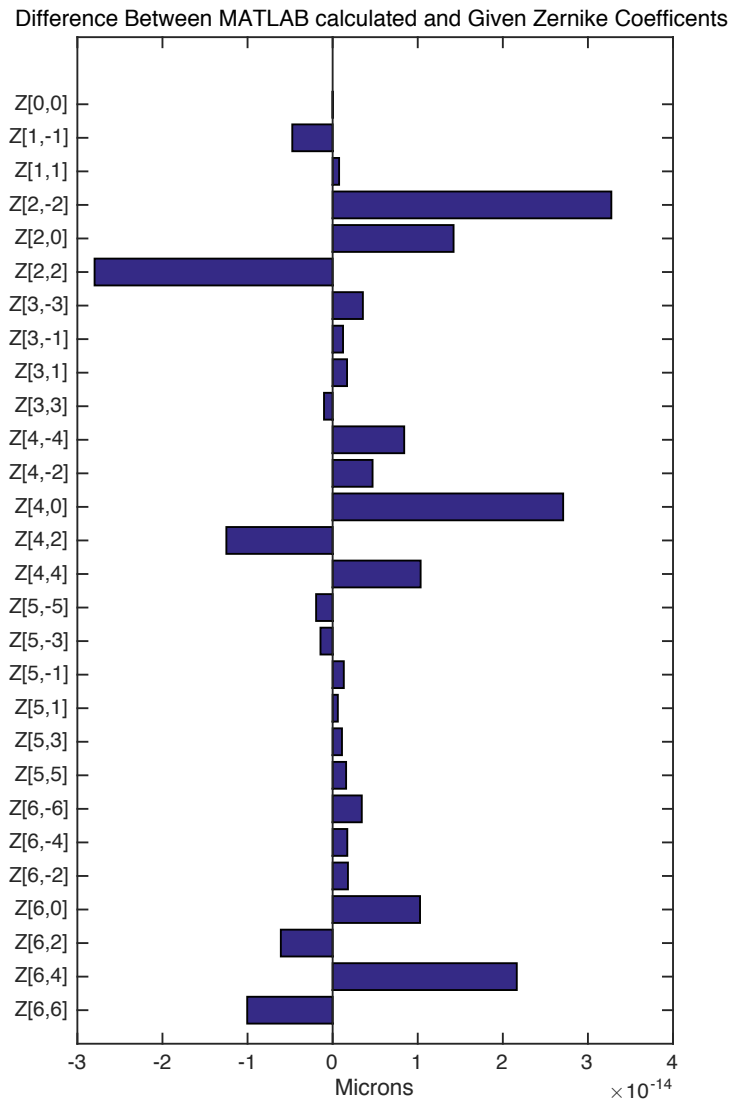


Figure 3.4 Difference between Given Zernike coefficients  $a_i$  and calculated Zernike coefficients  $a_0$ . The difference is on the scale of  $10^{-14}$ .



The reconstructed Zernike coefficients were equal (within  $10^{-14}$ ) to the input Zernike coefficients. This simulation indicates that the general Zernike coefficient calculation algorithm is accurate. It will be applied to the experimental data from LRT system with certain modifications that are described in Chapter 4.

### **3.7 Summary**

In summary, this chapter demonstrated the general principles of the Zernike wavefront reconstruction and the calculation algorithm of the MATLAB program. The developed calculation algorithm was tested using simulation and the results showed the feasibility of using the program to reconstruct the Zernike coefficients. In next chapter, the developed program will be applied to reconstruct the Zernike coefficients for glass lenses, cynomolgus lenses, and human lenses from the LRT recorded spot patterns.

## CHAPTER 4

### APPLICATION TO THE LRT SYSTEM

#### 4.1 Purpose

This chapter describes the application of the developed MATLAB program to obtain the Zernike coefficients from experimental data recorded from the LRT system on *in vitro* crystalline lens experiments. The Zernike coefficients for two glass lenses, two cynomolgus lenses, and two human lenses were calculated.

#### 4.2 Experimental Setup

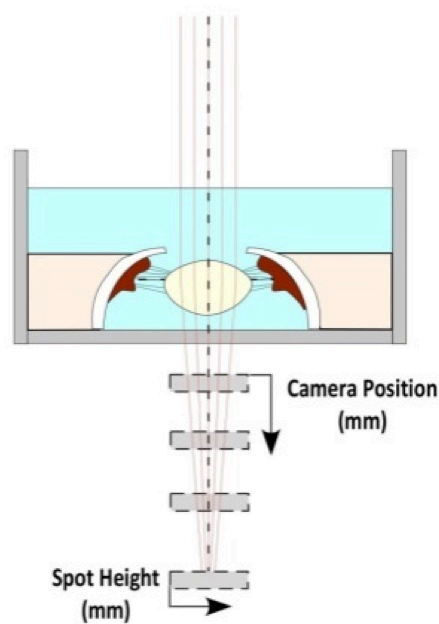


Figure 4.1 Experimental Setup. The LRT uses the source and beam delivery of a Spectral-Domain OCT system to deliver input rays onto the crystalline lens sequentially. The camera is used to record the spots positions of each ray sequentially at different vertical camera positions. The recorded spot positions for each ray at different vertical camera positions are used to calculate the ray slopes for Zernike wavefront reconstruction (Maceo, 2015).

Figure 4.1 demonstrates the *in vitro* experimental set up of the LRT system. During the experiments, the LRT system uses the OCT delivery system to deliver input beams sequentially on the crystalline lenses and the spot positions for each ray are recorded on a camera at different vertical positions. The recorded spot positions along the vertical axis for each ray can be used to represent the trajectory of the ray, which will be applied for  $x$  and  $y$  slope determination and Zernike coefficients calculations.

### 4.3 Data Analysis

#### 4.3.1 Calculation of Spot Centroid Positions

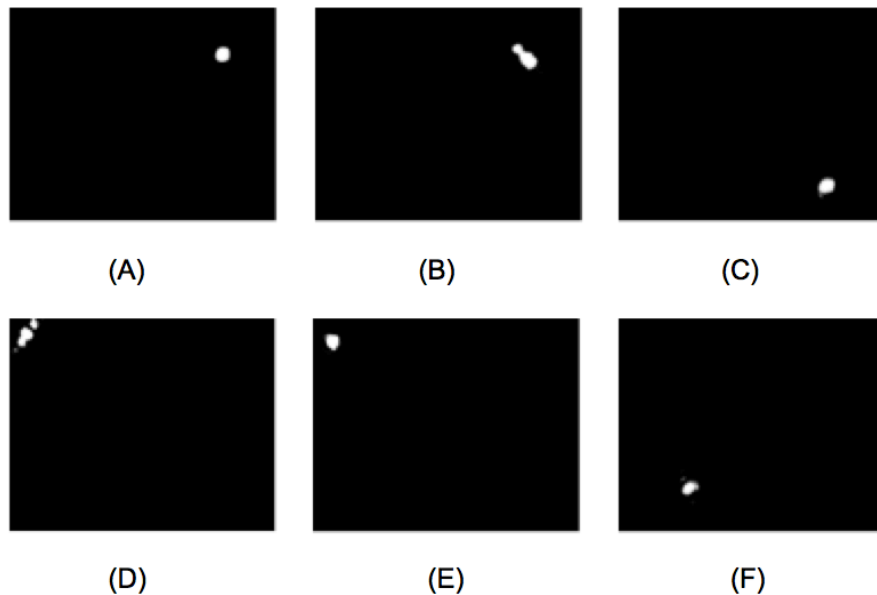


Figure 4.2 Examples of spot images recorded from the LRT system.

Figure 4.2 shows the camera recorded spot position images during the LRT experiments. In this experiment, for each camera position, there are a total of 621 laser rays passing through the crystalline lens sequentially and 621 images were formed containing spot position information. The combination of all 621 spots positions forms a 23 by 27 matrix. In order to find the input sampling geometry of the LRT system, an experiment without crystalline lens nor chamber was performed. The camera was placed at the position where the chamber would be. The spot positions obtained for all 621 rays were used as the  $x$  and  $y$  slope sampling positions.

The camera records the centroids of the spots in pixels. In order to determine the wavefront slopes, the spot positions recorded in pixels were converted to millimeters and shifted to center at the (0,0) positions for Zernike reconstruction. The LRT system uses a camera with a sensor sized 6.66 mm x 5.32 mm and a pixel size of 1280 x 1024. The following formulas are therefore used to convert spot positions data from pixel to mm:

$$x \text{ Spot positions (mm)} = \frac{6.66\text{mm}}{1280\text{pixels}} x \text{ pixels} \quad (\text{Eq.4.1})$$

$$y \text{ Spot positions(mm)} = \frac{5.32\text{mm}}{1024\text{pixels}} y \text{ pixels} \quad (\text{Eq.4.2})$$

Figure 4.3 illustrates the camera recorded spot positions geometry for all of the 621 rays without the lens chamber in place.

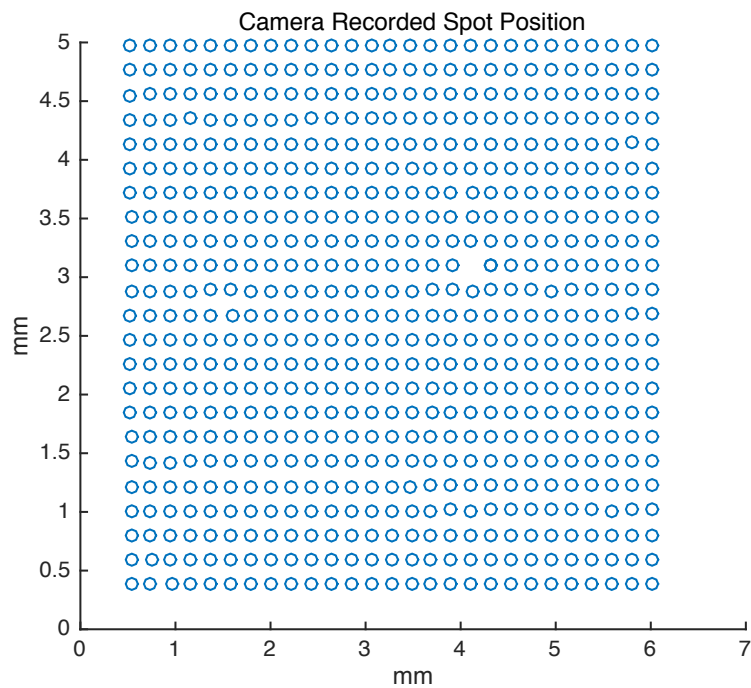


Figure 4.3 Camera recorded spot centroids positions without the presence of the chamber.

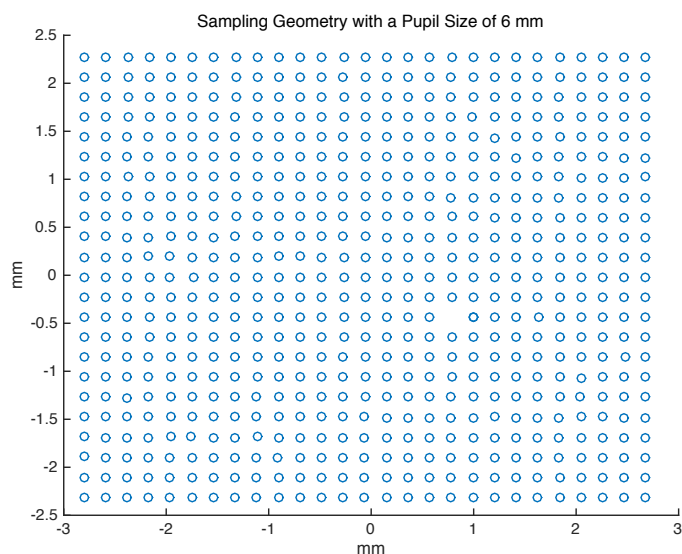


Figure 4.4 Spots positions for all of the 621 rays without the presence of the chamber. The spot positions recorded by the camera were shifted to center at the (0,0) position.

In Figure 4.4, the recorded spot positions were shifted and centered at the (0,0) position, which centers the pupil as required for the Zernike reconstruction.

The equations used to center the recorded spot positions are:

$$x \text{ Centered spot positions} = x \text{ Spot positions} - 3.33\text{mm} \quad \text{Eq.4.3}$$

$$y \text{ Centered spot positions} = 2.66\text{mm} - y \text{ Spot positions} \quad \text{Eq.4.4}$$

### 4.3.2 Pupil Scaling

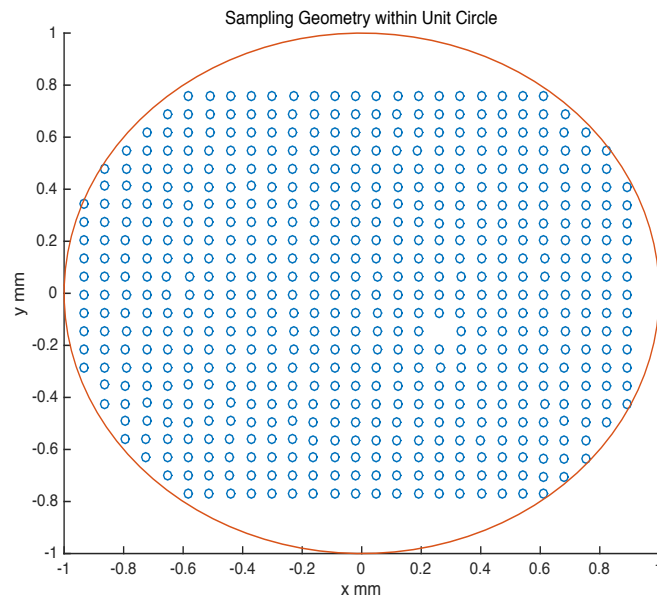


Figure 4.5 Sampling geometry of the Zernike wevfront reconstruction within unit circle. All of the 621 rays form a 23 by 27 matrix. Some of the spot positions were recorded outside of the unit circle and therefore eliminated for the wavefront reconstruction.

Zernike polynomials only satisfy the orthogonality condition over the unit circle. For the same wavefront error, different pupil sizes will result in different Zernike expansion coefficients. The coordinates of the spot positions therefore need to be scaled to the size of a unit circle first to perform Zernike coefficient

calculation. Figure 4.5 shows the sampling geometry of the waveform reconstruction within a unit circle with scaled coordinates.

### 4.3.3 Slope Measurements

Linear fits of  $x$  and  $y$  spots positions as a function of the axial positions of the camera were used to calculate the  $x$  slopes and  $y$  slopes. Figure 4.6 demonstrates the LRT beam propagation along the  $z$ -direction.

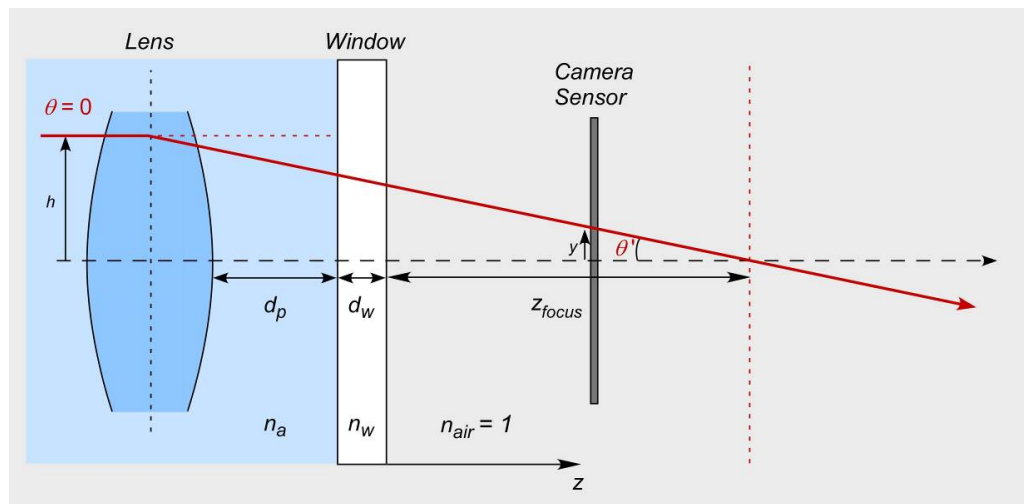


Figure 4.6 Schematic of LRT beam propagating through the lens along the  $z$ -direction.  $h$  is the entrance ray height,  $\theta$  is the incident angle ( $\theta=0$ ),  $d_p$  is the distance between the posterior surface of the lens and the window of the tissue chamber,  $n_a$  is the refractive index of the medium,  $d_w$  is the thickness of the window,  $n_w$  is the refractive index of the glass window,  $n_{air}$  is the refractive index of air ( $n_{air}=1$ ),  $y$  is the ray height incident on the camera,  $\theta' = dy/dz$  is the output ray slope, and  $z_{focus}$  is the distance between the posterior window surface and the intersection of the lens focus along the optical axis (Maceo et al., 2015).

The camera record spots positions in both  $x$  direction and  $y$  direction.

The output ray slope for a single beam in  $x$  direction is:

$$x \text{ Slope} = dx/dz \quad (\text{Eq.4.5})$$

The output ray slope for a single beam in  $y$  direction is:

$$y \text{ Slope} = dy/dz \quad (\text{Eq.4.6})$$

An example of the slope calculations of the experimental recorded image data for a cynomolgus lens is shown below. Figure 4.7 shows the centered camera recorded image spots positions from  $z=1$  mm to  $z=8$  mm.

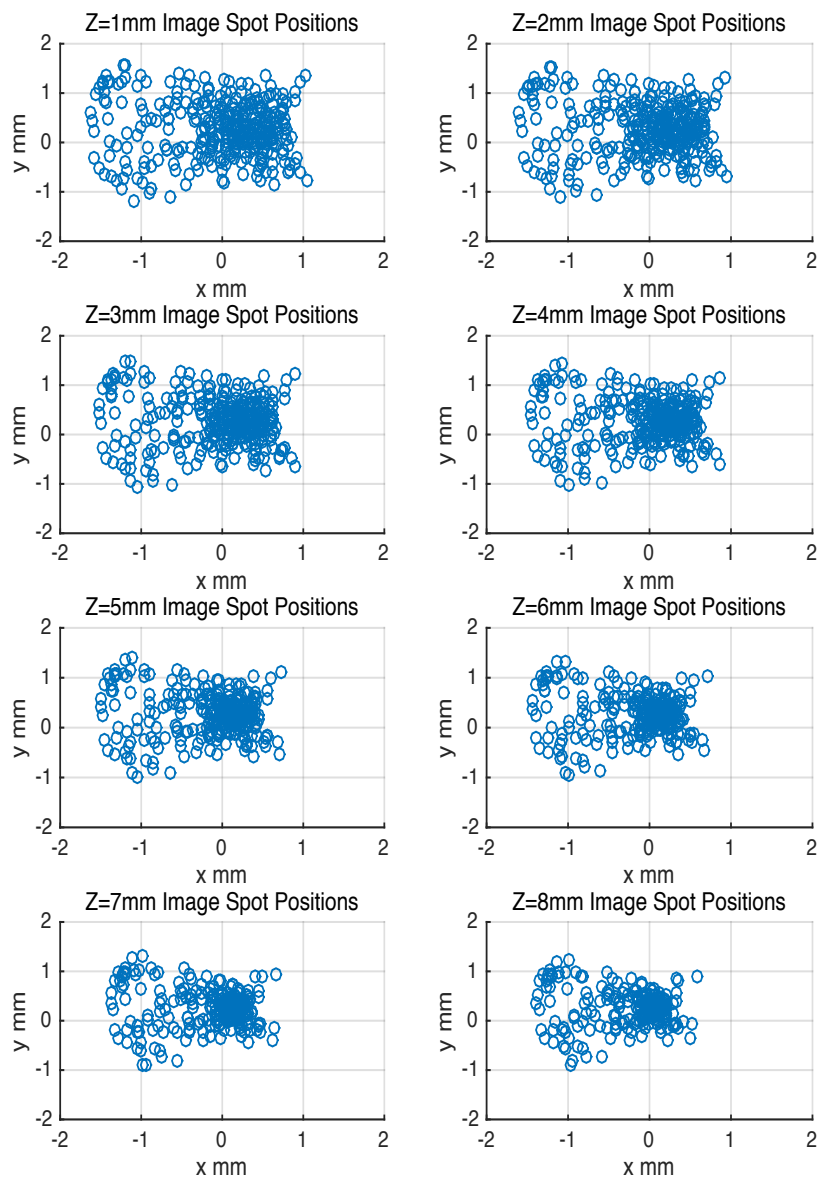


Figure 4.7 Centered camera recorded spots positions for rays within a circle of 6 diameter from  $z=1$ mm to  $z=8$ mm



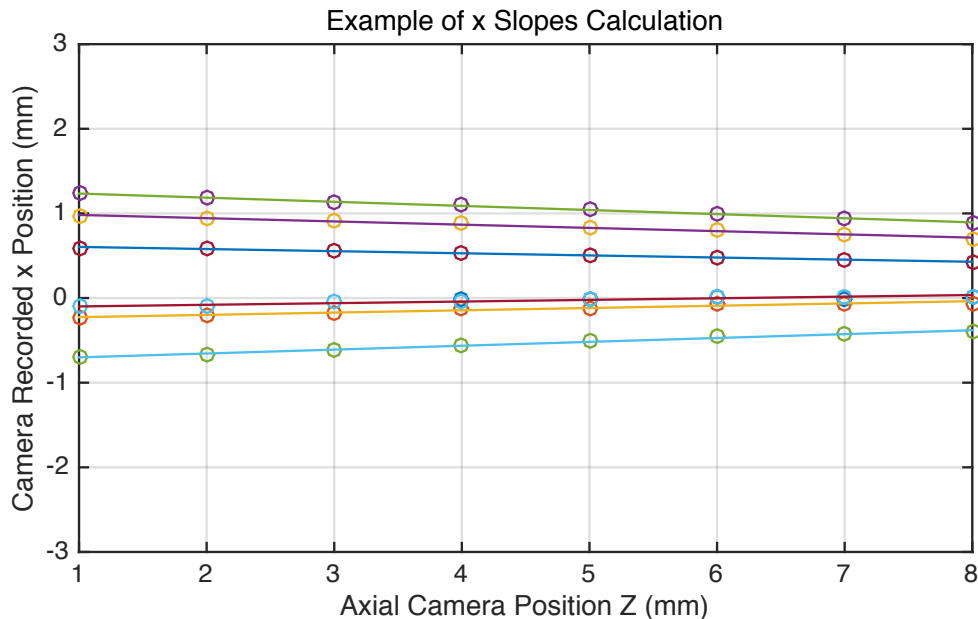


Figure 4.8 Examples of x slopes calculation. The 6 rays were picked from the locations where the camera recorded y positions=0.

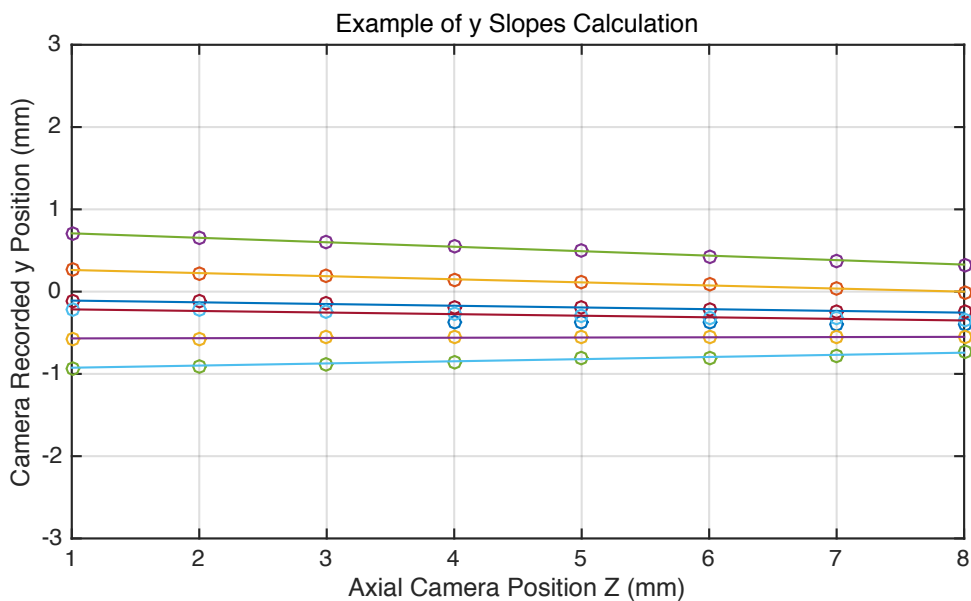


Figure 4.9 Examples of y slopes calculation. The 6 rays were picked from the locations where the camera recorded x positions=0.

In Figure 4.7, each recorded spot represents a laser ray. The rays passing through the crystalline lens become more focused along the z direction from  $z=1\text{mm}$  to  $z=8\text{mm}$ . Figure 4.8 shows the linear fits for 6 rays picked from the

horizontal axis ( $y=0$ ). Figure 4.9 shows the linear fits for 6 rays picked from the vertical axis ( $x=0$ ). The  $x$  slopes and  $y$  slopes are obtained by performing a linear regression. The MATLAB program performs linear fits for all of the rays within the defined pupil radius in both  $x$  and  $y$  directions to output a slope matrix  $S$ , which will be used for Zernike coefficients calculation. In this particular example, the pupil radius was 1.5mm.

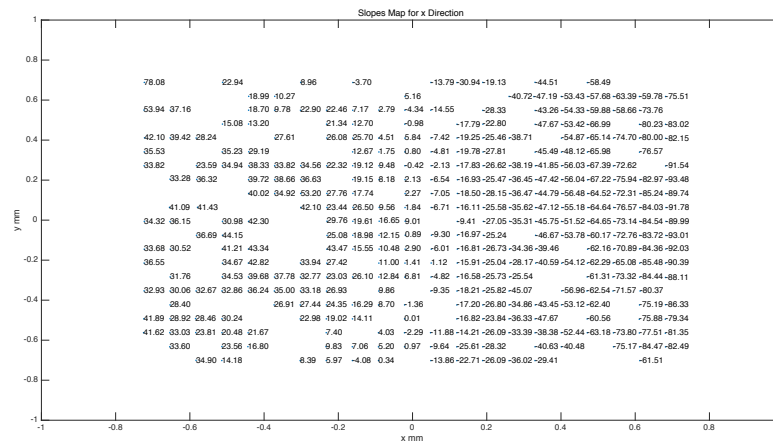


Figure 4.10 Example of an output slope matrix for x-slope. The location of the labeled slope outputs corresponds to the location of the input laser beams in the sampling geometry used. Some of the camera recorded images do not have good spots. The image data in these locations are discarded. The calculated slope values are multiplied by 1000 on the map for easy reading purpose.

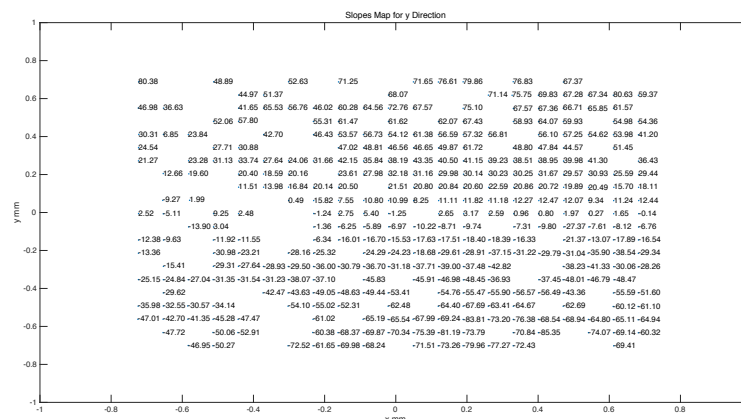


Figure 4.11 Example of an output slope matrix for y-slope. The location of the labeled slope outputs corresponds to the location of the input laser beams in the sampling geometry used. Some of the camera recorded images do not have good spots. The image data in these locations are discarded. The calculated slope values are multiplied by 1000 on the map for easy reading purpose.

#### 4.3.4 Calculation of Zernike Coefficients

According to the Eq.3.12 in chapter 3, Zernike coefficients can be calculated from known matrix  $V$  and the measured slope matrix  $S$ . Different sampling geometries were used to perform the Zernike coefficients calculations for different lens experiments. Figure 4.12 shows the steps for the MATLAB program to calculate the Zernike coefficients.

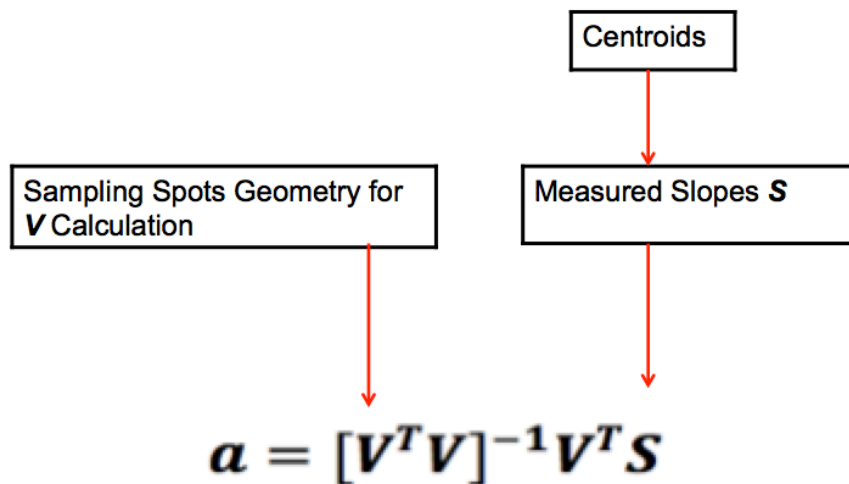


Figure 4.12 Principle of the MATLAB program to calculate the Zernike coefficients.

## 4.4 Experiments

### 4.4.1 Glass Lens, $f=18\text{mm}$

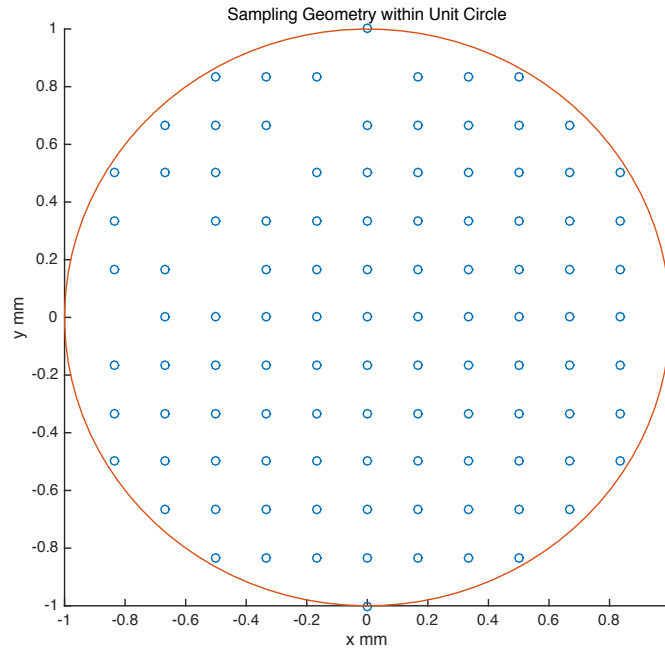


Figure 4.13 Sample geometry. The sample matrix was 13 rows by 13 columns. The matrix was scaled from the 3mm radius to the unit radius

In the experiment, a 12.5mm diameter Plano-convex glass lens with 18mm focal length (Edmund Scientific) was placed in the tissue chamber and properly aligned in the LRT system. The lens was placed on an O-ring in the chamber with the curved surface facing up. The motorized camera was used to capture images below the tissue chamber from  $z=0\text{mm}$ , which is very close to the tissue chamber, to  $z=8\text{mm}$ . The LRT system was programmed to deliver laser rays over a 6 mm pupil size with a 0.5 mm increment. A total of 169 spot images were acquired from the LRT system. The centroids of these spot images form a square matrix with 13 rows by 13 columns. Since Zernike polynomials are defined within a unit circle for wavefront reconstruction, the sampling geometry is scaled to fit

into a unit circle. Figure 4.13 shows the scaled 105 sampling points used in this experiment. The missing sampling points within the unit circle related to the image quality of these rays. Following figures show the results of this glass lens experiment.

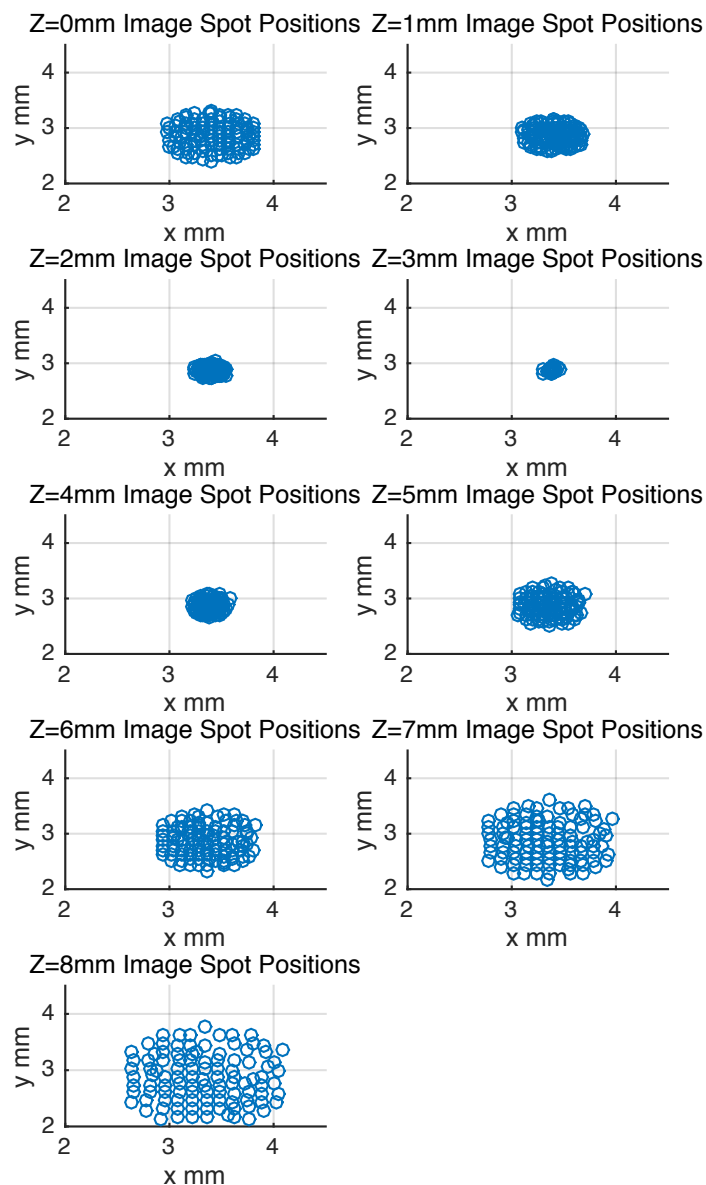


Figure 4.14 Camera recorded spots centroids from  $z=1\text{mm}$  to  $z=8\text{mm}$ . The sample matrix was 13 rows by 13 columns. The recorded spots centroids are used to calculate the ray slopes.

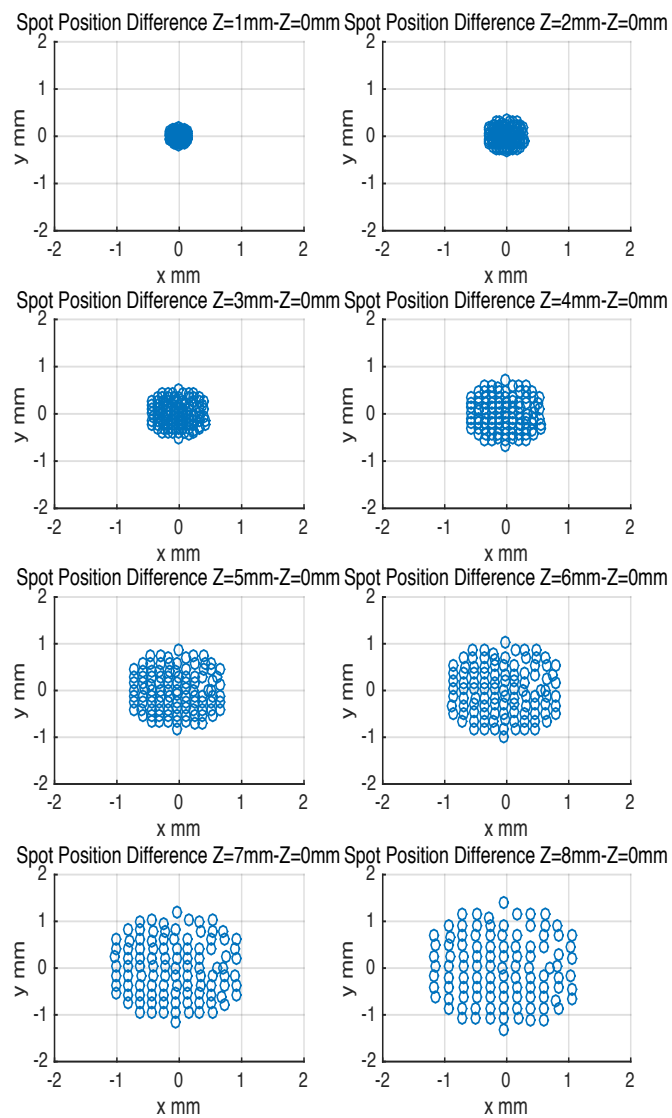


Figure 4.15 Camera recorded spots position differences along the z axis.

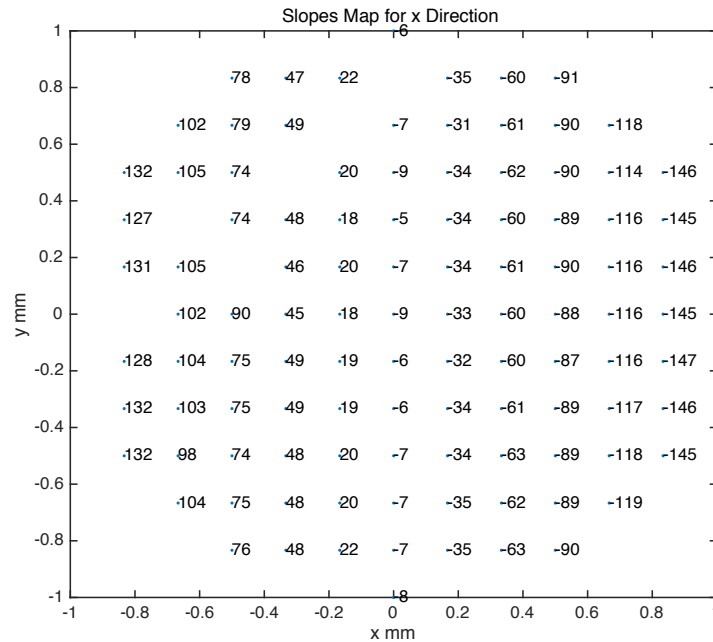


Figure 4.16 Output slope map for x direction. The calculated slope values were multiplied by 1000 on the map for easy reading purpose. The location of the labeled slope outputs corresponds to the location of laser beams in 13 rows by 13 columns sample geometry.

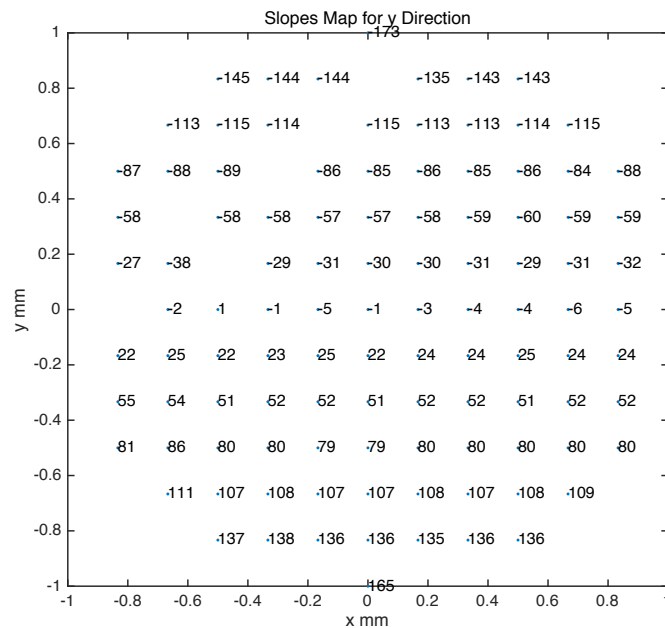


Figure 4.17 Output slope map for y direction. The calculated slope values were multiplied by 1000 on the map for easy reading purpose. The location of the labeled slope outputs corresponds to the location of laser beams in 13 rows by 13 columns sample geometry.

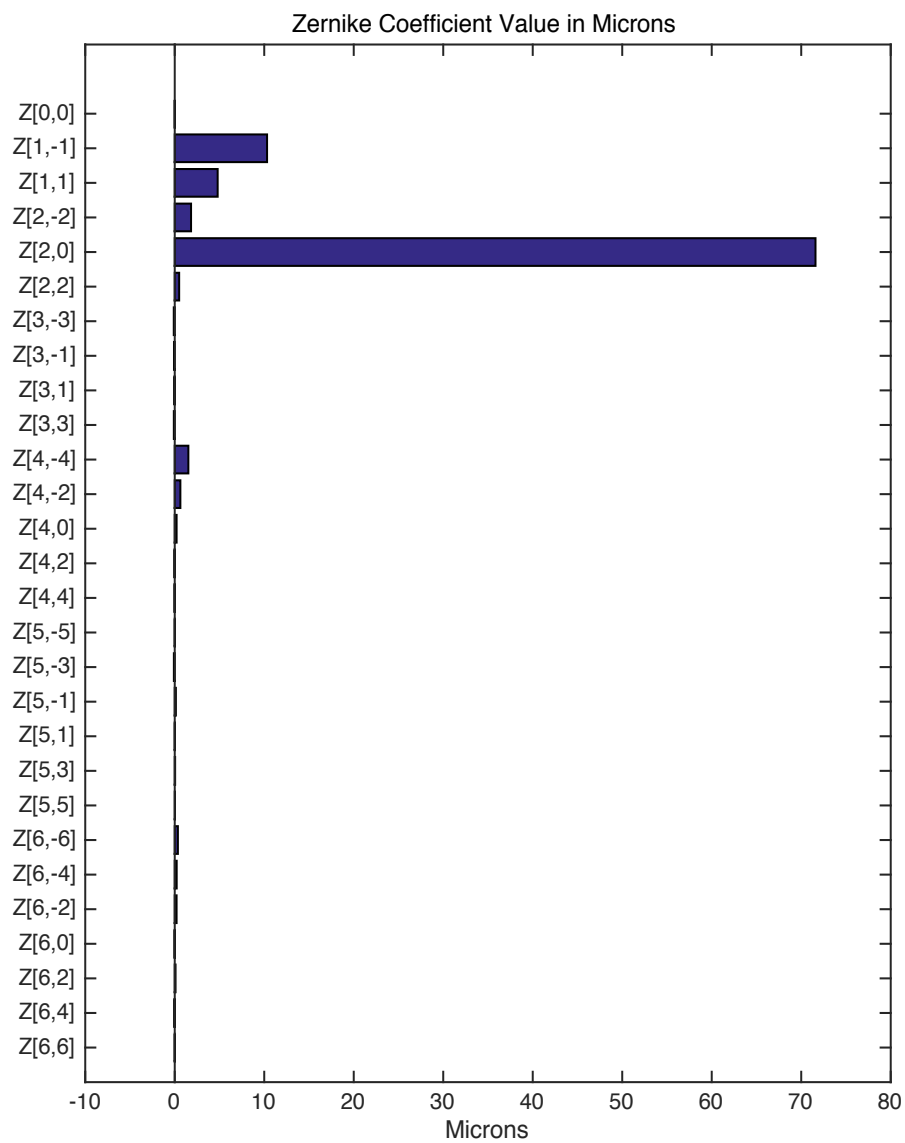


Figure 4.18 Zernike coefficients for the  $f=18\text{mm}$  glass lens. The sample geometry was 13 rows by 13 columns over a 6mm diameter zone.



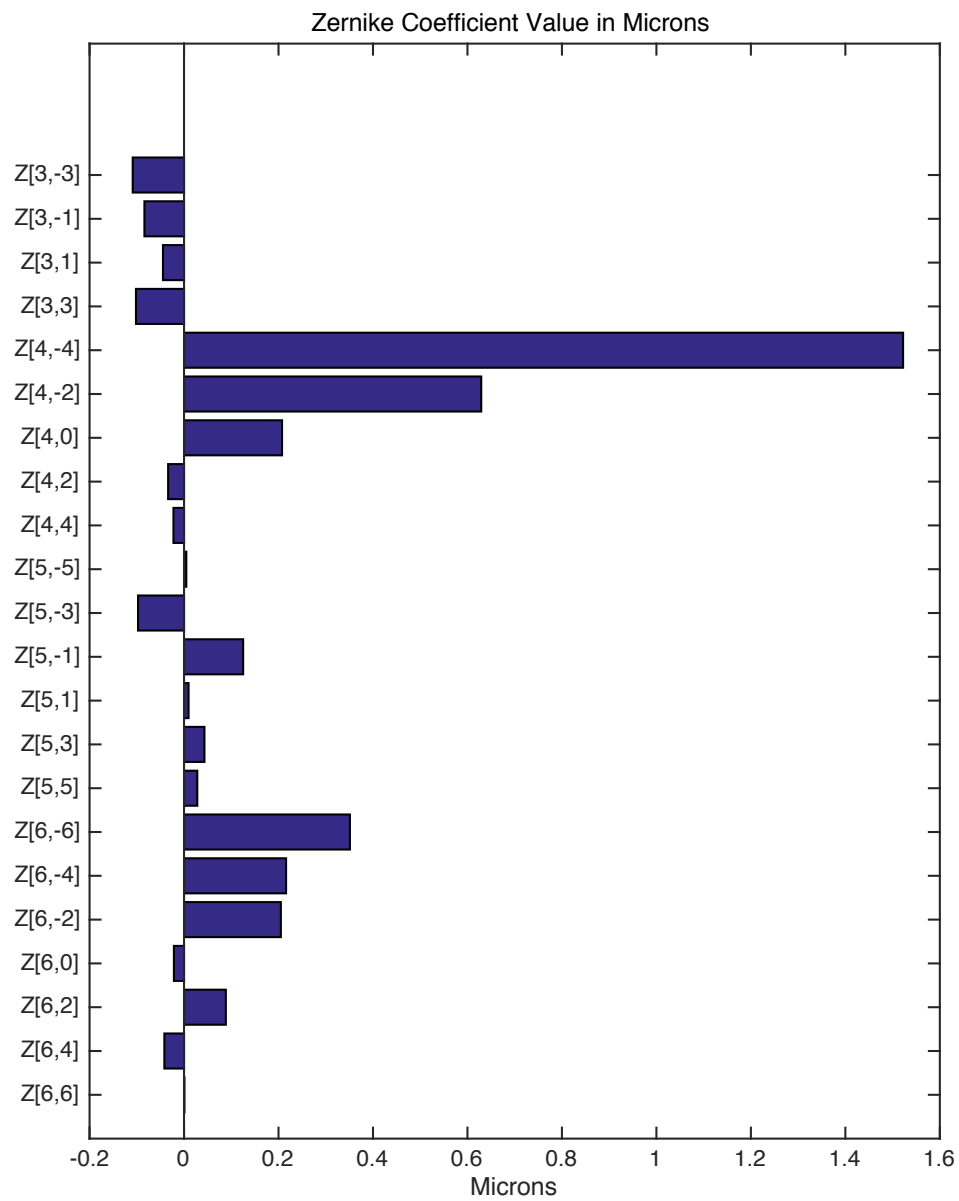


Figure 4.19 Zernike coefficients starting from Z [3, -3] for the f=18mm glass lens.

#### 4.4.2 Glass Lens, $f=30\text{mm}$

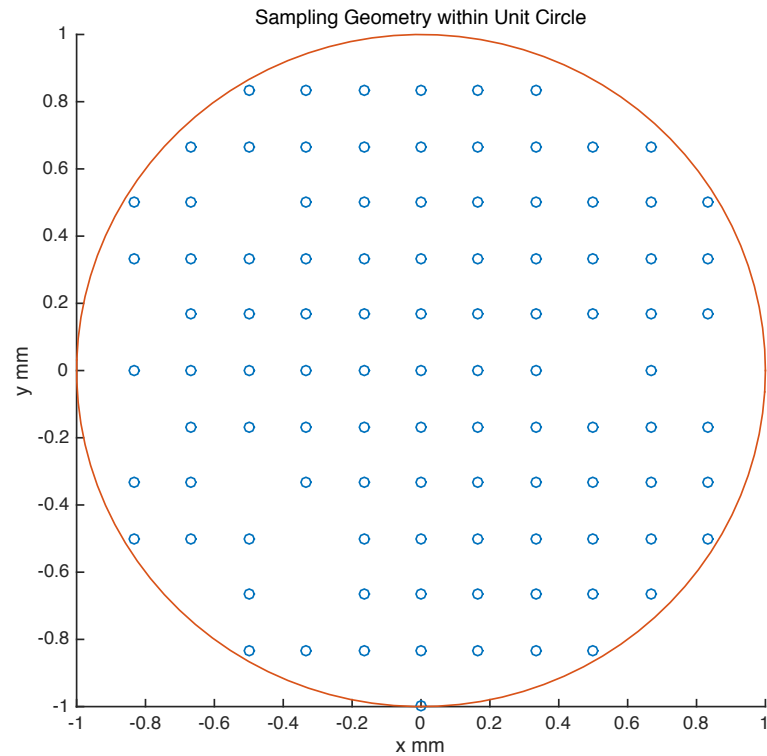


Figure 4.20 Sample geometry. The sample matrix was 13 rows by 13 columns. The matrix was scaled from the 3mm radius to the unit radius.

A 12.5 mm diameter Plano-convex glass lens with a focal length of 30 mm (Edmund Scientific) was used in this experiment. The experimental method was same as for the lens shown in section 4.4.1. Figure 4.20 shows the scaled 100 sampling points used in this experiment. The following figures show the results of this glass lens experiment.

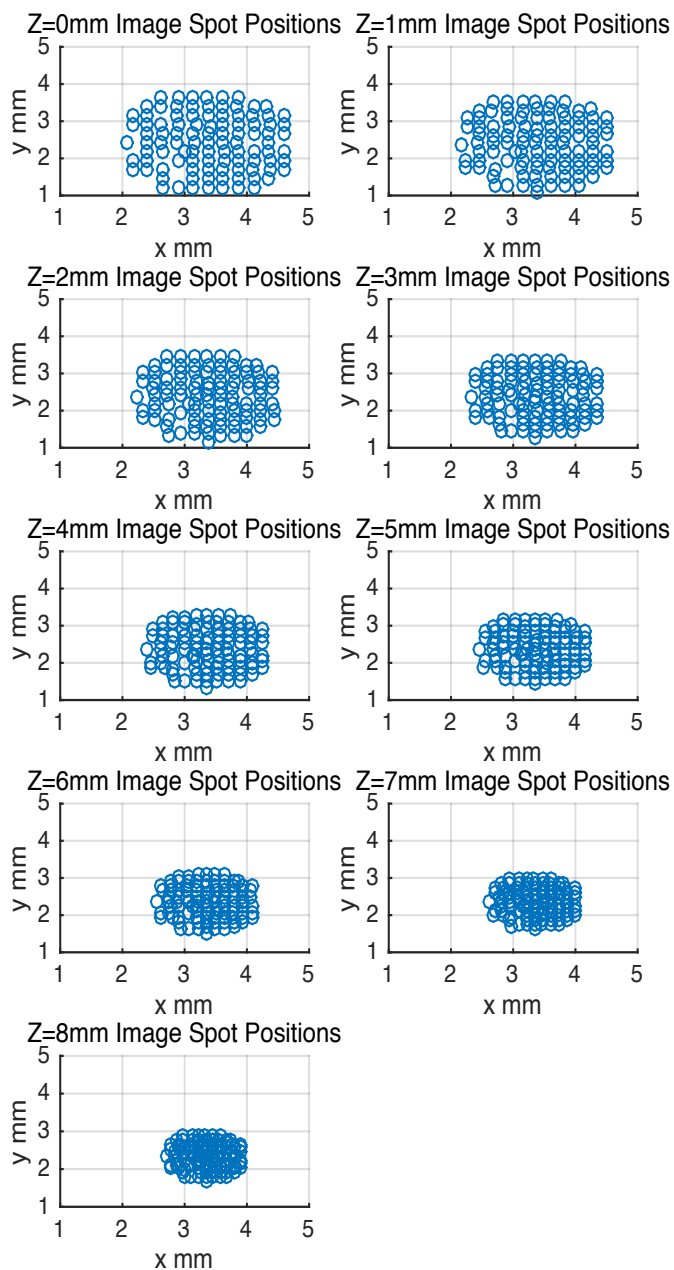


Figure 4.21 Camera recorded spots positions from  $z=1\text{mm}$  to  $z=8\text{mm}$ . The sample matrix was 13 rows by 13 columns.

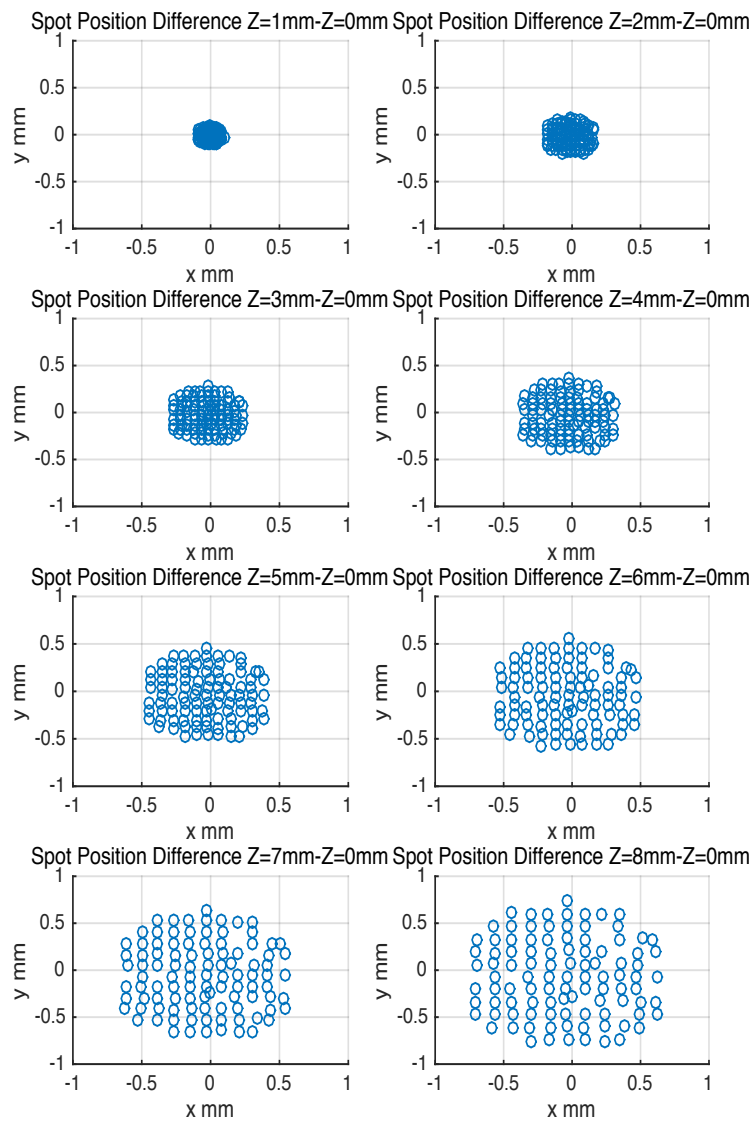


Figure 4.22 Camera recorded spots position differences along the z axis.

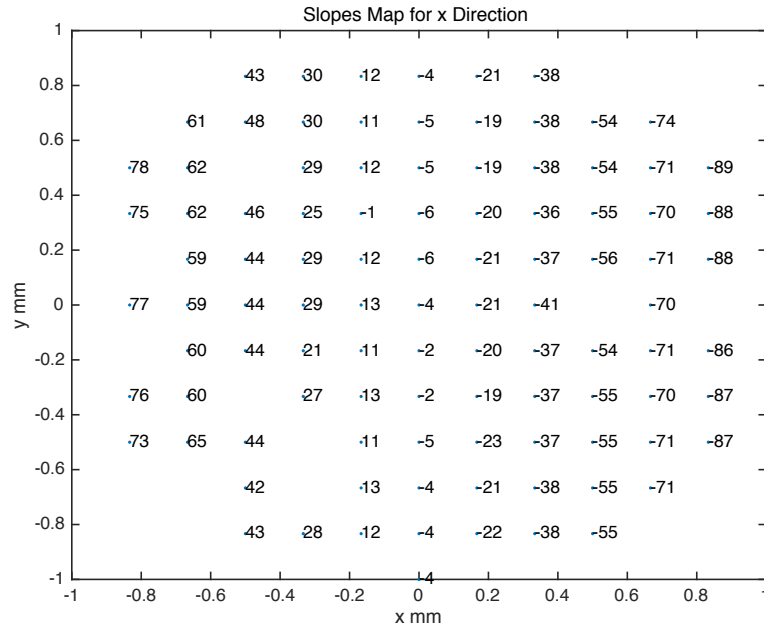


Figure 4.23 Output slope map for x direction. The calculated slope values were multiplied by 1000 on the map for easy reading purpose. The location of the labeled slope outputs corresponds to the location of laser beams in 13 rows by 13 columns sample geometry.

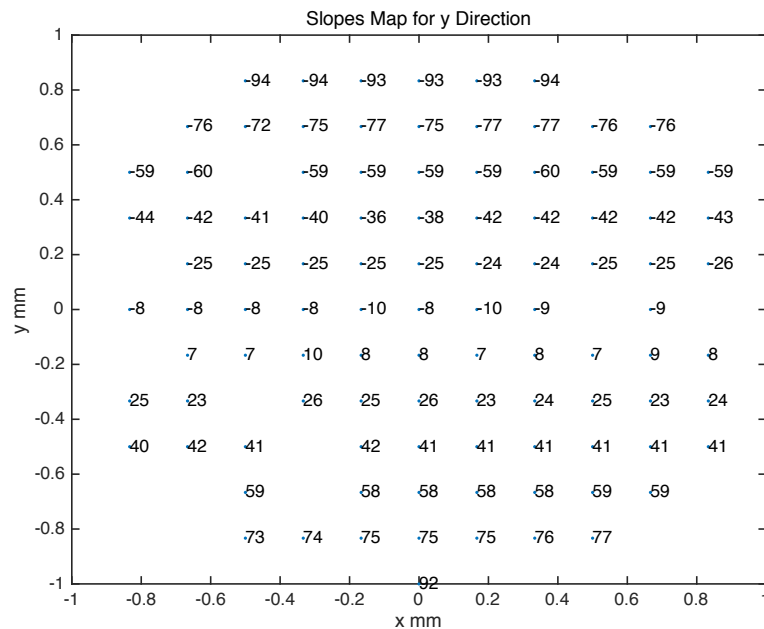


Figure 4.24 Output slope map for y direction. The calculated slope values were multiplied by 1000 on the map for easy reading purpose. The location of the labeled slope outputs corresponds to the location of laser beams in 13 rows by 13 columns sample geometry.

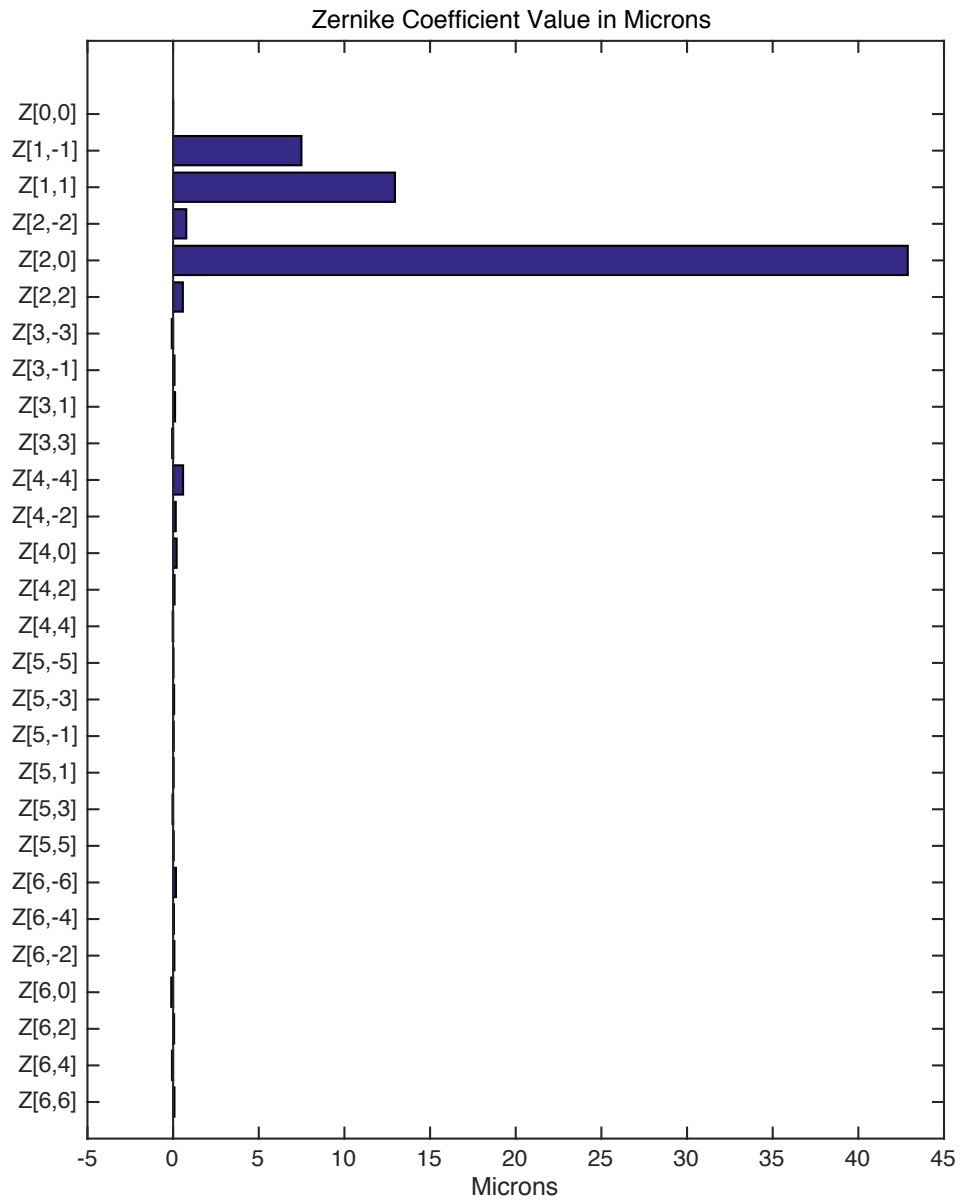


Figure 4.25 Zernike coefficients for the  $f=30$  mm glass lens. The sample geometry was 13 rows by 13 columns over a 6 mm diameter zone.

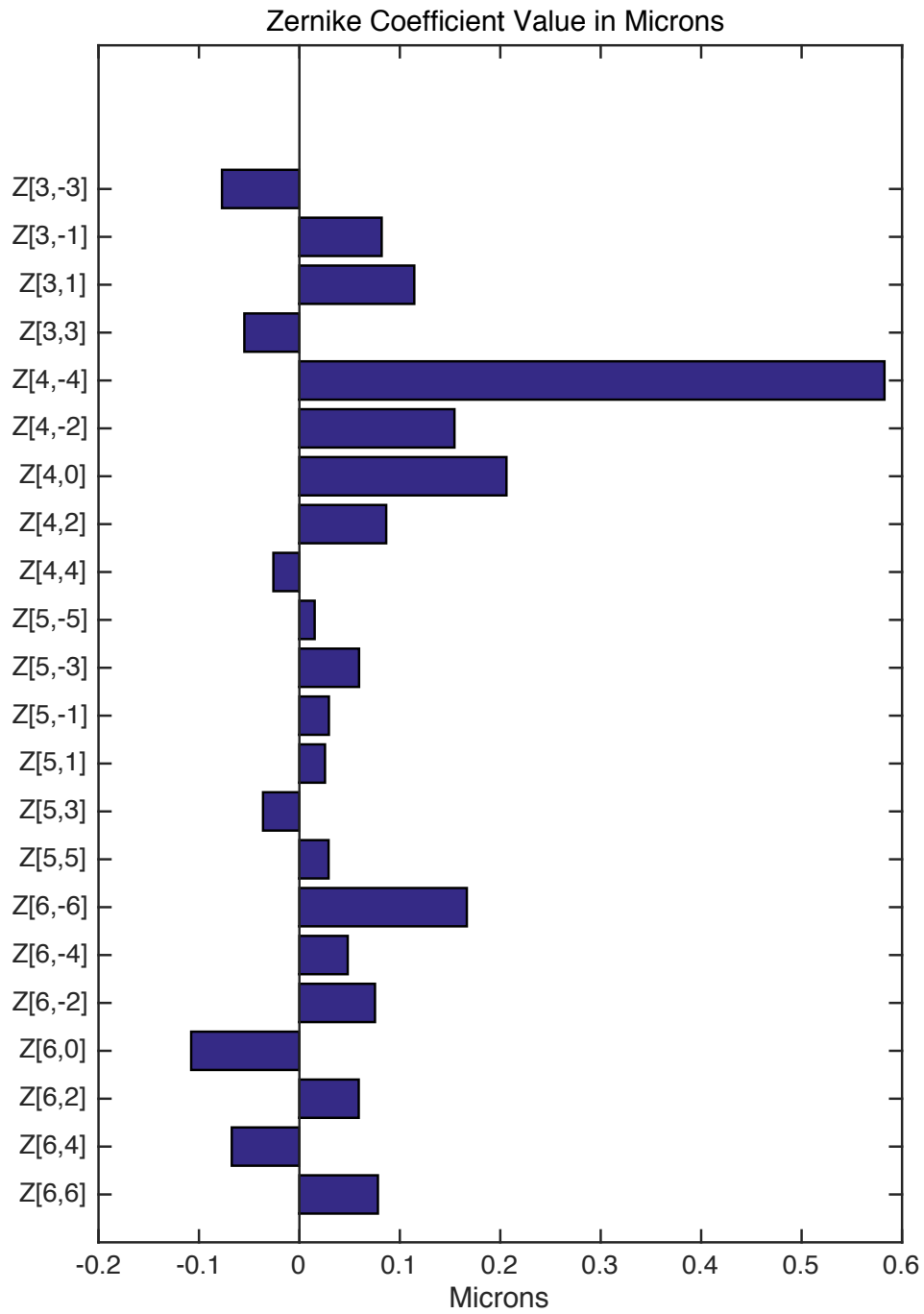


Figure 4.26 Zernike coefficients starting from Z [3, -3] for the f=30mm glass lens.

#### 4.4.3 Cynomolgus Monkey Lens 1 (4C105-OS)

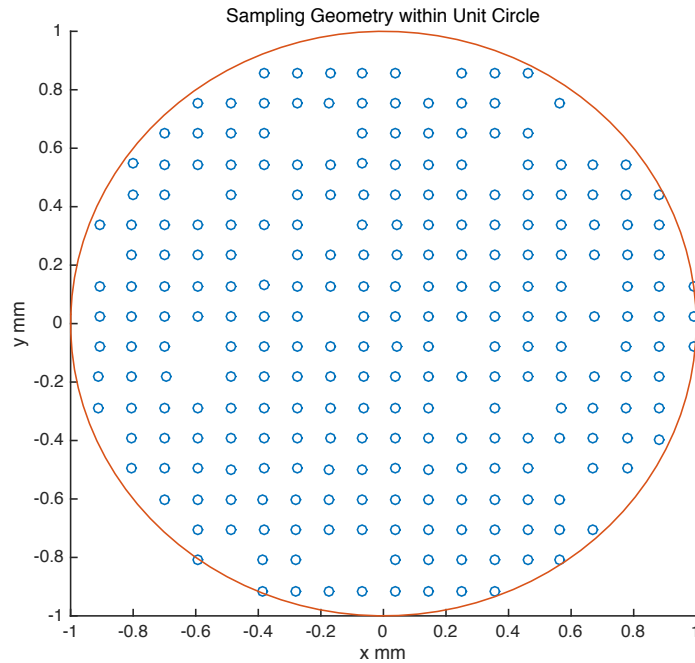


Figure 4.27 Sample geometry. The sample matrix was 19 rows by 19 columns. The matrix was scaled from the 2mm radius to the unit radius.

A cynomolgus lens was placed in the motorized mini stretcher in the LRT system. The lens stretcher stretches the lens radially outward in a step-wise fashion with 0.25mm increment up to 5.25mm. The tissue was immersed in a chamber filled with BSS. Under the 5.25mm stretched condition, the LRT system was programmed to deliver laser rays sequentially to form a sampling matrix with 23 rows by 27 columns over 6mm pupil diameter with 0.21mm increment. The wavefront reconstruction was performed over the centered 4 mm diameter zone, corresponding to a sampling geometry with 19 rows by 19 columns. The camera recorded the images at 8 axial positions from  $z=1\text{mm}$  to  $z=8\text{mm}$  directly below the tissue chamber. The missing points in Figure 4.27 represent the location of



the rays where the spot images were of insufficient quality to allow calculation of the slope.

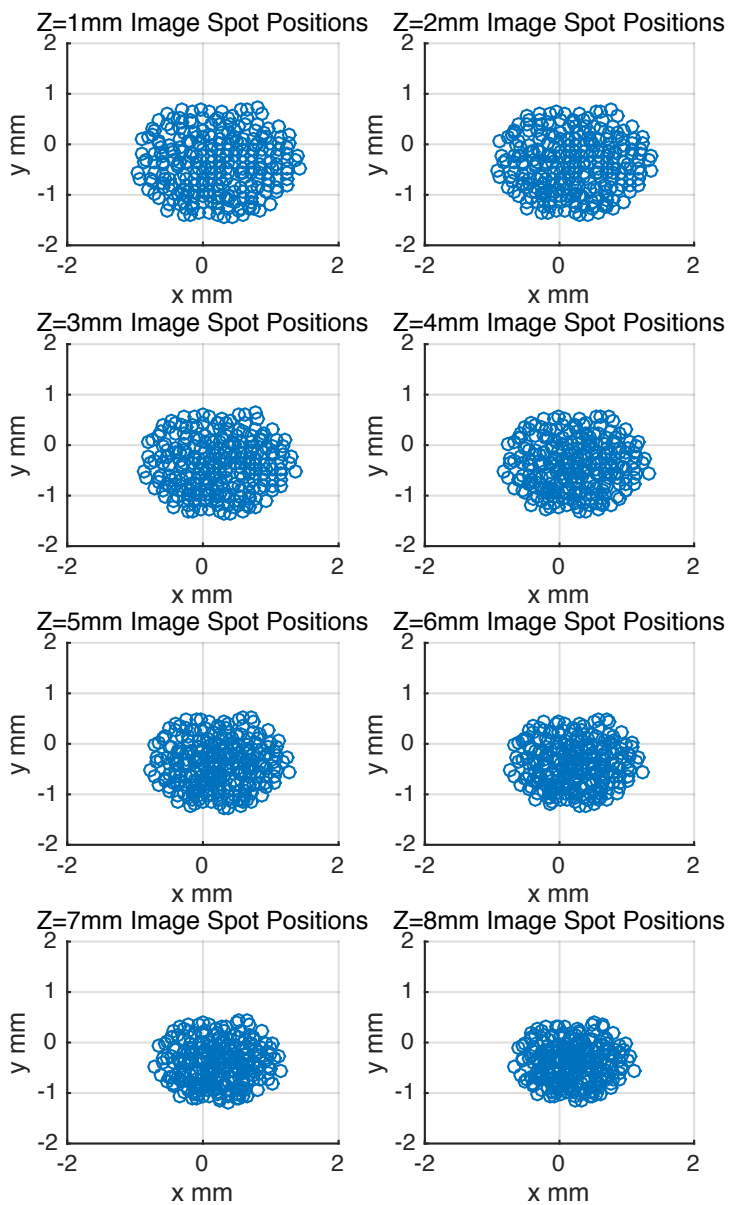


Figure 4.28 Centered camera recorded spots positions for input rays within a circular aperture of 4mm from  $z=1\text{mm}$  to  $z=8\text{mm}$ . The sample matrix was 19 rows by 19 columns.

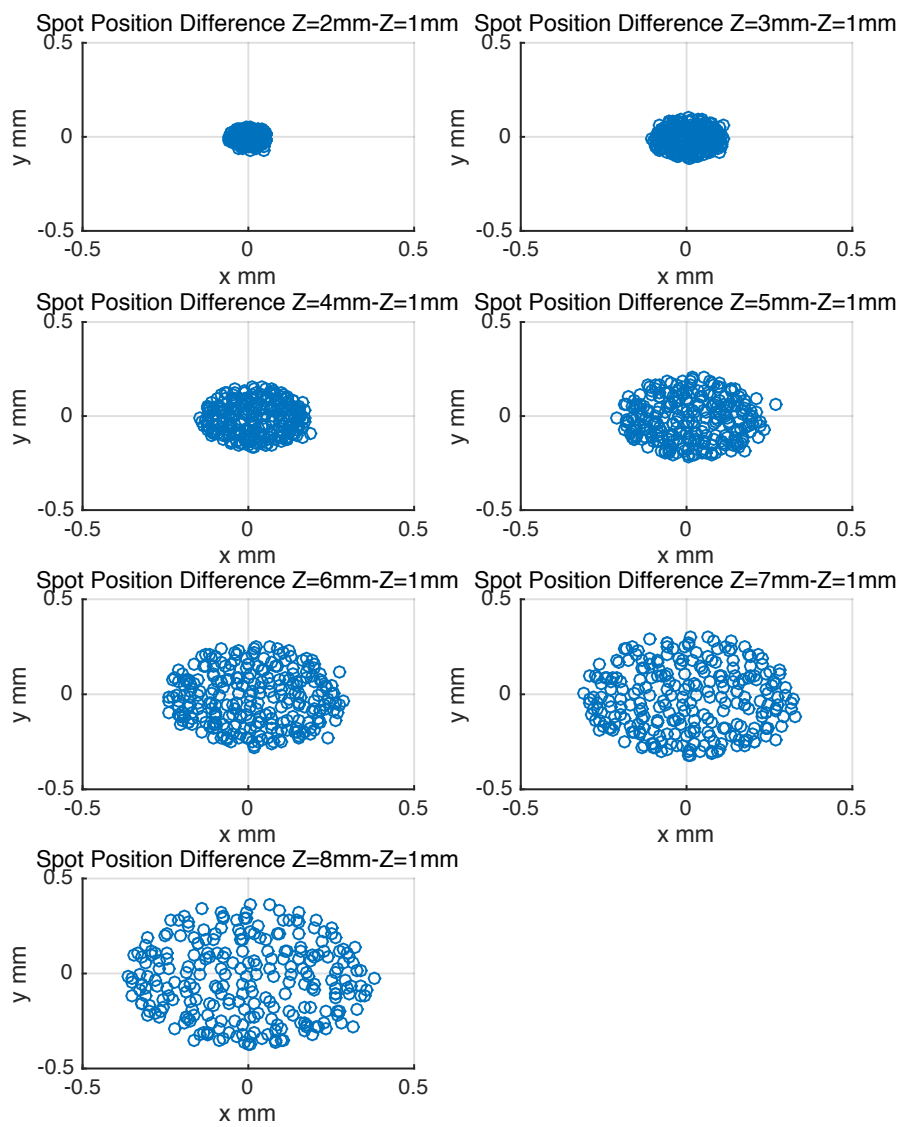


Figure 4.29 Centered camera recorded spots position differences along the z axis.

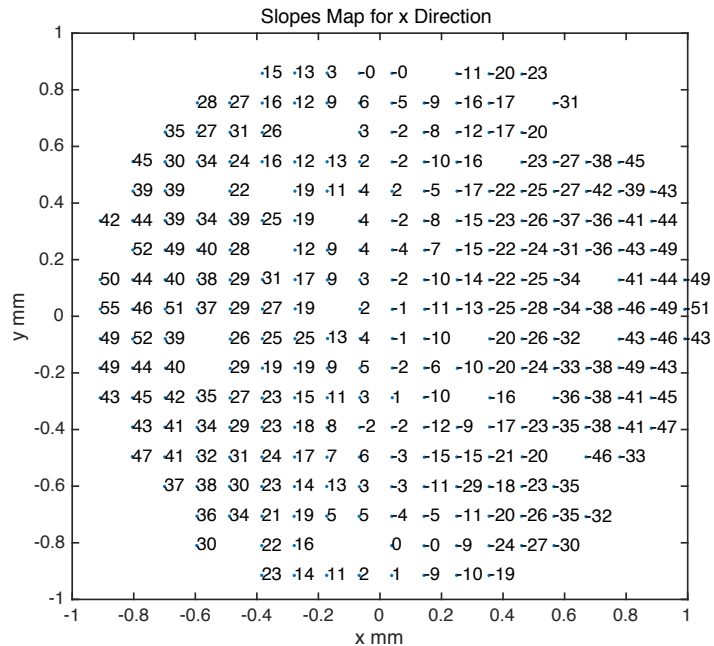


Figure 4.30 Output slope map for x direction. The calculated slope values were multiplied by 1000 on the map for easy reading purpose. The location of the labeled slope outputs corresponds to the location of laser beams in 19 rows by 19 columns sample geometry.

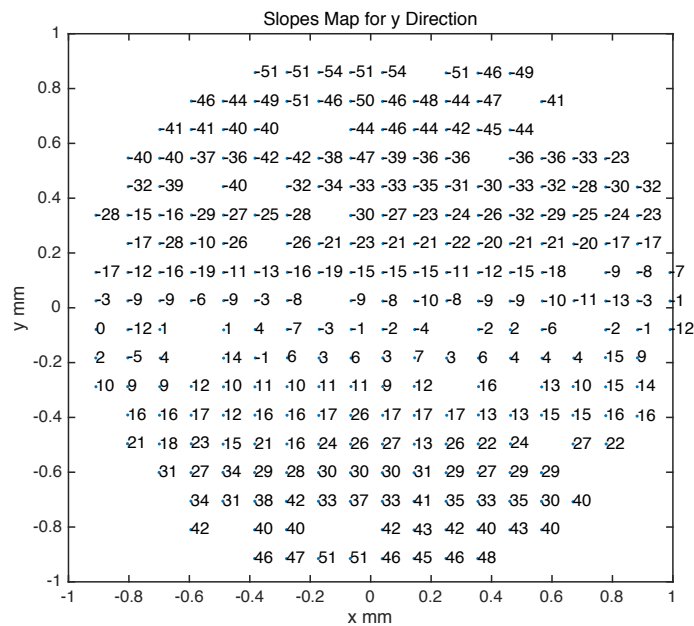


Figure 4.31 Output slope map for y direction. The calculated slope values were multiplied by 1000 on the map for easy reading purpose. The location of the labeled slope outputs corresponds to the location of laser beams in 19 rows by 19 columns sample geometry.

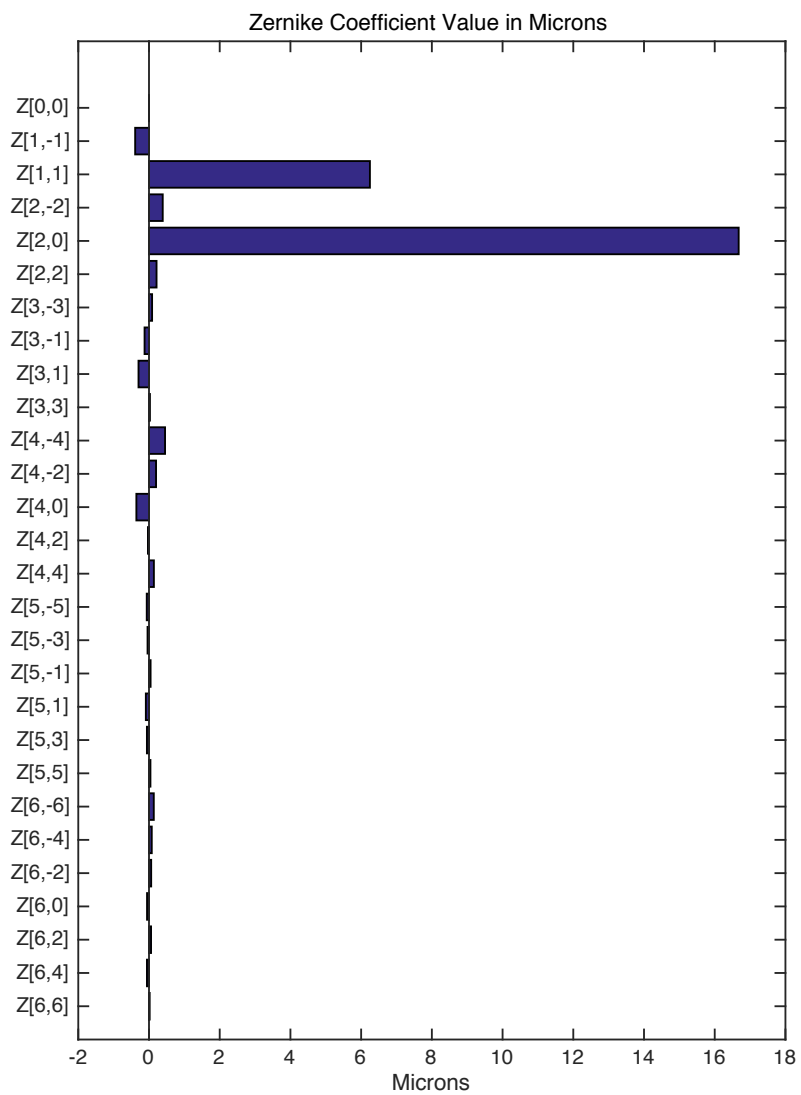


Figure 4.32 Zernike coefficients for Cynomolgus lens 4C105 OS in the stretched state. The sample geometry was 19 rows by 19 columns over a 4mm diameter zone.

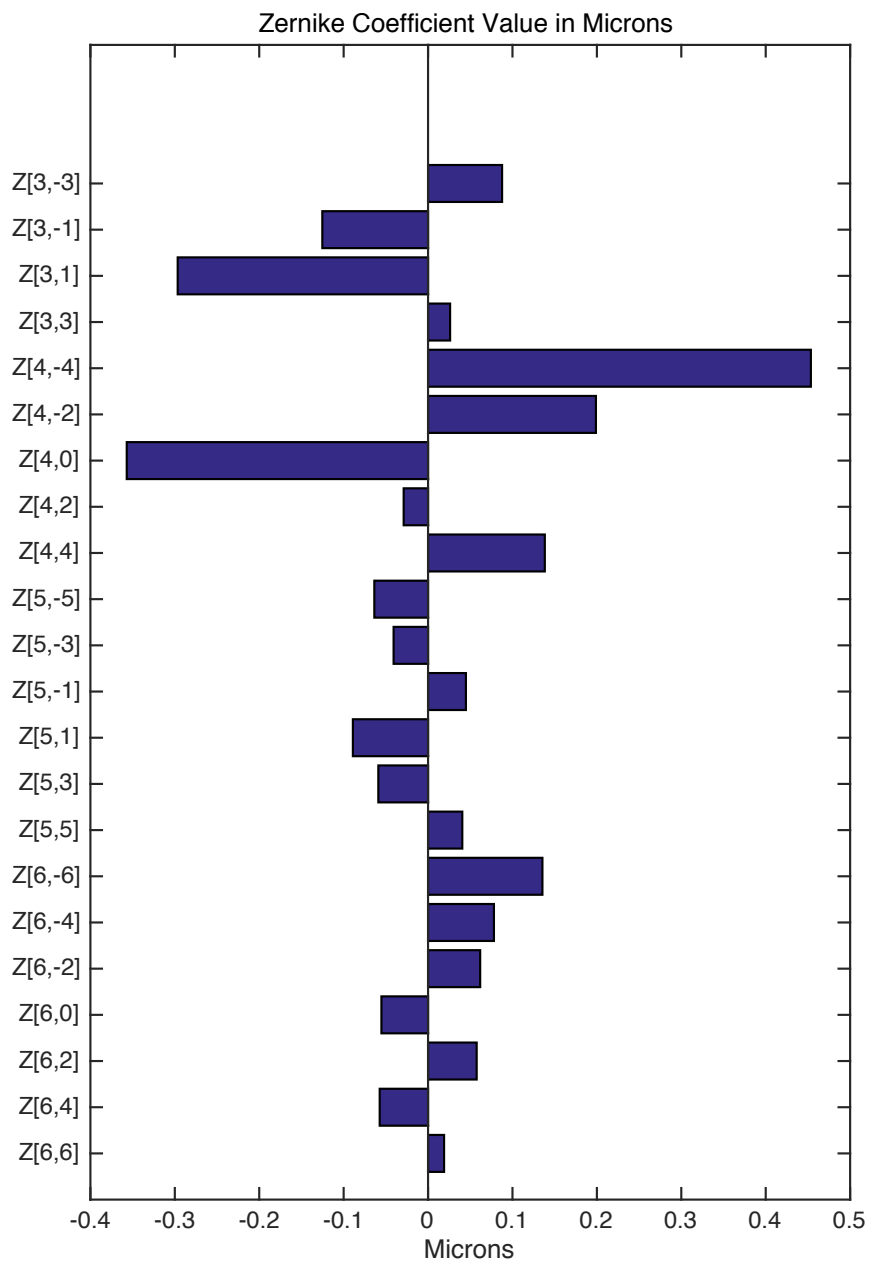


Figure 4.33 Zernike coefficients starting from Z [3, -3] for Cynomolgus lens 4C105 OS in the stretched state.

#### 4.4.4 Cynomolgus Lens 2 (1632 OS)

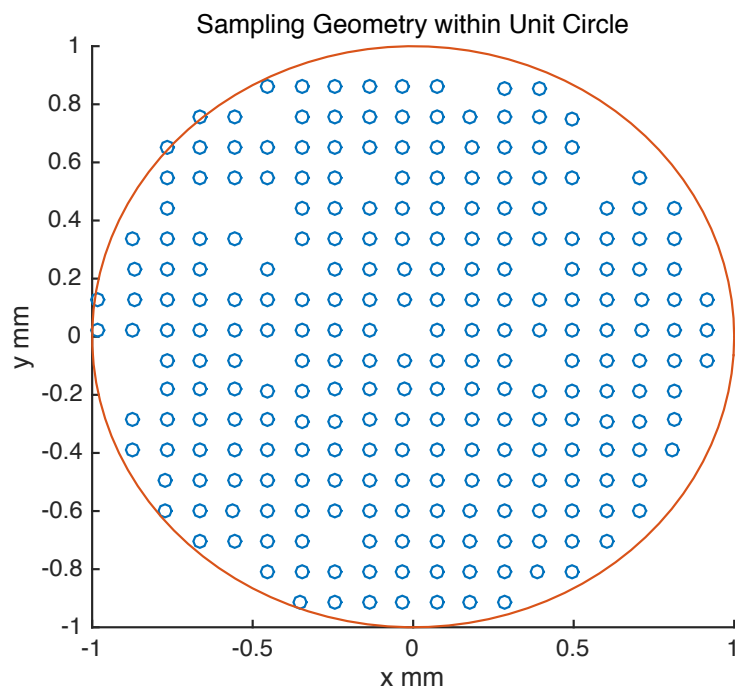


Figure 4.34 Sample geometry. The sample matrix was 19 rows by 19 columns. The matrix was scaled from the 2mm radius to the unit radius .

The experimental method is same as for the cynomolgus lens shown in section 4.4.3. The missing sampling points represent the locations where the ray slopes could not be calculated due to poor spots quality.

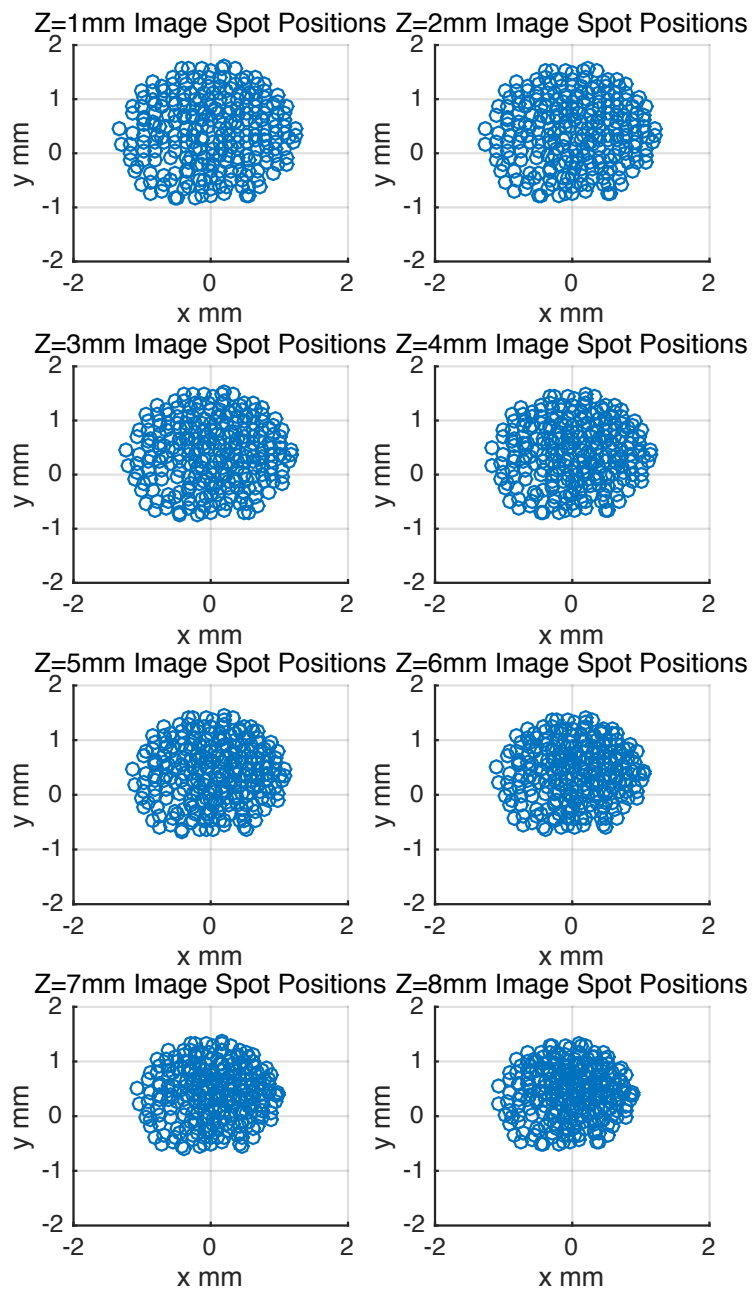


Figure 4.35 Centered camera recorded spots positions for input rays within a circle of 4mm diameter from  $z=1\text{mm}$  to  $z=8\text{mm}$ . The sample matrix was 19 rows by 19 columns.

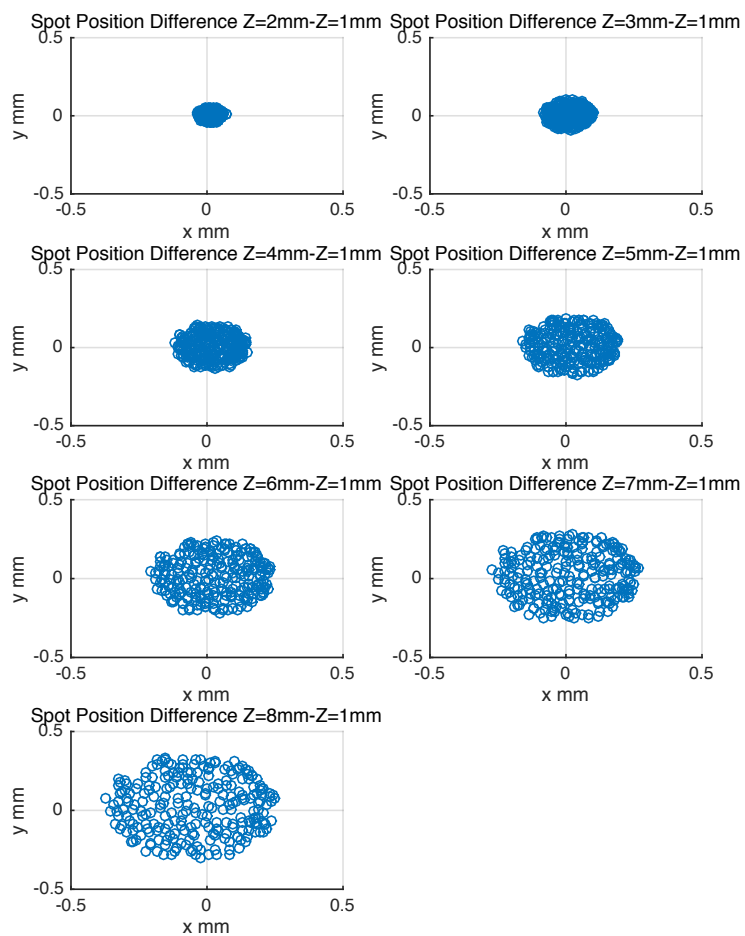


Figure 4.36 Centered camera spots position differences along the z axis.



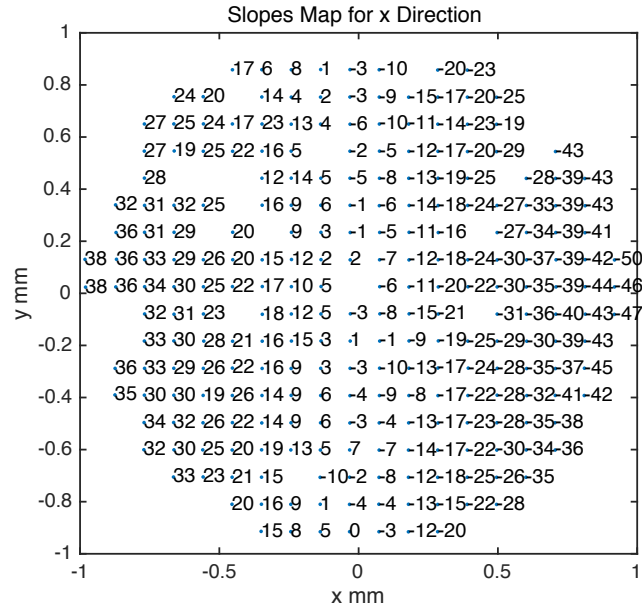


Figure 4.37 Output slope map for x direction. The calculated slope values were multiplied by 1000 on the map for easy reading purpose. The location of the labeled slope outputs corresponds to the location of the input laser beams in 19 rows by 19 columns sample geometry.

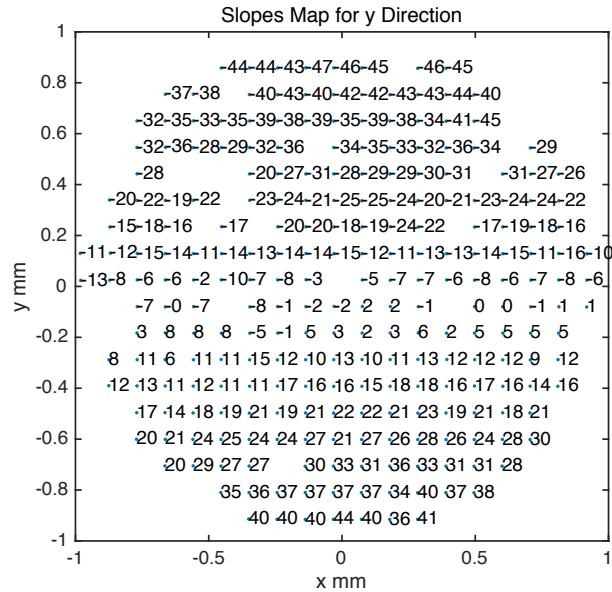


Figure 4.38 Output slope map for y direction. The calculated slope values were multiplied by 1000 on the map for easy reading purpose. The location of the labeled slope outputs corresponds to the location of the input laser beams in 19 rows by 19 columns sample geometry.

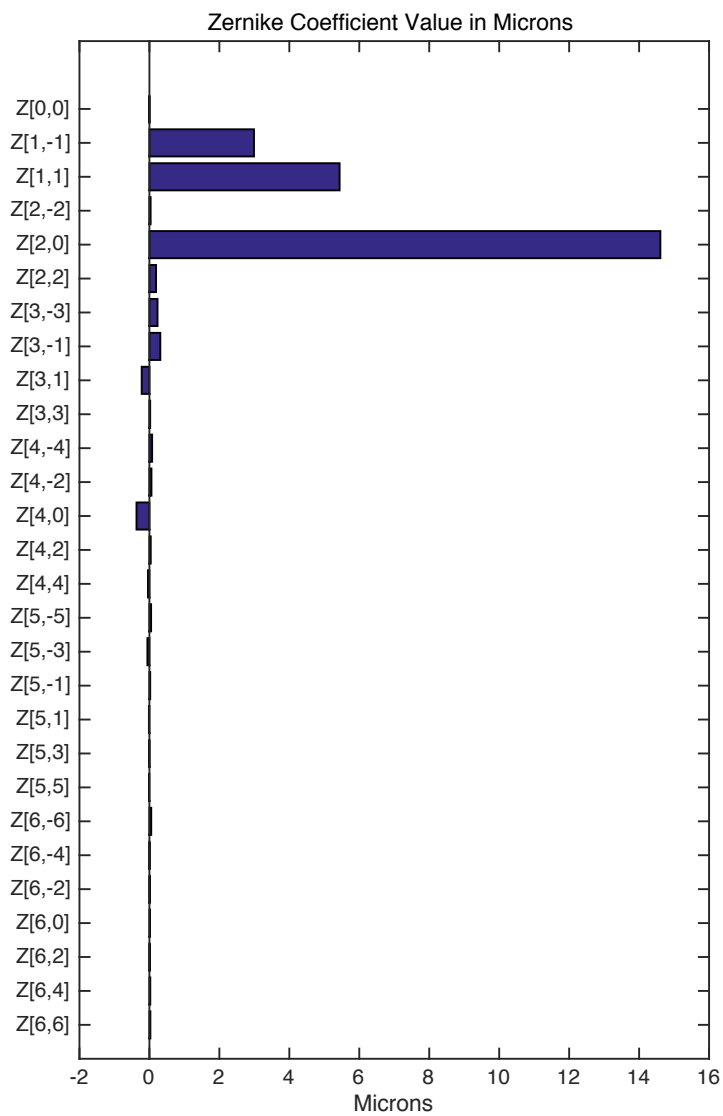


Figure 4.39 Zernike coefficients for Cynomolgus lens 1632 OS. The sample geometry is 19 rows by 19 columns over a 4 mm diameter zone in the stretched state.

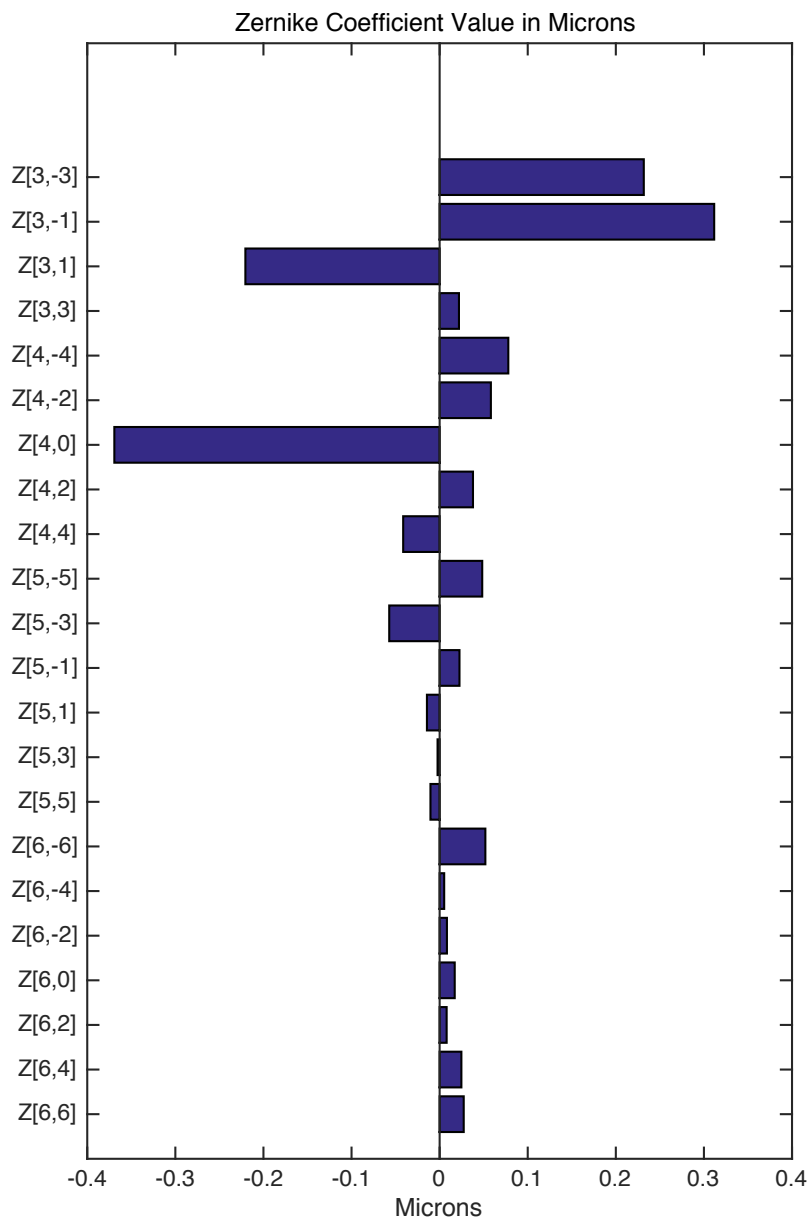


Figure 4.40 Zernike coefficients starting from Z [3, -3] for Cynomolgus lens 1632 OS in the stretched state.

#### 4.4.5 Human Eye Bank Lens #1

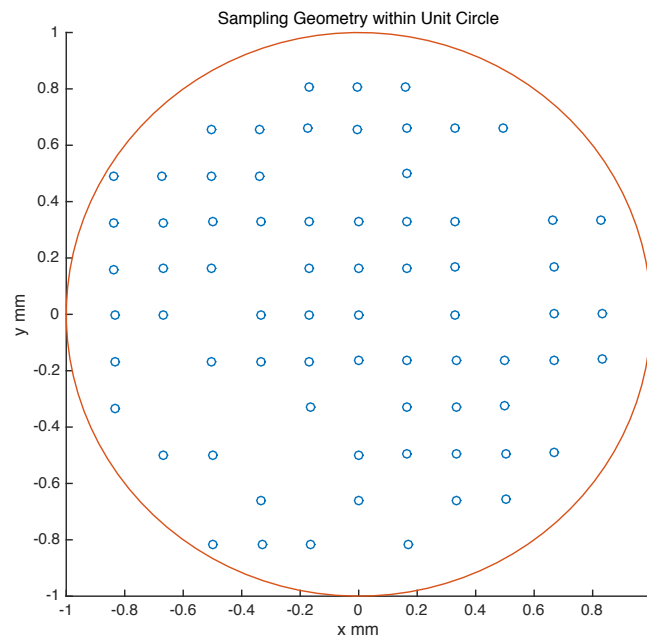


Figure 4.41 Sample geometry. The sample matrix was 13 rows by 13 columns. The matrix was scaled from the 3mm radius to the unit radius.

An experiment was performed on a lens from a human eye donated from the Florida Lion's Eye Bank (16-04-014OS). The lens was placed in an O-ring inside the tissue chamber of the LRT system. The experimental method is same as for the Cynomolgus lens shown in section 4.4.3. The LRT system recorded 169 images to form a 13 rows by 13 columns matrix with a 0.5mm increment over a 6mm pupil diameter. As shown in Figure 4.41, the slopes could not be calculated in several locations due to the poor spots quality caused by a cataract. Slopes could only be calculated at 73 sampling points. The results of this experiment and the calculated Zernike coefficients are shown in following figures.

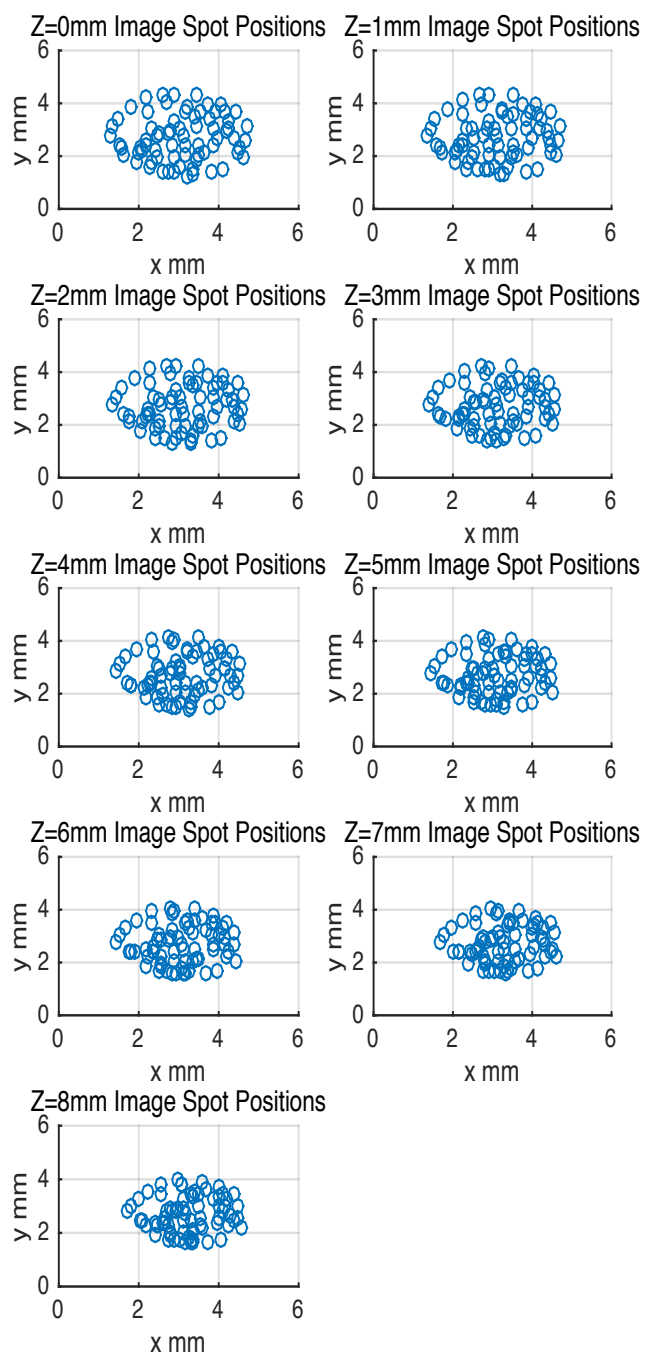


Figure 4.42 Camera recorded spots positions from  $z=1\text{mm}$  to  $z=8\text{mm}$ . The sample matrix was 13 rows by 13 columns over a 6mm diameter zone.

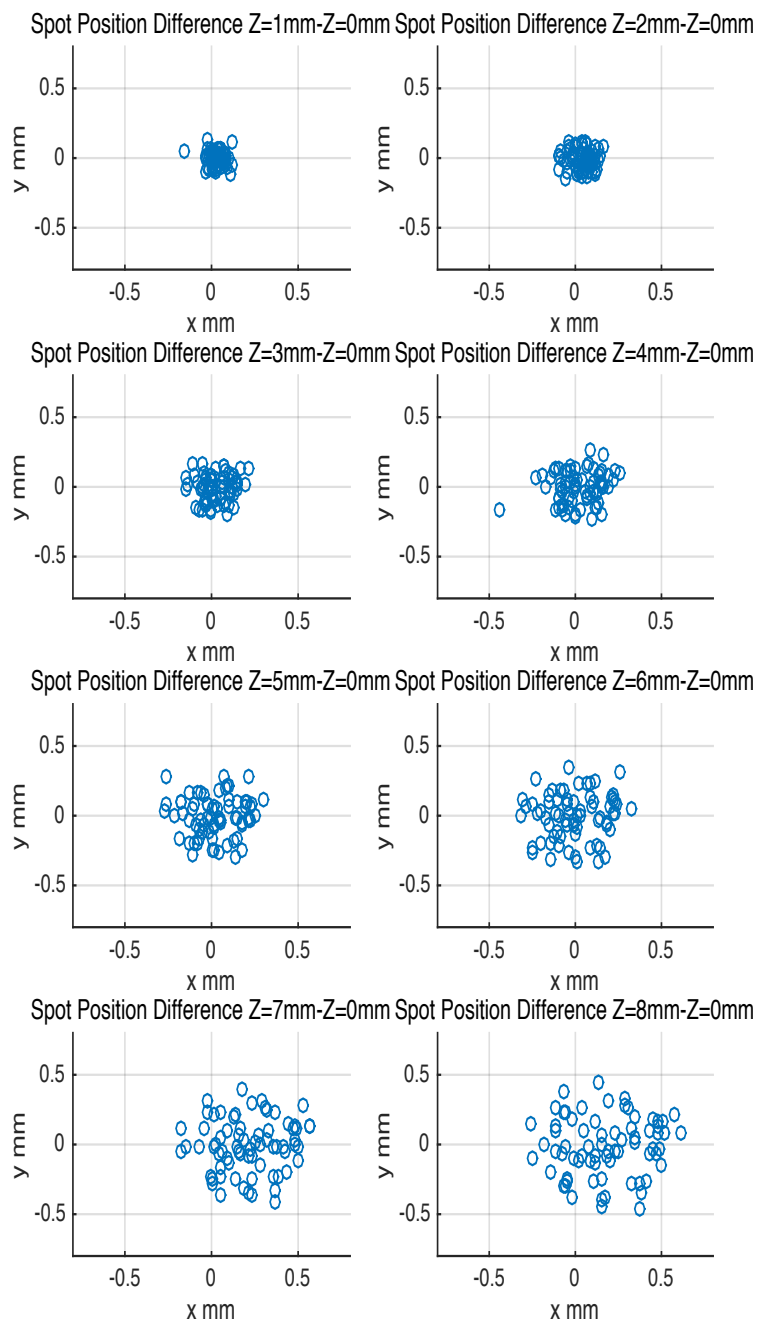


Figure 4.43 Camera recorded spots position differences along the z axis.

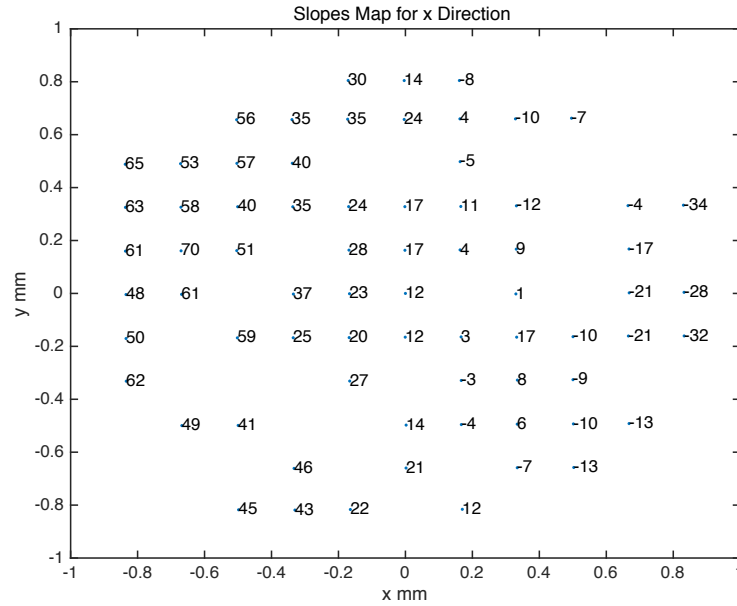


Figure 4.44 Output slope map for x direction. The calculated slope values were multiplied by 1000 on the map for easy reading purpose. The location of the labeled slope outputs corresponds to the location of the input laser beams in 13 rows by 13 columns sample geometry.

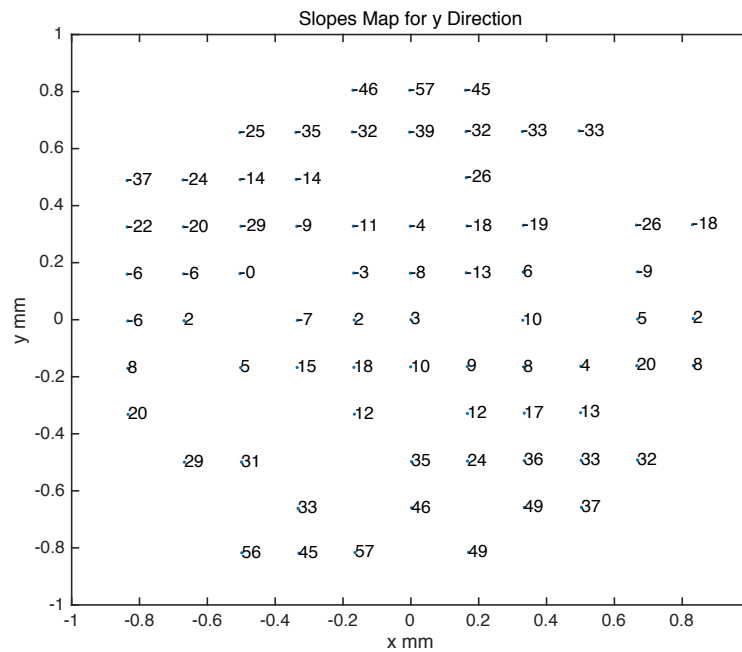


Figure 4.45 Output slope map for y direction. The calculated slope values were multiplied by 1000 on the map for easy reading purpose. The location of the labeled slope outputs corresponds to the location of the input laser beams in 13 rows by 13 columns sample geometry.

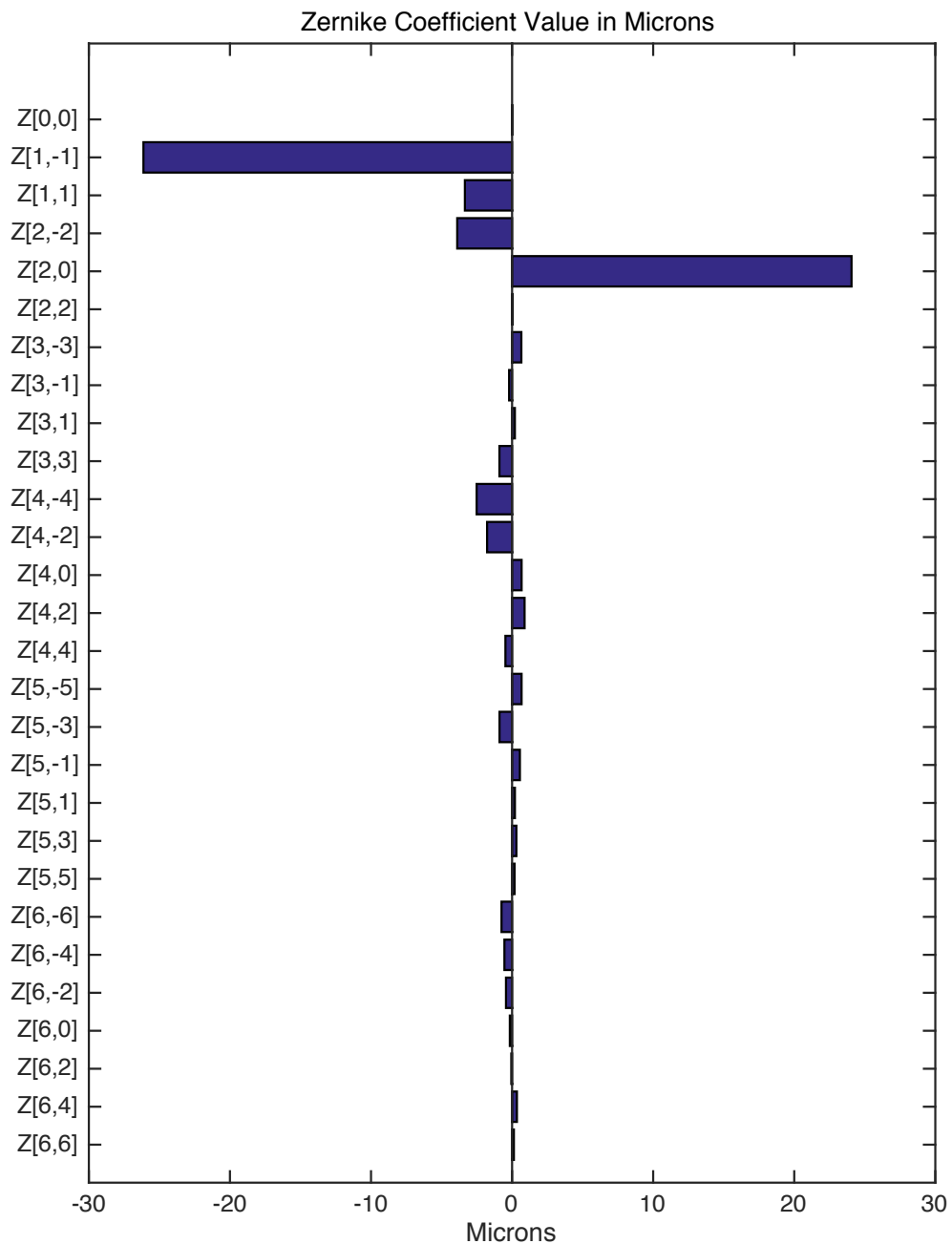


Figure 4.46 Zernike coefficients for human lens # 16-04-014 OS. The sample geometry was 13 rows by 13 columns over a 6mm diameter zone.



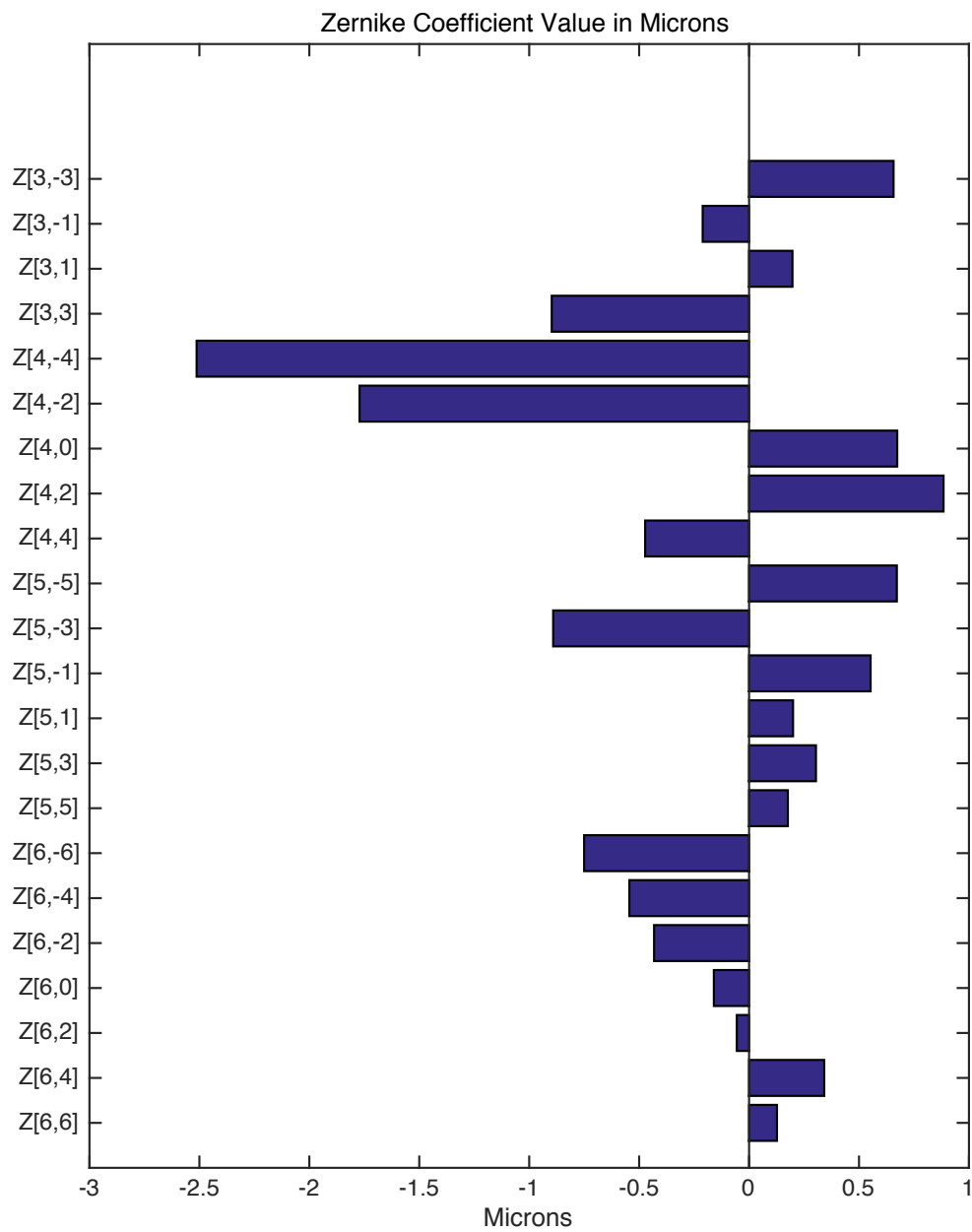


Figure 4.47 Zernike coefficients starting from Z [3, -3] for human lens # 16-04-014 OS.

#### 4.4.6 Human Eye Bank Lens #2

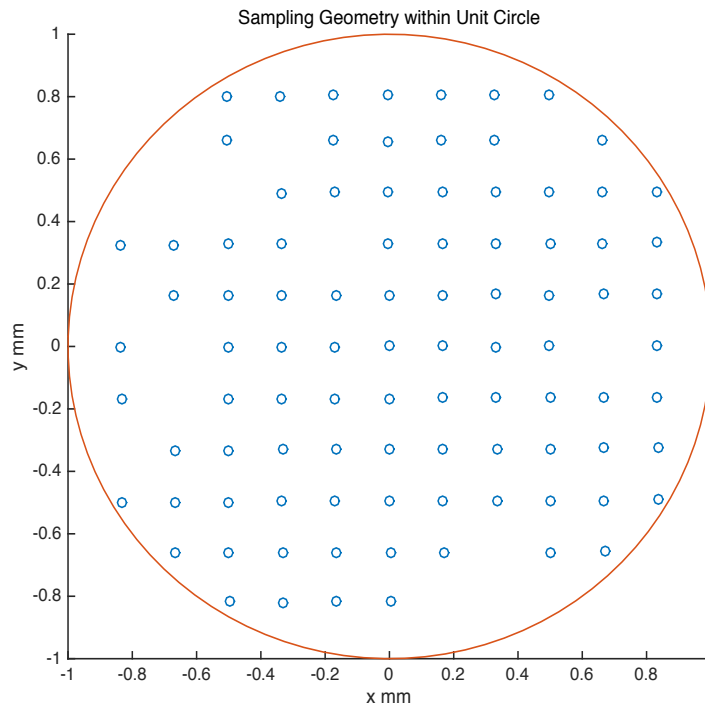


Figure 4.48 Sample geometry. The sample matrix was 13 rows by 13 columns. The matrix was scaled from the 3mm radius to the unit radius.

An experiment was performed on a second human lens donated by the Florida Lion's Eye Bank (16-04-014 OD). The experimental method is same as for the human lens shown in section 4.4.5. A total of 169 images were recorded by the LRT system to form a 13 rows by 13 columns matrix at each axial camera position. This experiment used 93 sampling points within the unit circle to reconstruct the Zernike coefficients. The remaining slopes could not be calculated due to the poor spots quality caused by the presence of a cataract. The missing points in Figure 4.48 show the location of the input rays corresponding to the missing slope values. The flowing figures show the results of this human lens experiment.

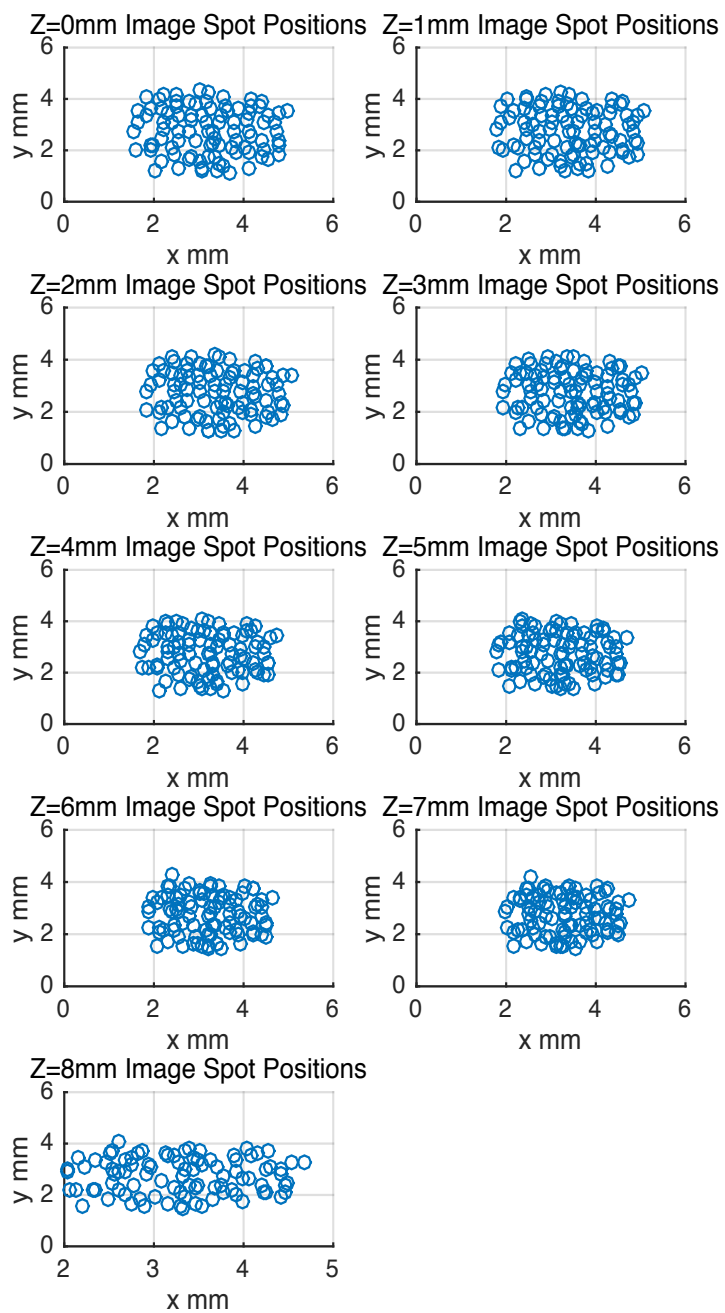


Figure 4.49 Camera recorded spots positions from  $z=1\text{ mm}$  to  $z=8\text{ mm}$ . The sample matrix was 13 rows by 13 columns over a 6mm diameter zone.

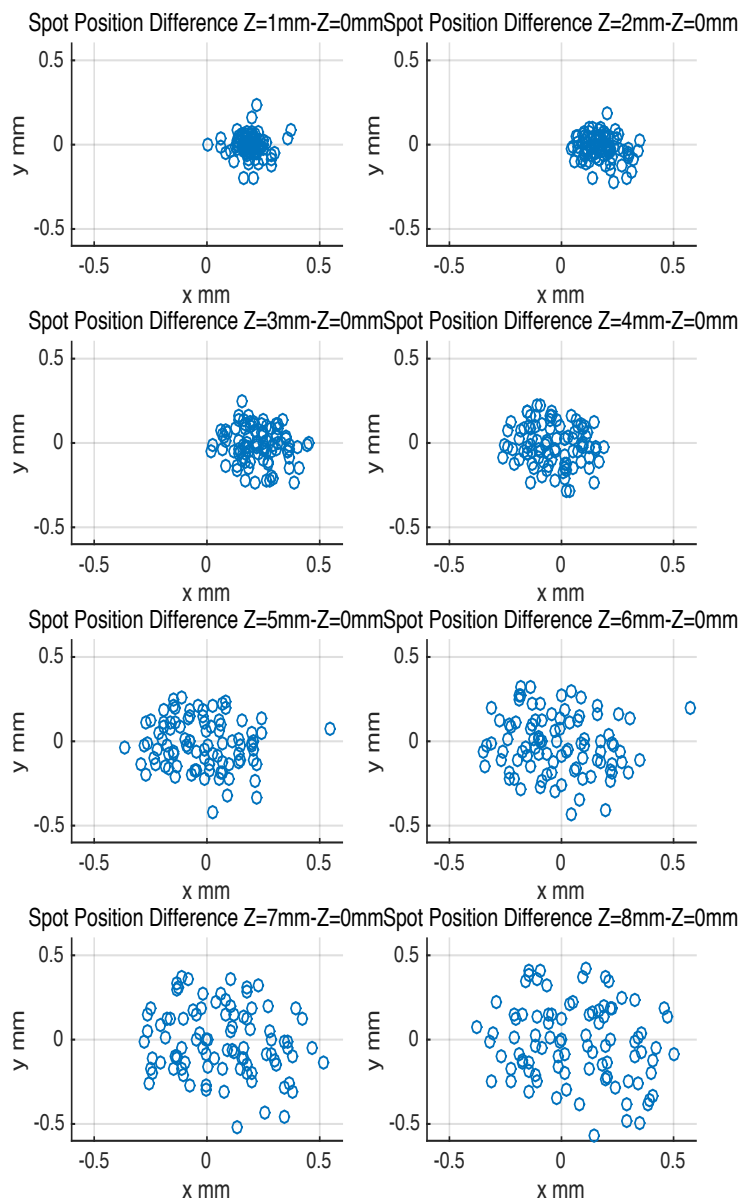


Figure 4.50 Camera recorded spots position differences along the z axis.

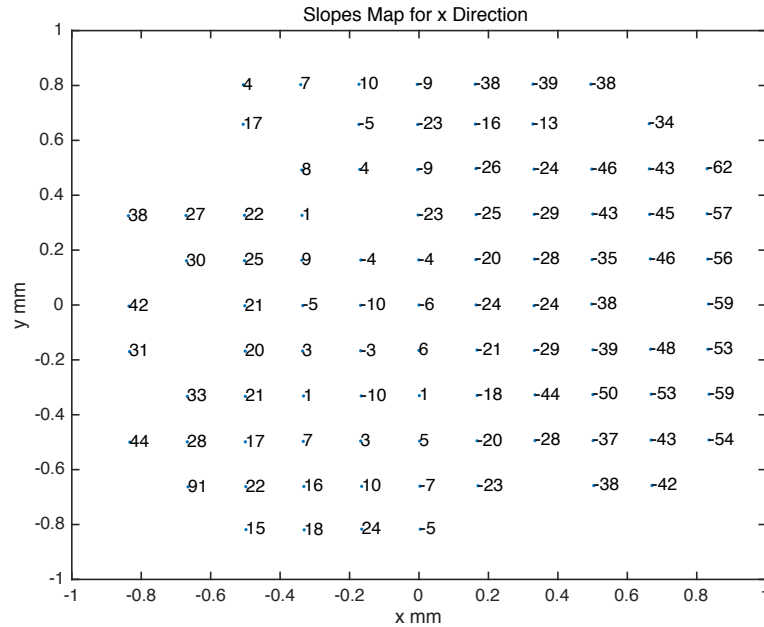


Figure 4.51 Output slope map for x direction. The calculated slope values were multiplied by 1000 on the map for easy reading purpose. The location of the labeled slope outputs corresponds to the location of the input laser beams in a 13 rows by 13 columns sample geometry.

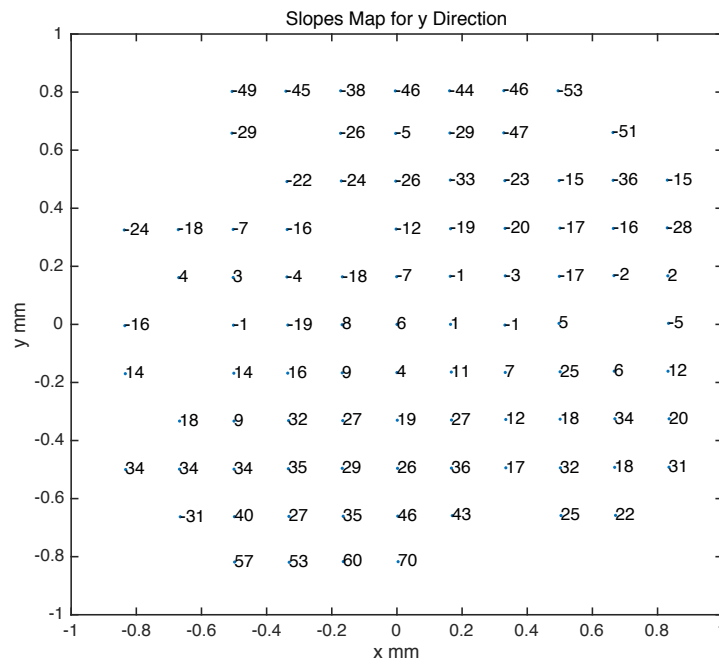


Figure 4.52 Output slope map for y direction. The calculated slope values were multiplied by 1000 on the map for easy reading purpose. The location of the labeled slope outputs corresponds to the location of the input laser beams in a 13 rows by 13 columns sample geometry.

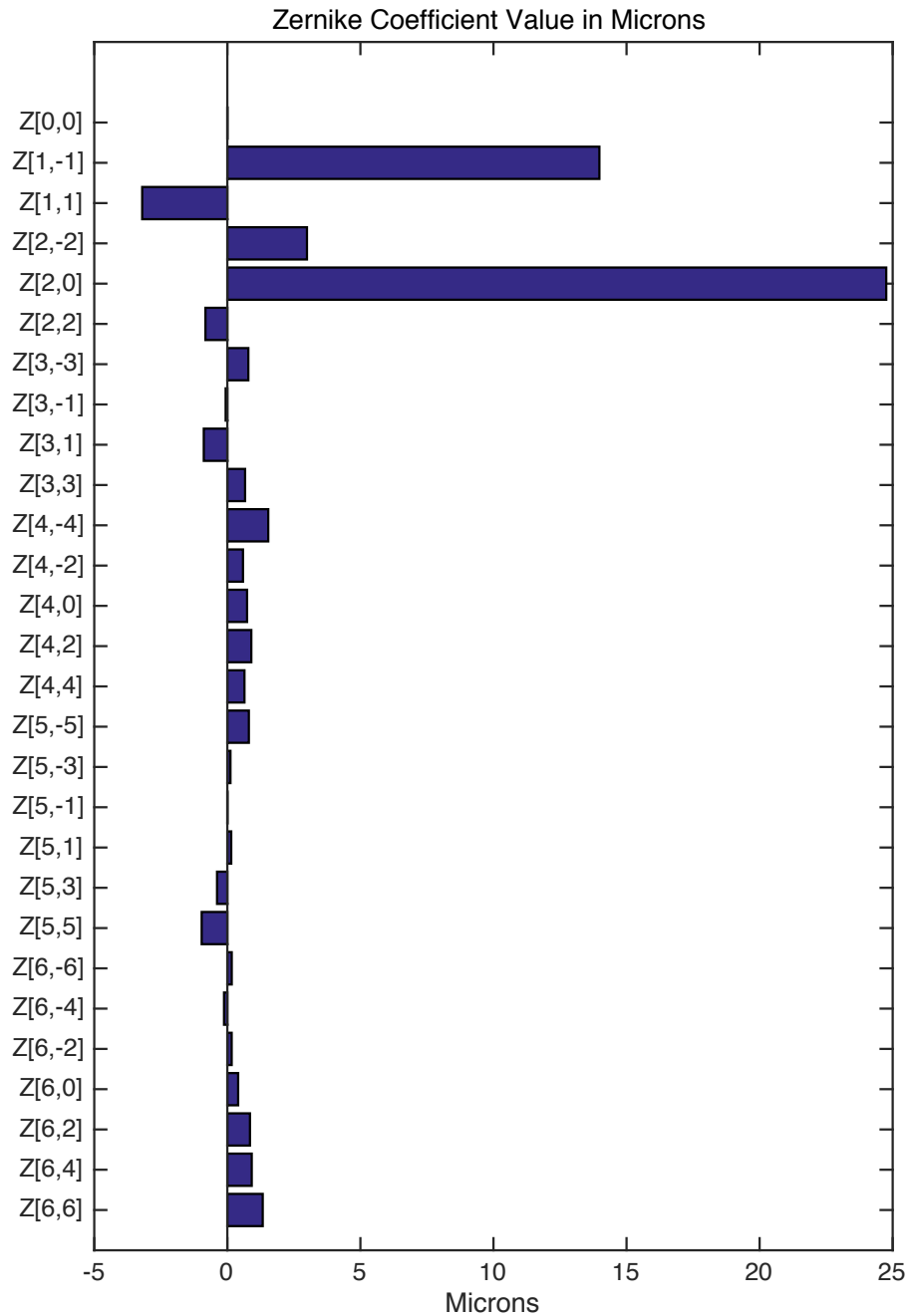


Figure 4.53 Zernike coefficients for human lens # 16-04-014 OD. The sample geometry was 13 rows by 13 columns over a 6mm diameter zone.

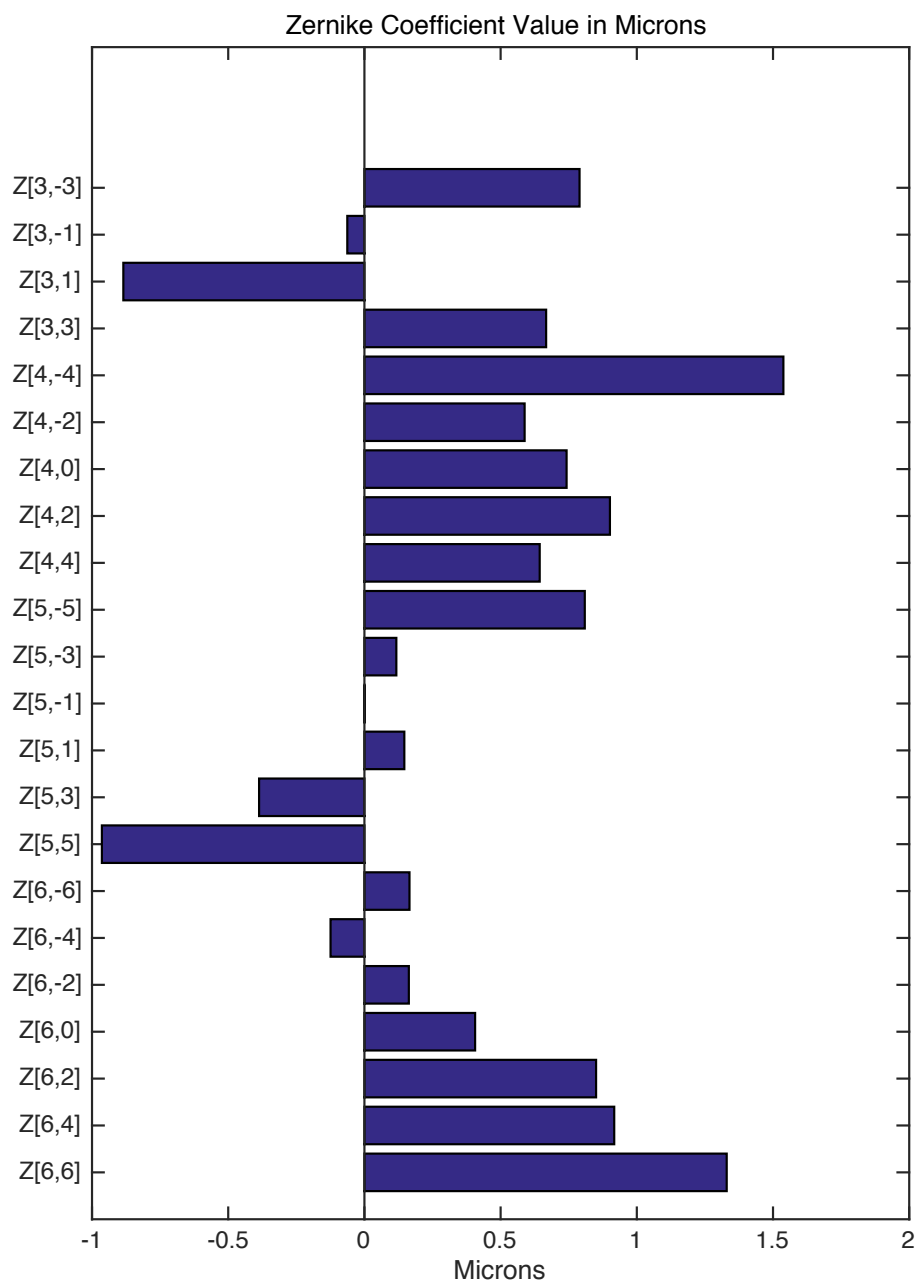


Figure 4.54 Zernike coefficients starting from Z[-3,3] for human lens # 16-04-014 OD.

#### 4.6 Discussion

In order to test the calculated Zernike coefficients from the developed MATLAB program and experiments, expected theoretical  $Z_2^0$  and  $Z_4^0$  values were calculated to compare with the experimental results. According to Table 3.1, the contribution of Zernike coefficients  $Z_2^0$  to the Zernike wavefront aberration is

$$W(h) = 2\sqrt{3} \cdot Z_2^0 \cdot \left(\frac{h^2}{a^2}\right) \quad (\text{Eq.4.7})$$

where  $W$  is the wavefront aberration ( $\mu\text{m}$ ),  $Z_2^0$  is the Zernike aberration coefficient ( $\mu\text{m}$ ),  $h$  is the input ray height ( $\mu\text{m}$ ), and  $a$  is the pupil radius ( $\mu\text{m}$ ). Figure 4.55 shows the relationship between wavefront aberration  $W$ , input ray height  $h$  and effective focal length  $f$  with the assumption that aberrations other than  $Z_2^0$  were negligible.

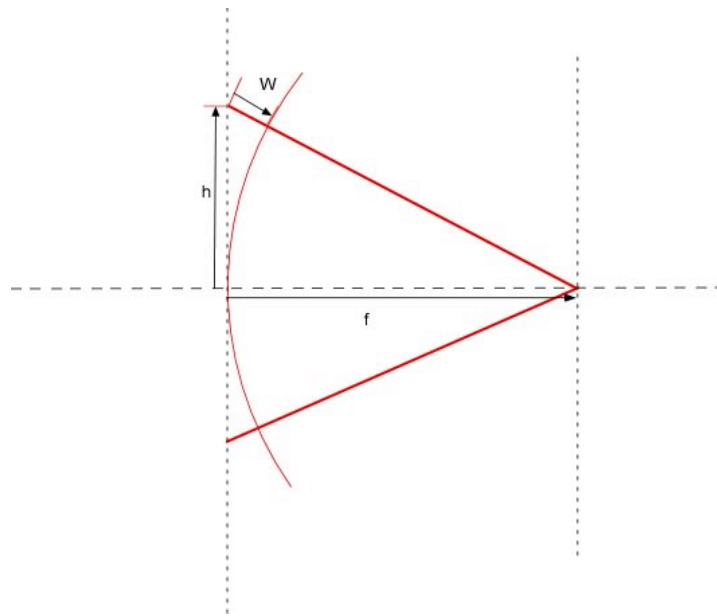


Figure 4.55 The relationship between wavefront aberration  $W$ , input ray height  $h$  and effective focal length  $f$  under the assumption that aberrations other than  $Z_2^0$  were negligible.



As shown in Figure 4.55, if the wavefront is a sphere (defocus only), the relationship between wavefront aberration  $W$ , input ray height  $h$ , and effective focal length  $f$  can be expressed by equation

$$h^2 + f^2 = (f + W)^2 \quad \text{Eq.4.8}$$

The wavefront aberration  $W$  is equal to

$$W = \sqrt{f^2 + h^2} - f \quad \text{Eq.4.9}$$

According to Taylor series expansion,

$$\sqrt{f^2 + h^2} \cong 1 + \frac{h^2}{2 \cdot f^2} \quad \text{Eq.4.10}$$

Equation 4.7 can be simplified into

$$W = \frac{h^2}{2 \cdot f} \quad \text{Eq.4.11}$$

According to Optical Society of America standards for reporting optical aberrations, the wavefront aberration shown in Figure 4.55 is positive. Combining Equations 4.7 and 4.11 shows that the Zernike coefficient  $Z_2^0$  is equal to

$$Z_2^0 = \frac{a^2}{4 \cdot \sqrt{3} \cdot f} \quad \text{Eq.4.12}$$

Or, in terms of the power  $P_L = \frac{n}{f}$ ,

$$Z_2^0 = \frac{a^2 \cdot P_L}{4 \cdot \sqrt{3} \cdot n} \quad \text{Eq.4.13}$$

where the refractive index  $n = 1.341$  when the lens is placed in Balanced Salt Solution (Maceo et al., 2015).

To validate the glass lenses experiments, the measured Zernike coefficients  $Z_2^0$  was input into equation Eq.4.12 to calculate the focal length and the results were compared with the original known focal length.

In order to validate the cynomolgus lenses and human lenses experiments, the measured Zernike coefficients  $Z_2^0$  were used to calculate the lens powers. The calculated effective lens powers were compared with published values. The tables listed below show the comparison between the MATLAB results and published values for glass lenses, cynomolgus lenses, and human lenses.

<b>Glass Lens</b>	<b>Calculated <math>Z_2^0</math> 6mm Pupil Size (<math>\mu\text{m}</math>)</b>	<b>Calculated Focal Length (mm)</b>
f=18mm	71.60	18.14
f=30mm	42.88	30.29

Table 4.1 Comparison between calculated focal length and expected focal length

<b>Cynomolgus Lens</b>	<b>Calculated <math>Z_2^0</math> 4mm Pupil Size (<math>\mu\text{m}</math>)</b>	<b>Calculated Effective Lens Power (D)</b>	<b>Published Mean Effective Lens Power (D)</b> (Maceo et al., 2015)
Cyno 4C105 OS 5.25 mm Stretched	16.68	38.74	$33.55 \pm 3.41 D$
Cyno 1632 OS 5.25 mm Stretched	14.61	33.93	$33.55 \pm 3.41 D$

Table 4.2 Comparison between calculated effective lens power values and published effective lens power values for cynomolgus lenses. For cynomolgus lenses, the Zernike coefficients are reconstructed over a 4mm pupil diameter.

<b>Human Lens</b>	<b>Calculated <math>Z_2^0</math> 6mm Pupil Size (<math>\mu\text{m}</math>)</b>	<b>Calculated Effective Lens Power (D)</b>	<b>Published Mean Effective Lens Power (D)</b> (Hernandez et al., 2015)
FLEB 16-04-014 OS	24.0609	24.83	24.34
FLEB 16-04-014 OD	24.7582	25.56	24.34

Table 4.3 Comparison between calculated effective lens power values and published effective lens power values for human lenses. For human lenses, the Zernike coefficients are reconstructed over a 6mm pupil diameter.

As shown in the tables above, for glass lenses, the calculated focal length is very close to the original known focal length, which indicates the calculated Zernike coefficients  $Z_2^0$  are accurate. For both cynomolgus lenses and human lenses, the calculated powers are within the range of the published values. These results show the feasibility of using the MATLAB program to calculate the defocus coefficients  $Z_2^0$ .

The results of the spherical aberration  $Z_4^0$  coefficients are also within the range of expected values. The Zernike coefficients for stretched cynomolgus crystalline lenses over a 6mm pupil diameter are expected to be  $-2.57 \pm 0.52 \mu\text{m}$  on average (Maceo et al., 2015). As shown in Table 4.4, the measured results are within the range of expected values.

<b>Cynomolgus Lens</b>	<b>Calculated <math>Z_4^0</math> 4mm Pupil Size (<math>\mu\text{m}</math>)</b>	<b>Calculated <math>Z_4^0</math> 6mm Pupil Size (<math>\mu\text{m}</math>)</b>	<b>Published <math>Z_4^0</math> Values 6mm Pupil Size (<math>\mu\text{m}</math>)</b> (Maceo et al., 2015)
Cyno 4C105 OS 5.25 mm Stretched	-0.36	-1.81	$-2.57 \pm 0.52$
Cyno 1632 OS 5.25 mm Stretched	-0.37	-1.87	$-2.57 \pm 0.52$

Table 4.4 Comparison of Zernike coefficients  $Z_4^0$  between calculated results and published values for cynomolgus lenses

The source of errors for the calculated Zernike coefficients may come from several factors such as the quality of the LRT acquired images, the alignment of laser rays with the crystalline lenses during experiments, and the sampling geometries used for calculations. As mentioned in the slope calculation section, for some human lenses with cataract, it is challenging to accurately find the centroids of the images. Future work needs to be done to minimize the effects of these sources of errors.

## CHAPTER 5

### SUMMARY AND FUTURE WORK

#### 5.1 Summary

In this thesis project, A MATLAB program was developed to reconstruct the Zernike coefficients from the LRT spot patterns to study the aberrations of the crystalline lens. The developed program was tested on glass lenses, human lenses, and cynomolgus lenses. The results show the feasibility of using LRT spots patterns acquired at different axial positions to calculate Zernike coefficients.

Future studies will focus on correcting for the effects of distortions on the calculated Zernike coefficients of *in vitro* crystalline lens in the LRT system, determining the optimal sampling geometry related to the number of spots and the spots spacing, and studying the optimal number of axial positions that are used for the slope calculations. Future studies will also focus on investigating the accuracy of centroids, further validating the Zernike coefficients, evaluating the effects of input beam geometry, and improving the MATLAB program for easier data input and output.

#### 5.2 Zernike Coefficients Distortion Correction

The effects of distortions of the ray path on the calculated Zernike coefficients need to be corrected. The slopes of the rays are measured in air after transmission through the tissue chamber window. However, in order to represent

the wavefront of the laser rays passing through the crystalline lens in aqueous environments (refer to Figure 4.6 in Chapter 4), the calculated slopes must be corrected to take into account the effects of refraction through the window of the cell. The correction can be performed by using Snell's law to compute the ray slopes inside the cell. The distortion may contribute to some of the difference between measured and predicted Zernike coefficient  $Z_4^0$  as shown Chapter 4.

### 5.3 Effects of the Centroids Position Errors on the Slope Calculation

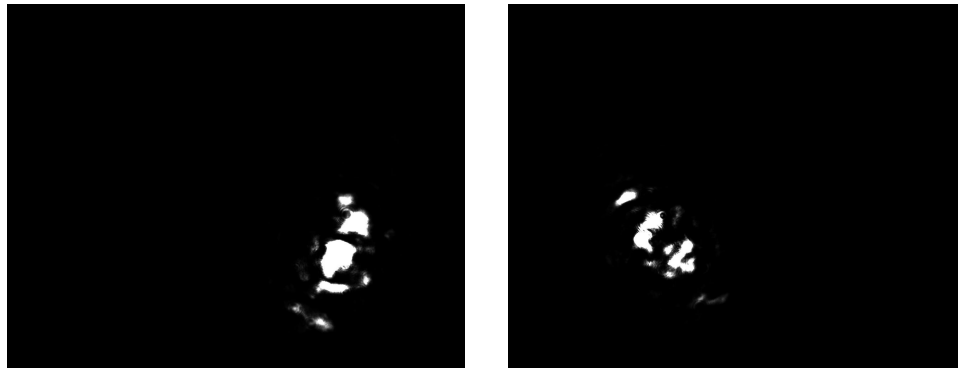


Figure 5.1 Examples of spot images from a human lens with cataract

Currently, a MATLAB program is used to determine the image spot centroids automatically. For some lenses, such as a human lens with cataract, the acquired image may form a spot that has no clear shape. Therefore, validations of the current MATLAB program need to be done to test the accuracy of the resulted spot centroids, and the effects of centroids position errors on the calculated slopes.

## 5.4 Evaluate Effects of Input Beam Geometry

An empty cell LRT experiment was performed to evaluate if the entrance beam is truly parallel, with zero slope, over the entire measurement zone. In the experiment, no lens is present in the tissue chamber. The entrance laser rays passing through the tissue chamber and the spot images are recorded at 8 axial positions by the camera. The recorded spot centroids indicate that the entrance rays have some small slopes, particularly for the  $y$  direction, and these slopes may affect the calculated Zernike coefficients. Future studies will focus on understanding the effects of the entrance beam geometry on the calculated Zernike coefficients. The experimental results are shown in following figures.

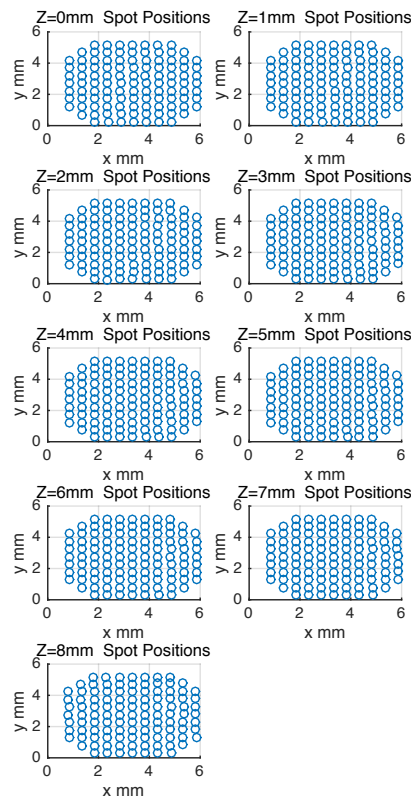


Figure 5.2 Spot centroids for empty cell experiment. The entrance rays form a 13 by 13 matrix over a 6 mm pupil size with 0.5mm increment.

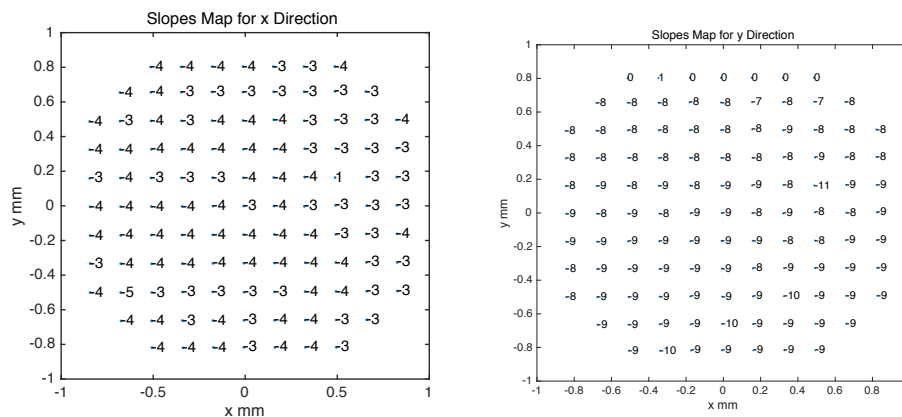


Figure 5.3 Ray slopes of the entrance beam. The values were multiplied by 1000 for easy reading purpose.

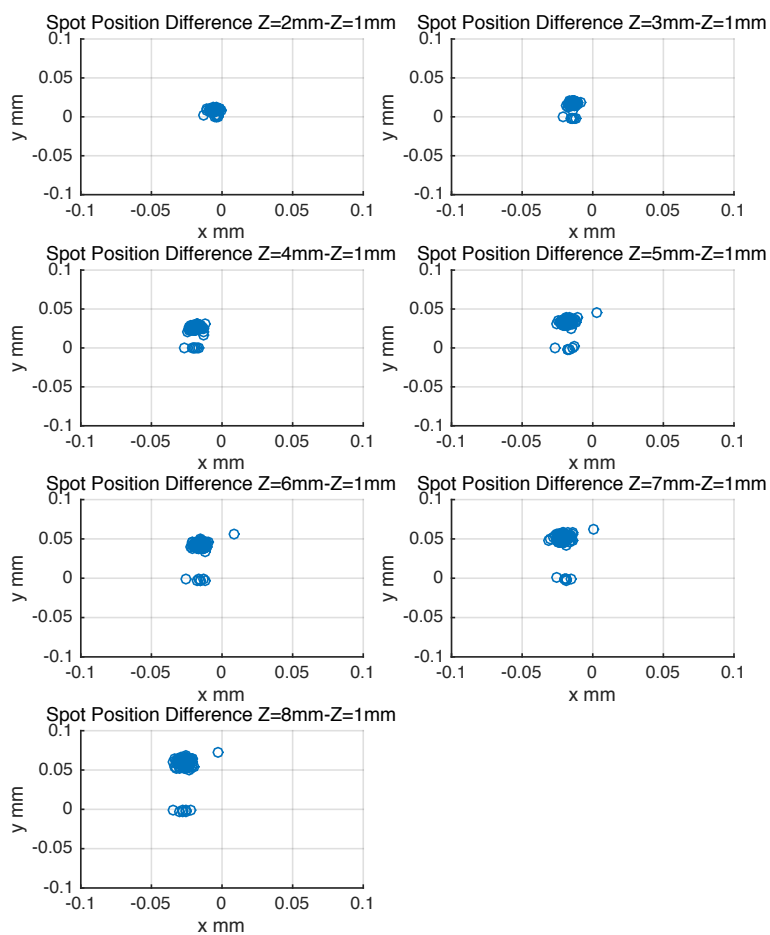


Figure 5.4 Spot centroids differences along the z direction for the empty cell experiment.



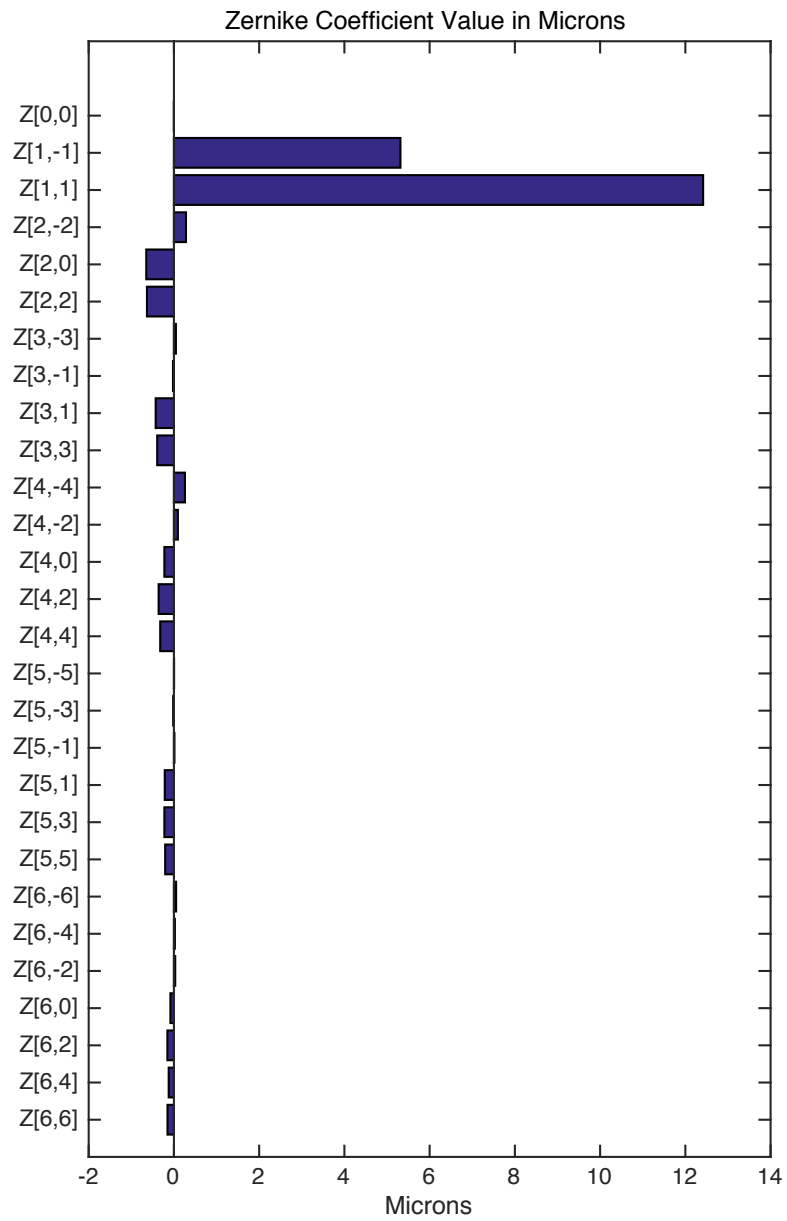


Figure 5.5. Calculated Zernike coefficients for empty cell experiments from Z [0,0] to Z[6,6].

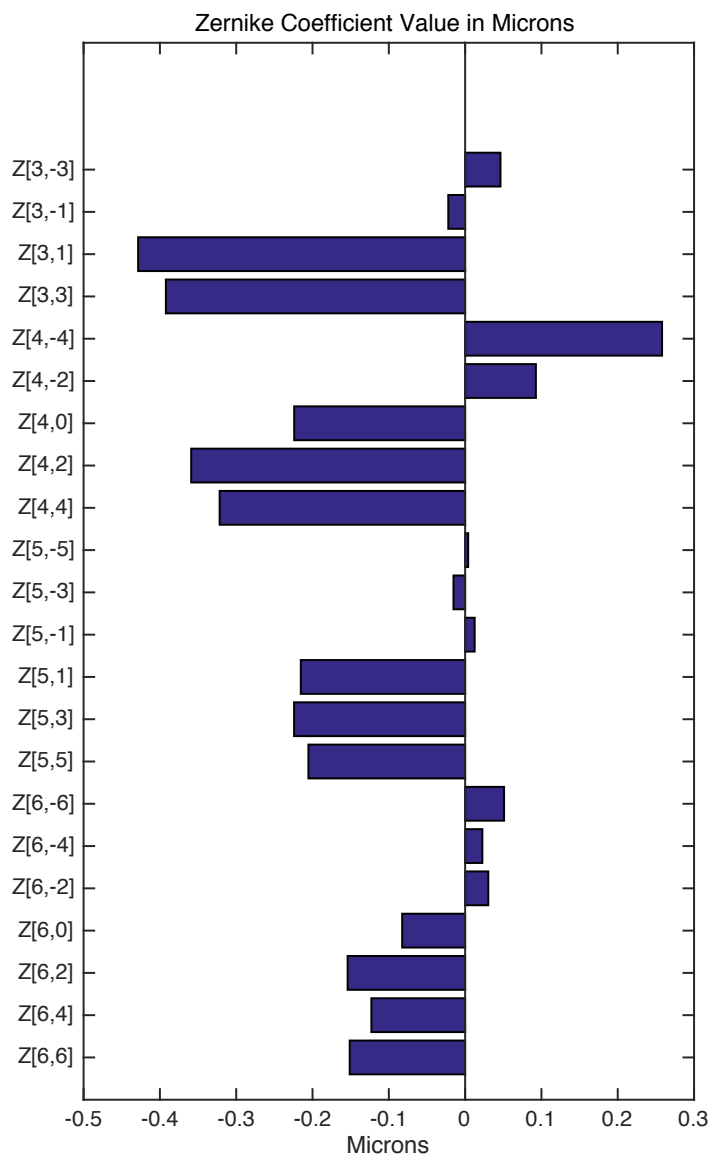


Figure 5.6 Calculated Zernike coefficients for empty cell experiments from Z [3,-3] to Z[6,6].

## WORKS CITED

- Atchison DA, Smith G. Optics of the human eye. Oxford: Butterworth-Heinemann. Oxford, UK. 2000;21-29.
- Born M, Wolf E. Principles of optics, 6th ed. Cambridge University Press: New York, NY. 1980;
- Charman WN. Wavefront aberration of the eye: a review. *Optometry and Vision Science*. 1991; 68(8): 574–583.
- Cubalchini R. Modal wave-front estimation from phase derivative measurements. *Journal of the Optical Society of America*. 1979; 69:972-977
- Garner LF, Smith G. Changes in equivalent and gradient refractive index of the crystalline lens with accommodation. *Ophthalmology and Visual Science*. 1997;74(2):114-119.
- Hernández-Gómez G, Malacara-Hernández Z, Malacara-Doblado D, Díaz-Uribe R, Malacara-Hernández D. Modal integration of Hartmann and Shack–Hartmann patterns. *Journal of the Optical Society of America A*. 2014;31:846-851
- He JC, Burns SA, Marcos S. Monochromatic aberrations in the accommodated human eye. *Vision Research*. 2000; 40 (1):41-48.
- Hernandez VM, Cabot F, Ruggeri M, de Freitas C, Ho A, Yoo S, Parel J-M, Manns F. Calculation of crystalline lens power using a modification of the Bennett method. *Biomedical Optics Express*. 2015;6(11):4501-4515.
- Hudgin H. Wave-front reconstruction for compensated imaging. *Journal of the Optical Society of America*. 1997; 67: 375-378.
- Kasthurirangan S, Markwell EL, Atchison DA., Pope JM. In vivo study of changes in refractive index distribution in the human crystalline lens with age and accommodation. *Investigative Ophthalmology and Visual Science*. 2008;49(6):2531-2540
- Lakshminarayana V , Fleck A . Zernike polynomials: a guide. *Journal of Modern Optics*. 2011; 58, Iss.7
- Liang J, Grimm B, Goetz S, Bille JF. Objective measurements of wave aberrations of the human eye with the use of a Hartmann – Shack wave-front sensor. *Journal of the Optical Society of America A*. 1994;11:1949–1957.

Liang J, Williams DR. Aberrations and retinal image quality of the normal human eye. *Journal of the Optical Society of America A*.1997; 14(11): 2873–2883.

Liang J, Grimm B, Goetz S, Bille JF. Hartmann-Shack sensor as a component in active optical system to improve the depth resolution of the laser tomographic scanner. *International Society for Optics and Photonics*.1991; 1542,10.1117/12.48837

Malacara D. *Optical Shop Testing*, 3rd ed. Wiley: Hoboken, NJ. 2007;

Moreno-Barriuso E, Navarro R. Laser Ray Tracing versus Hartmann–Shack sensor for measuring optical aberrations in the human eye. *Journal of the Optical Society of America A*. 2000;17:974-985

Maceo Heilman B. Evaluation of the Crystalline Lens Gradient Refractive Index using Laser Ray Tracing and Optical Coherence Tomography. *Open Access Dissertations*. 2015;Paper 1558.

Maceo Heilman B, Manns F, de Castro A, Durkee H, Arrieta E, Marcos S, Parel J-M. Changes in monkey crystalline lens spherical aberration during simulated accommodation in a lens stretcher. *Investigative Ophthalmology and Visual Science*. 2015;56:1743–1750.

Navarro R, Losada, MA. Aberrations and relative efficiency of light pencils in the living human eye. *Optometry and Visual Science*. 1997; 74:540–547.

Navarro R, Moreno-Barriuso E. Laser Ray Tracing method for optical testing. *Optic Letters*. 1999; 24:951-953.

Navarro R, Moreno E, Dorronsoro C. Monochromatic aberrations and point-spread functions of the human eye across the visual field. *Journal of the Optical Society of America A*. 1998; 15: 2522–2529.

Roorda A, Glasser A. Wave aberrations of the isolated crystalline lens. *Journal of Vision*. 2004;4(4):250–261.

Smith, G. The optical properties of the crystalline lens and their significance. *Clinical and Experimental Optometry*. 2003;86(1):3-18.

Smartt RN, Steel WH. Theory and application of Point-Diffraction interferometers”. *Japanese Journal of Applied Physics*. 1975; (14): 351–356.

Southwell W. Wave-front estimation from wave-front slope measurements. *Journal of the Optical Society of America*. 1980; 70:998-1006

Thibos LN, Applegate RA, Schwiegerling JT, Webb R, VSIA Standards Taskforce Members. Standards for reporting the optical aberrations of eyes. *Journal of Refractive Surgery*. 2002;18(5):S652-S660.

Thibos LN, Applegate RA, Schwiegerling JT, Webb R, VSIA Standards Taskforce Members. Appendix A: Optical Society of America's standards for reporting optical aberrations. Edited by Porter J, Queener H, Lin J, Thorn K, Awwal AAS. *Adaptive Optics for Vision Science: Principles, Practices, Design and Applications*. John Wiley & Sons, Inc. 2006:511-528.

Wang JY, Silva DE. Wave-front interpretation with Zernike polynomials. *Applied Optics*. 1980;19:1510-1518